

NASA Technical Paper 3651  
ATCOM Technical Report 97-A-005

# Full-Potential Modeling of Blade-Vortex Interactions

---

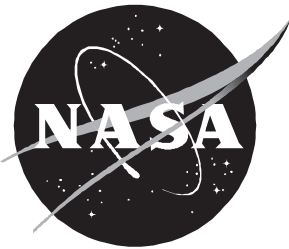
*Henry E. Jones*

---

December 1997

REPORT DOCUMENTATION PAGE			Form Approved OMB No. 0704-0188
<p>Public reporting burden for this collection of information is estimated to average 1 hour per response, including the time for reviewing instructions, searching existing data sources, gathering and maintaining the data needed, and completing and reviewing the collection of information. Send comments regarding this burden estimate or any other aspect of this collection of information, including suggestions for reducing this burden, to Washington Headquarters Services, Directorate for Information Operations and Reports, 1215 Jefferson Davis Highway, Suite 1204, Arlington, VA 22202-4302, and to the Office of Management and Budget, Paperwork Reduction Project (0704-0188), Washington, DC 20503.</p>			
1. AGENCY USE ONLY (Leave blank)	2. REPORT DATE	3. REPORT TYPE AND DATES COVERED	
	December 1997	Technical Paper	
4. TITLE AND SUBTITLE		5. FUNDING NUMBERS	
Full-Potential Modeling of Blade-Vortex Interactions		WU 505-63-36-03 PR A5226	
6. AUTHOR(S)			
Henry E. Jones			
7. PERFORMING ORGANIZATION NAME(S) AND ADDRESS(ES)		8. PERFORMING ORGANIZATION REPORT NUMBER	
Joint Research Program Office Aeroflightdynamics Directorate U.S. Army Aviation and Troop Command NASA Langley Research Center Hampton, VA 23681-2199		L-17594	
9. SPONSORING/MONITORING AGENCY NAME(S) AND ADDRESS(ES)		10. SPONSORING/MONITORING AGENCY REPORT NUMBER	
National Aeronautics and Space Administration Washington, DC 20546-0001 and U.S. Army Aviation and Troop Command St. Louis, MO 63120-1798		NASA TP-3651 ATCOM TR-97-A-005	
11. SUPPLEMENTARY NOTES <p>The information presented in this report was submitted as a dissertation in partial satisfaction of the requirements for the degree of Doctor of Science, The George Washington University, Washington, DC, February 1987.</p>			
12a. DISTRIBUTION/AVAILABILITY STATEMENT		12b. DISTRIBUTION CODE	
Unclassified–Unlimited Subject Category 71 Availability: NASA CASI (301) 621-0390			
13. ABSTRACT (Maximum 200 words) <p>A study of the full-potential modeling of a blade-vortex interaction was made. A primary goal of this study was to investigate the effectiveness of the various methods of modeling the vortex. The model problem restricts the interaction to that of an infinite wing with an infinite line vortex moving parallel to its leading edge. This problem provides a convenient testing ground for the various methods of modeling the vortex while retaining the essential physics of the full three-dimensional interaction. A full-potential algorithm specifically tailored to solve the blade-vortex interaction (BVI) was developed to solve this problem. The basic algorithm was modified to include the effect of a vortex passing near the airfoil. Four different methods of modeling the vortex were used: (1) the angle-of-attack method, (2) the lifting-surface method, (3) the branch-cut method, and (4) the split-potential method. A side-by-side comparison of the four models was conducted. These comparisons included comparing generated velocity fields, a subcritical interaction, and a critical interaction. The subcritical and critical interactions are compared with experimentally generated results. The split-potential model was used to make a survey of some of the more critical parameters which affect the BVI.</p>			
14. SUBJECT TERMS			15. NUMBER OF PAGES
Aerodynamics; Acoustics; Blade-vortex interaction; Unsteady transonic flow			90
			16. PRICE CODE
			A05
17. SECURITY CLASSIFICATION OF REPORT	18. SECURITY CLASSIFICATION OF THIS PAGE	19. SECURITY CLASSIFICATION OF ABSTRACT	20. LIMITATION OF ABSTRACT
Unclassified	Unclassified	Unclassified	

Report Documentation Page		
<b>Report Date</b> 01DEC1997	<b>Report Type</b> N/A	<b>Dates Covered (from... to)</b> -
<b>Title and Subtitle</b> Full-Potential Modeling of Blade-Vortex Interactions		<b>Contract Number</b>
		<b>Grant Number</b>
		<b>Program Element Number</b>
<b>Author(s)</b>		<b>Project Number</b>
		<b>Task Number</b>
		<b>Work Unit Number</b>
<b>Performing Organization Name(s) and Address(es)</b> NASA Langley Research Center Hampton, VA 23681-0001		<b>Performing Organization Report Number</b>
<b>Sponsoring/Monitoring Agency Name(s) and Address(es)</b> National Aeronautics and Space Administration Washington, DC 20546-0001		<b>Sponsor/Monitor's Acronym(s)</b>
		<b>Sponsor/Monitor's Report Number(s)</b>
<b>Distribution/Availability Statement</b> Approved for public release, distribution unlimited		
<b>Supplementary Notes</b>		
<b>Abstract</b>		
<b>Subject Terms</b>		
<b>Report Classification</b> unclassified		<b>Classification of this page</b> unclassified
<b>Classification of Abstract</b> unclassified		<b>Limitation of Abstract</b> UU
<b>Number of Pages</b> 90		



NASA Technical Paper 3651  
ATCOM Technical Report 97-A-005

# Full-Potential Modeling of Blade-Vortex Interactions

---

*Henry E. Jones*  
*Joint Research Program Office*  
*Aerofluidynamics Directorate*  
*U.S. Army Aviation and Troop Command*  
*Langley Research Center • Hampton, Virginia*

National Aeronautics and Space Administration  
Langley Research Center • Hampton, Virginia 23681-2199

---

December 1997

### **Acknowledgments**

This work would not have been completed without the guidance and support of Francis X. Caradonna, Aeroflightdynamics Directorate, U.S. Army Aviation and Missile Command, Ames Research Center, Moffett Field, CA. His persistent encouragement enabled me to continue when many times I would have quit.

Available electronically at the following URL address: <http://techreports.larc.nasa.gov/ltrs/ltrs.html>

Printed copies available from the following:

NASA Center for AeroSpace Information  
800 Elkridge Landing Road  
Linthicum Heights, MD 21090-2934  
(301) 621-0390

National Technical Information Service (NTIS)  
5285 Port Royal Road  
Springfield, VA 22161-2171  
(703) 487-4650

## Contents

Figures . . . . .	v
Symbols . . . . .	vii
Summary . . . . .	xii
1. Introduction . . . . .	1
1.1. Physical Problem . . . . .	1
1.2. Physical Model . . . . .	2
1.3. Vortex Models . . . . .	2
1.4. Historical Background . . . . .	2
1.5. Purpose of Current Research . . . . .	4
2. Full-Potential Algorithm . . . . .	4
2.1. Conservative Formulation of Transformed Equation . . . . .	4
2.2. Computational Grid . . . . .	5
2.3. Metric Derivatives . . . . .	5
2.4. Boundary Conditions . . . . .	6
2.4.1. Airfoil Surface . . . . .	6
2.4.2. Outer Boundaries . . . . .	7
2.4.3. Aft Face . . . . .	7
2.4.4. Kutta Condition . . . . .	7
2.5. Difference Equation . . . . .	7
2.6. Implementing the Algorithm . . . . .	9
2.6.1. Basic Difference Operators . . . . .	9
2.6.2. Flux Operator Differencing . . . . .	9
2.6.2.1. Flux density term (switching) . . . . .	9
2.6.2.2. Flux metric term (consistent differencing) . . . . .	11
2.6.3. Approximate Factorization . . . . .	13
2.6.4. Implementing Boundary Conditions . . . . .	14
2.6.5. Solution Steps . . . . .	15
2.7. Steady-State Algorithm . . . . .	15
3. Vortex Models . . . . .	16
3.1. The Surface-Specification Methods . . . . .	17
3.1.1. Angle-of-Attack Method . . . . .	17
3.1.2. Lifting-Surface Method . . . . .	18
3.2. Explicit Models . . . . .	18
3.2.1. Branch-Cut Method . . . . .	18
3.2.2. Split-Potential Method . . . . .	19

4. Computational Results . . . . .	21
4.1. Executing the Algorithm . . . . .	21
4.1.1. Executing Basic Airfoil Solution . . . . .	21
4.1.2. Executing HSI Problem . . . . .	21
4.1.3. Data Recovery . . . . .	22
4.2. Results From Basic Airfoil Solution . . . . .	22
4.2.1. Comparison With Original Algorithm . . . . .	22
4.2.2. Subcritical Flow . . . . .	22
4.2.3. Supercritical Case . . . . .	22
4.2.4. Oscillating Airfoil . . . . .	23
4.3. Introduction to HSI . . . . .	24
4.3.1. Generic Vortex Interaction . . . . .	24
4.3.2. Effects of Time Terms . . . . .	26
4.3.3. Comparison With Other Codes . . . . .	30
4.4. Comparison of Vortex Models . . . . .	32
4.4.1. Vortex Velocity Field . . . . .	32
4.4.2. Related Experiment . . . . .	32
4.4.3. Subcritical Interaction . . . . .	33
4.4.4. Critical Interaction . . . . .	34
4.4.5. Summation . . . . .	34
4.5. Parametric Sweeps . . . . .	35
4.5.1. Effect of Mach Number . . . . .	35
4.5.2. Effect of Vortex Strength . . . . .	35
4.5.3. Effect of Miss Distance . . . . .	36
4.5.4. Effect of Core Size . . . . .	36
4.5.5. Effect of Angle of Attack . . . . .	36
5. Concluding Remarks . . . . .	72
Appendix A—The Computational Grid . . . . .	74
Appendix B—Derivations of Boundary Conditions . . . . .	76
Appendix C—Time Linearization Operator . . . . .	77
References . . . . .	78

## Figures

Figure 1. Interaction of infinite aspect ratio blade with infinite line vortex . . . . .	1
Figure 2. Low-speed interaction between rotor and vortex. . . . .	1
Figure 3. High-speed interaction between rotor and vortex. . . . .	1
Figure 4. Transpiration boundary condition at airfoil surface. . . . .	6
Figure 5. Computation of velocity at grid point in field permeated with branch cuts. . . . .	10
Figure 6. Principal vortex models. . . . .	16
Figure 7. Angle-of-attack vortex model. . . . .	17
Figure 8. Lifting-surface vortex model. . . . .	18
Figure 9. Branch-cut vortex model. . . . .	18
Figure 10. Distribution of vorticity to four points nearest vortex. . . . .	19
Figure 11. Split-potential vortex model. . . . .	19
Figure 12. Maximum residual convergence history for NACA 0012 airfoil at several Mach numbers and $\alpha = 0^\circ$ . . . . .	21
Figure 13. Pressure coefficients at midchord for parabolic arc airfoil as it thickens then thins for $M_\infty = 0.85$ and $\tau = 0.104$ . . . . .	22
Figure 14. Pressure coefficients for NACA 0012 airfoil at $M_\infty = 0.63$ and $\alpha = 2^\circ$ . . . . .	23
Figure 15. Pressure coefficients for Aerospatiale RA16SC1 airfoil at $M_\infty = 0.30$ and $\alpha = 0^\circ$ . . . . .	23
Figure 16. Pressure coefficients for NACA 0012 airfoil at $M_\infty = 0.80$ and $\alpha = 0^\circ$ . . . . .	24
Figure 17. Pressure coefficients for Aerospatiale RA16SC1 airfoil at $M_\infty = 0.76$ and $\alpha = 0^\circ$ . . . . .	24
Figure 18. Pressure coefficients for NACA 0012 airfoil at $M_\infty = 0.755$ and $\alpha = 0$ . . . . .	24
Figure 19. Pressure coefficients for oscillating NACA 0012 airfoil at $M_\infty = 0.755$ . . . . .	25
Figure 20. Pressure coefficients for Aerospatiale RA16SC1 airfoil with oscillating 25-percent flap. . . . .	26
Figure 21. Variation of airfoil lift with vortex location for typical BVI. . . . .	27
Figure 22. Airfoil surface pressure distribution for typical BVI. . . . .	28
Figure 23. Variation of lower surface pressure coefficient with vortex location for typical BVI. . . . .	29
Figure 24. Effect of time step on airfoil lift during BVI. . . . .	29

Figure 25. Effect of error wave propagation during BVI. . . . .	30
Figure 26. Effect of $\mathbf{G}_t$ terms on split-potential model. . . . .	30
Figure 27. Airfoil lift variation with vortex location for various algorithms. . . . .	31
Figure 28. Vortex-induced velocity on airfoil surface. . . . .	32
Figure 29. Experimental measurement of blade-vortex interaction. . . . .	33
Figure 30. Variation of airfoil lift with vortex location for the four vortex models. . . . .	33
Figure 31. Variation of airfoil pressure with vortex location. Subcritical flow. . . . .	37
Figure 32. Computed and measured airfoil surface pressures for $M_\infty = 0.536$ . . . . .	38
Figure 33. Airfoil lift variation with vortex location for the four vortex models at critical flow. . . . .	42
Figure 34. Variation of airfoil pressure with vortex location at critical flow. . . . .	43
Figure 35. Computed and measured airfoil surface pressures for $M_\infty = 0.714$ . . . . .	44
Figure 36. Effect of Mach number on variation of airfoil lift. . . . .	48
Figure 37. Airfoil pressure distribution at selected vortex locations for several free-stream Mach numbers. . . . .	49
Figure 38. Effect of vortex strength on variation of airfoil lift. . . . .	52
Figure 39. Airfoil pressure distribution at selected vortex locations for several vortex strengths. . . . .	53
Figure 40. Effect of vertical miss distance on variation of airfoil lift coefficient. . . . .	56
Figure 41. Airfoil pressure distribution at selected vortex locations for several values of $y_v$ . . . . .	57
Figure 42. Effect of core size on variation of airfoil lift. . . . .	60
Figure 43. Airfoil pressure distribution at selected vortex locations for several vortex core radii. . . . .	61
Figure 44. Effect of angle of attack on airfoil lift variation for subcritical flow. . . . .	64
Figure 45. Airfoil pressure distribution at selected vortex locations. . . . .	65
Figure 46. Effect of angle of attack on airfoil lift variation for supercritical flow. . . . .	68
Figure 47. Airfoil pressure distribution at selected vortex locations. . . . .	69

## Symbols

<b>A</b>	coefficient of $j - 1$ terms in solution matrix
<b>A</b> <sub>1</sub>	chordwise metric
<b>A</b> <sub>2</sub>	cross derivative metric
<b>A</b> <sub>3</sub>	chord-normal metric
ADI	alternating directional implicit
a	vortex core radius normalized by $c$
$a_\infty$	free-stream speed of sound
<b>B</b>	coefficient of $j$ terms in solution matrix
BVI	blade-vortex interaction
$b$	radius of transform circle for Joukowski airfoil
<b>C</b>	coefficient of $j + 1$ terms in solution matrix
<b>C</b> <sup>*</sup>	conservation correction term in algorithm
$C$	damping factor for upwind biasing
Calc.	calculated
$c$	rotor chord
$c_l$	airfoil lift coefficient
$C_{l,v}$	vortex strength expressed in equivalent lift coefficient, $\frac{2\Gamma^*}{M_\infty}$
$c_p$	pressure coefficient
$c_p^*$	critical pressure coefficient
$D_n$	determinant of Jacobian matrix (at node)
$D_m$	determinant of Jacobian matrix (at midsegment)
Exp.	experimental
<b>G</b>	prescribed vorticity velocity potential
$\Delta \mathbf{G}^N$	$= \mathbf{G}^N - \mathbf{G}^{N-1}$
HSI	high-speed interaction
<b>I</b>	identity matrix
$i$	chordwise grid index
<b>J</b> <sub>n</sub>	Jacobian of coordinate transform matrix (at node)
<b>J</b> <sub>m</sub>	Jacobian of coordinate transform matrix (at midsegment)
$j$	chord normal grid index
$k$	reduced frequency, $\frac{\omega c}{U_\infty}$
<b>L</b>	time update operator on left-hand side of algorithm
LSI	low-speed interaction
$M_l$	local Mach number
$M_R$	relative Mach number of equivalent steady coordinate for BVI

$M_\infty$	free-stream Mach number
$N$	stream-normal distance in real space normalized by $c$
$\mathbf{q}$	velocity vector
$\mathbf{R}$	right-hand side of solution vector
$\mathbf{R}^*$	spatial flux terms on right-hand side of algorithm
$\mathbf{R}_\infty$	free-stream subtraction vector
$r$	radial distance from vortex, normalized by $c$
$S$	streamwise distance in real space normalized by $c$
$S_u$	velocity normal to airfoil upper surface (in computational space)
Sur.	surface
TSD	transonic small distribution
$t$	time, chords traveled, $\frac{\tilde{t}a_\infty}{c}$
$\Delta t$	time step
$\tilde{t}$	time
$\mathbf{U}$	chordwise contravariant velocity vector
$U_v$	vortex-induced velocity in $x$ direction
$U_\infty$	free-stream velocity
$u$	chordwise velocity normalized by $a_\infty$
$\tilde{u}$	chordwise velocity
$\mathbf{V}$	chord-normal contravariant velocity vector
$V$	induced velocity
$V_v$	vortex-induced velocity in $y$ direction
$v$	chord-normal velocity normalized by $a_\infty$
$w$	complex velocity about Joukowski airfoil
$x$	chordwise distance normalized by airfoil chord
$\tilde{x}$	chordwise distance in real space
$x'$	equivalent steady coordinate for BVI
$x^*, y^*$	cell width and height, respectively
$x_v$	vortex location
$y$	chord-normal distance normalized by airfoil chord
$\tilde{y}$	chord-normal distance in real space
$y'$	equivalent steady coordinate for BVI
$y_v$	vertical miss distance, chords
$\mathbf{z}^*$	complex coordinate for Joukowski airfoil solution
$\alpha$	airfoil angle of attack
$\beta$	$= \rho^{2-\gamma}$

$\hat{\beta}$	$= \frac{\beta}{\mathbf{J}}$
$\Gamma$	jump in potential across a branch cut
$\Gamma^*$	vortex strength
$\gamma$	specific heat ratio
$\delta_\eta$	chord-normal difference operator
$\delta_\xi$	chordwise difference operator
$\delta_\tau \Phi^N$	difference operator in time, $\frac{\Phi^N - \Phi^{N-1}}{\Delta t^N}$
$\epsilon$	angle between grid and airfoil surface
$\eta$	chord-normal distance in computational space
$\theta$	angle between blade and vortex
$\nu$	switching parameter
$\xi$	chordwise distance in computational space
$\rho$	fluid density normalized by free-stream values
$\tilde{\rho}$	fluid density
$\hat{\rho}$	$= \frac{\rho}{\mathbf{J}}$
$\tau$	time in computational space, chords traveled
$\Phi$	total velocity potential
$\phi$	perturbation velocity potential
$\varphi$	phase angle
$\omega$	circular frequency
2-D	two-dimensional
3-D	three-dimensional

Subscript:

S	surface conditions
---	--------------------

Superscript:

N	current time level
---	--------------------

## Summary

A study of the full-potential modeling of a blade-vortex interaction was made. A primary goal of this study was to investigate the effectiveness of the various methods of modeling the vortex. The problem was studied within the context of a two-dimensional model problem, which represents one of the limiting types of blade-vortex interactions (BVIs). The model problem restricts the interaction to that of an infinite wing with an infinite line vortex moving parallel to its leading edge. This problem provides a convenient testing ground for the various methods of modeling the vortex while retaining the essential physics of the full three-dimensional interaction. The flow field is assumed to be inviscid, irrotational, unsteady, and, in general, transonic.

A full-potential algorithm specifically tailored to solve BVI was developed to solve this problem. The algorithm makes use of the unsteady mass conservation and Bernoulli equations to form a full-potential model of the flow field. The system of equations is reduced to one equation by using a Taylor-series expansion of the temporal derivative of the density term in the conservation equation. The spatial derivatives are recast in “delta” form, with the density written at the previous time step. The stability of the algorithm in transonic flow is assured through the use of upwind biasing of the density in the flux terms. The flux metrics are computed by the consistent metric method, which has been found to be superior to the so-called free-stream subtraction method that has difficulties with grid singularities. The equation is approximately factored into convenient geometric parts in order to reduce the matrix to a compact form. A tridiagonal matrix inversion is used to solve for the updated potential solution. The model has the capability to predict the steady and unsteady flow about an airfoil under subcritical and transonic flow conditions. Comparisons of the results predicted are made with those presented by other researchers and with experimental data. The comparisons indicate that the algorithm is able to predict basic unsteady transonic flow about an airfoil.

The basic algorithm has been modified to include the effect of a vortex passing near the airfoil. Four different methods of modeling the vortex were used:

1. The angle-of-attack method
2. The lifting-surface method
3. The branch-cut method
4. The split-potential method

The angle-of-attack method uses the velocity field of a point vortex to compute a vortex-induced velocity at the airfoil quarter-chord. This velocity is then used to compute an effective angle of attack of the airfoil. This method is identical to techniques which are currently in use in comprehensive helicopter rotor analyses. The lifting-surface method is an extension of the angle-of-attack method in which the vortex-induced velocity is a function of chordwise distance on the airfoil surface. The branch-cut method is a flow-field vortex representation that makes use of a surface of potential discontinuity, the edge of which constitutes the vortex location. The effect of the vortex is implemented by imposing special differencing methods along the cut. In the split-potential method, the velocity field is split between a known field (induced by the vortex) and an unknown perturbation field caused by the airfoil.

A side-by-side comparison of the four models was conducted. These comparisons include comparing generated velocity fields, a subcritical interaction, and a critical interaction. The subcritical and critical interactions are compared with experimentally generated results.

The split-potential model was used to make a survey of some of the more critical parameters which affect the BVI. The survey studies general flow parameters such as free-stream Mach number and airfoil angle of attack, and vortex parameters such as strength, core size, and miss distance. The results were computed at subcritical and supercritical free-stream Mach numbers. For the vortex parameters, the free-stream Mach number was chosen to be just subcritical in order to study the effect of the vortex on the formation of critical flow on the airfoil.

## 1. Introduction

### 1.1. Physical Problem

Helicopter rotors operating in high-speed flight encounter a number of important aerodynamic phenomena. Two major features that dominate the flow on the advancing side of the rotor disc exist. The first key feature is the presence of transonic flow conditions. Transonic flow imposes major limitations on the high-speed performance of the rotor. These limitations manifest themselves in high vibration levels, power divergence, noise, and component fatigue. The second key feature is the presence of a large vortex system near the rotor. The vortex system is composed of a series of helical vortex filaments generated at the tip of the blade. The following blade, which may be experiencing transonic flow, frequently interacts with these vortices.

The interaction between a rotor blade and the vortices from a preceding blade can have a large impact on the blade aerodynamic environment. These blade-vortex interactions (BVIs) cause large changes in local pressure which can occur over short periods. The pressure changes exist within a flow field which is, in general, transonic, unsteady, viscous, and three-dimensional. The vortex passage, therefore, acts to modify an already complicated flow field.

A rotor interacts with a vortex under a wide range of relative orientations. However, the essential physics can be illustrated by considering a rectangular blade of infinite aspect ratio interacting with an infinite line vortex at an angle  $\theta$ . Johnson (ref. 1) has shown that this problem is steady in a coordinate system whose origin travels with the intersection of the blade centerline and the projection of the free vortex on the blade. (See fig. 1.) The steady coordinate system is

$$\left. \begin{aligned} x' &= x \\ y' &= y - M_\infty \cot \theta \end{aligned} \right\} \quad (1.1)$$

The speed at which the origin travels is a function of the angle  $\theta$ . When  $\theta = \pi/2$ , the vortex is perpendicular to the blade and the speed of the interaction point is zero. (See fig. 2.) For increasing values of  $\theta$ , the speed of the interaction point increases, but the problem remains steady. For  $\theta = \pi$ , there is no spanwise flow dependence, and the problem is now two-dimensional. (See fig. 3). However, the cost of this two-dimensional simplification is that this problem is now intrinsically unsteady because the speed of the interaction point is infinite. The blade-vortex interaction may then be classified by the two limiting conditions defined by  $\theta = \pi/2$  and  $\theta = \pi$ . The first condition ( $\theta = \pi/2$ ) may be

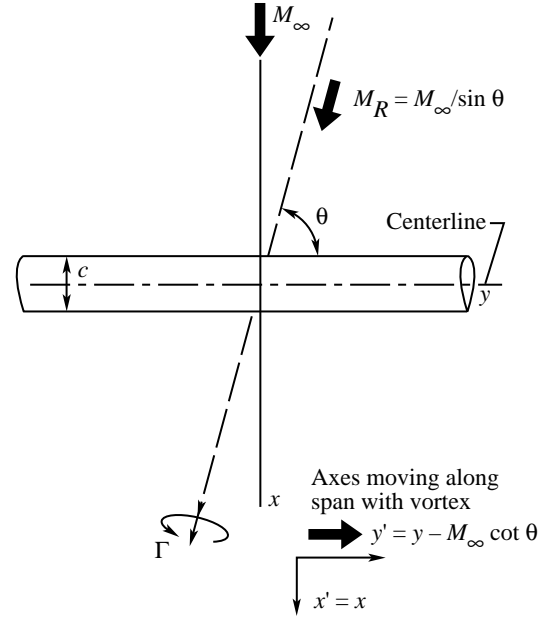


Figure 1. Interaction of infinite aspect ratio blade with infinite line vortex.

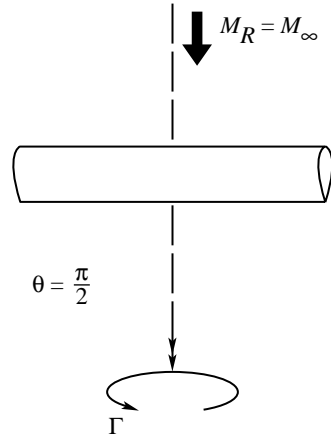


Figure 2. Low-speed interaction between rotor and vortex.

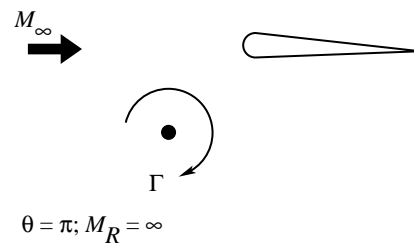


Figure 3. High-speed interaction between rotor and vortex.

called a low-speed interaction (LSI) because this is a steady problem even in the original coordinate system. The second condition ( $\theta = \pi$ ) may be called a high-speed interaction (HSI) because this is an unsteady problem even in the transformed coordinate

system. Both LSI and HSI represent real interactions which can have significant effects on the rotor aerodynamics. LSI, for instance, is the principal type of interaction which occurs during hovering flight. LSI affects rotor power and low harmonic loading. HSI occurs during high-speed flight and descents and affects noise, vibrations, and the higher harmonics of loading. Furthermore, HSI contains all the physics of LSI; therefore, the capability to solve for HSI contains the ability to solve LSI. The solution of HSI is the main study of this report.

## 1.2. Physical Model

The solution of HSI requires the computation of the time-varying surface pressures during the vortex passage. Because the angle between the vortex axis and the blade is zero, no spanwise flows are induced and the flow can be assumed to be two-dimensional. The distance between the airfoil and the vortex is assumed to be large enough to assure a basically inviscid flow; that is, the vortex does not distort the airfoil boundary layer. Any shock waves present are assumed to be weak and not a source of rotational flow. With these assumptions, the aerodynamic problem can be modeled by assuming a two-dimensional potential flow field. The mass conservation equation for such a flow field is

$$\frac{\partial \tilde{\rho}}{\partial t} + \frac{\partial}{\partial \tilde{x}}(\tilde{\rho} \Phi_{\tilde{x}}) + \frac{\partial}{\partial \tilde{y}}(\tilde{\rho} \Phi_{\tilde{y}}) = 0 \quad (1.2)$$

Since the flow is isentropic, the fluid density can be determined from the Bernoulli equation

$$\tilde{\rho} = \left[ 1 + \frac{\gamma - 1}{2} \left( M_{\infty}^2 - 2\Phi_{\tilde{t}} - \Phi_{\tilde{x}}^2 - \Phi_{\tilde{y}}^2 \right) \right]^{1/(\gamma-1)} \quad (1.3)$$

These two equations, solved together, constitute a full-potential model of the flow field. A solution for these equations can be accomplished by using a finite-difference algorithm. Such an algorithm, originally developed by Steger and Caradonna (ref. 2) is presented in section 2. This scheme is then modified to include various vortex models.

## 1.3. Vortex Models

A primary aim of this report is to study the effect of various vortex models on the solution of HSI within the framework of a 2-D potential finite-difference algorithm. All these models are candidates for use

in 3-D methods. Four different methods have been used to model the vortex:

1. The first model approximates the vortex effect as a change in airfoil angle of attack. The velocity field of a point vortex law is used to compute an induced velocity at the airfoil quarter chord. This induced velocity is then applied over the entire airfoil. This is referred to as the “angle-of-attack method.”
2. The second model is related to the first but, instead of imposing only a constant velocity on the airfoil, a distributed velocity field from the vortex is imposed on the airfoil surface. This is analogous to a lifting-surface method.
3. The third model is to specify a branch-cut discontinuity in the potential field. The vortex is modeled as a jump in potential across the branch cut, the edge of which represents the center of the vortex. This is referred to as the “branch-cut method.”
4. The fourth method models the vortex by expressing the potential as the sum of a known potential due to the vortex and an unknown potential due to the airfoil. This is referred to as the “split-potential method.”

The first two vortex models are typical of the linear integral flow methods which are used in all the currently available rotor-analysis methods. Methods 3 and 4 are flow models of the vortex and can only be used in finite-difference methods. An important aspect of this work is to determine whether this more elaborate modeling is necessary.

## 1.4. Historical Background

The problem of blade-vortex interactions is central to helicopter aerodynamics because the interaction of the rotor and its vortex system can have a large effect on the aerodynamic environment of the blade. The four vortex models discussed in section 1.3 reflect the level of sophistication of the global theories within which they were developed. To appreciate fully the various vortex models, reviewing the basics of the global rotor computations is useful.

Because of the geometric complexity of the vortex system, early analysts (e.g., Glauert in 1926 (ref. 3)) treated the wake influence on the rotor by using momentum theory and blade element approximations. The resulting models led to simple algebraic equations for the induced velocities. Computing an effective angle of attack on each blade segment with the induced velocity at the disc is possible and is the

essence of the angle-of-attack method. The resulting angle of attack is then used in conjunction with tabulated lift, drag, and moment data to compute rotor performance. This approach has proven to be useful in computing total aircraft performance but is unable to predict accurately the details of the rotor aerodynamic environment. Accurate prediction of these details could not be performed until the advent of high-speed computers (circa 1960).

Piziali and DuWalt (ref. 4) proposed the first practical method for studying the details of the rotor-wake interaction. The complete rotor wake was modeled with a series of such line segments. The velocities induced by each segment at the rotor were combined to produce an effective angle of attack. The solution then proceeds as before. This improved the earlier model by allowing for individual blade-vortex encounters to be studied. Isay (ref. 5) presented a more general solution of the induced velocity for a spiral wake model.

Kocurek (ref. 6) presented an extension of this method (for hover only) in which the blade was treated as a lifting surface. The induced velocity was computed over the entire surface of the blade not just at one point. These velocities were then used to compute local pressure and lift. Tabulated data were used to provide the drag and pitching moment with the solution proceeding as before.

These approaches can be broadly classified as blade-element integral methods. Currently they are the most popular methods of rotor analysis in use (especially the angle-of-attack method). Numerous investigators have improved on the basic model culminating in the effort by Johnson (ref. 7). Despite an impressive versatility, however, the blade-element integral methods have some serious shortcomings. Primarily the deficiencies of these methods lie in the use of tabulated airfoil data to provide aerodynamic forces and in the related assumption of local two-dimensional flow. Furthermore, unsteady aerodynamic effects are modeled with quasi-steady approximations which are incapable of modeling the truly unsteady phenomena of transonic flow.

During the time period 1960–1980, the field of computational fluid dynamics underwent rapid growth. Computer speeds increased to the point where it became possible to use finite-difference methods to compute simple rotor flows. Various investigators (e.g., refs. 8 and 9) addressed the limitations of the integral methods by using finite-difference methods to compute rotor aerodynamics, typically with hybrid methods. The hybrid methods

use finite-difference techniques to solve a limited part of the flow field and a linear integral method to provide the global solution. This method provides the capability to compute the entire transonic nonlinear flow field near the rotor. An essential difference between the nonlinear and the linear integral parts of the solution is that the linear solutions depend only on the blade surface and shear layer conditions because the speed of sound is assumed to be constant. In contrast the nonlinear solution depends on flow conditions in the entire flow field. For rotors, this field dependence is especially important because the field is frequently occupied with vortices from previous blades. Therefore, an important part of the development of rotor finite-difference schemes is the means of specifying vortices.

Caradonna, Tung, and Desopper (ref. 8) developed the first finite-difference scheme that included vortices in the flow field. They solved a high-tip-speed hover problem in which the vortices were specified as edges of potential discontinuities (branch-cut method). This scheme produced good comparisons with pressure data. Interestingly, reference 8 also reported an inability to obtain a good solution when the effect of the vortex was included only by a blade surface inflow specification (angle-of-attack method). Strawn and Caradonna (ref. 9) solved a similar problem by using a split-potential model. Their method is a modified version of a full-potential algorithm developed by Bridgeman, Steger, and Caradonna (ref. 10).

To date, the forward flight computations have relied on vortex-induced surface inflow boundary conditions (angle-of-attack method) and have been fairly successful at high advance ratios where the induced flow is a small percentage of the total inflow. Nevertheless, there remains a serious question of how best to introduce moving vortices into a computational grid and thereby predict their effect. The solution of the 2-D HSI is a convenient testing ground for the vortex modeling schemes that are required for the full 3-D problem.

A number of investigators (refs. 11 to 17) have studied the 2-D HSI problem by using finite-difference methods. These investigators have been primarily interested in acoustic effects and have used modified versions of earlier algorithms and vortex models. The problem of vortex specification has not been a primary aim of these studies. George and Chang (ref. 11) modeled the vortex with the angle-of-attack method to investigate the effects of blade-vortex interactions on noise. Later they extended their methodology and results to reflect the results

from the branch-cut method (ref. 12). McCroskey and Goorjian (ref. 13) introduced the split-potential method, which was first proposed by Steinhoff. (See ref. 14.) Computations with Euler and thin-layer Navier-Stokes algorithms have been presented in references 15 and 16. Sankar and Malone (ref. 17) presented a full-potential solution by using a strongly implicit procedure. All these methods produce results which are characteristically similar and, to a limited extent, show good correlation with each other, especially those methods that employ the split-potential vortex model.

### 1.5. Purpose of Current Research

Of all these methods, the full-potential approach is probably the best suited to rotor computations because it is geometrically general and is much faster than the Euler and Navier-Stokes methods. The purpose of the current research is to explore fully the BVI phenomena within the context of the full-potential algorithm. This exploration requires four major tasks.

The first task is to develop a full-potential algorithm which is specifically tailored to solve the BVI problem. Improvement to previous methods include (1) special boundary conditions to increase flexibility in modeling airfoils, (2) a “full-potential” mesh, (3) allowance for a variable time step in the unsteady solution, and (4) an improved method of computing the flux metric. Details of these improvements are presented in section 2, which includes a complete derivation of the full-potential algorithm.

The second task is to implement the various methods of modeling a vortex. This task can best be accomplished within the framework of a single algorithm. Using a single algorithm eliminates any question of differences raised by issues such as grid or boundary conditions. The present method provides a unique opportunity to accomplish this. The full-potential algorithm is modified to include the effects of four different ways to compute the influence of the vortex. These modifications include

1. Modifications to airfoil boundary conditions for the angle-of-attack and lifting-surface methods
2. Special internal boundary conditions to implement the branch-cut method
3. The inclusion of a split-potential model

The split-potential method has not yet been fully implemented for unsteady BVI problems with the

full-potential flow model; this will be accomplished for the first time in the present work. Details of the vortex modeling are presented in section 3.

The third tasks is a unique side-by-side comparison between the models. Comparisons with experimental data for subcritical and critical flow conditions are also made. These comparisons highlight the merits of the various models. This work provides the basis for a more systematic approach to three-dimensional computations of blade-vortex interaction. The results of these comparisons are presented in section 4.

The fourth task is to make a parametric study of the BVI problem, which will be the first complete study presented in the literature. The parameters studied fall into two categories: (1) flow-field parameters and (2) vortex parameters. The results of these parametric studies are presented in section 4.

## 2. Full-Potential Algorithm

The aerodynamic problem of HSI will be modeled with a potential flow-field assumption. Under this assumption the basic equations of fluid dynamics (mass, momentum, energy, and equation of state) are reduced to a system of two equations with two unknowns: the mass conservation equation,

$$\frac{\partial \rho}{\partial t} + \frac{\partial}{\partial x}(\rho \Phi_x) + \frac{\partial}{\partial y}(\rho \Phi_y) = 0 \quad (2.1)$$

and the Bernoulli equation,

$$\rho = \left[ 1 + \frac{\gamma - 1}{2} \left( M_\infty^2 - 2\Phi_t - \Phi_x^2 - \Phi_y^2 \right) \right]^{1/(\gamma-1)} \quad (2.2)$$

In these equations, all velocities are normalized by  $a_\infty$ ; distances, by the airfoil chord; time, by  $c/a_\infty$ ; and density, by its free-stream value.

### 2.1. Conservative Formulation of Transformed Equation

The system of equations (eqs. (2.1) and (2.2)) is transformed to a computational plane under the general transformation

$$\left. \begin{aligned} \xi &= \xi(x, y, t) \\ \eta &= \eta(x, y, t) \\ \tau &= t \end{aligned} \right\} \quad (2.3)$$

and the equations must be conservative in these coordinates. Equation (2.1) is written in conservative (or divergence) form; that is,

$$\partial_t f + \frac{\partial \mathbf{F}_i}{\partial x_i} = 0 \quad (2.4)$$

where  $\mathbf{F}_i$  is the flux of the quantity  $f$  ( $\rho$  for the potential model). This generic form must be maintained through the entire solution process (including discretization) if mass conservation is maintained. Vivian (ref. 18) has derived a general conservation form for such a generalized coordinate system which transforms equation (2.1) into

$$\partial_\tau \left( \frac{\rho}{\mathbf{J}_n} \right) + \partial_\xi \left( \frac{\rho \mathbf{U}}{\mathbf{J}_n} \right) + \partial_\eta \left( \frac{\rho \mathbf{V}}{\mathbf{J}_n} \right) = 0 \quad (2.5)$$

where  $\mathbf{J}_n$  is the Jacobian of the transformation (eqs. (2.3)). Under this transformation, the Bernoulli equation becomes

$$\rho = \left[ 1 + \frac{\gamma - 1}{2} \left( M_\infty^2 - 2\Phi_\tau - \mathbf{U}\Phi_\xi - \mathbf{V}\Phi_\eta \right) \right]^{1/(\gamma-1)} \quad (2.6)$$

where  $\mathbf{U}$  and  $\mathbf{V}$  are the contravariant velocity vectors, with  $\mathbf{U}$  being the velocity perpendicular to the  $\eta$  direction and  $\mathbf{V}$  being the velocity perpendicular to the  $\xi$  direction. In general these velocities are defined as

$$\begin{aligned} \mathbf{U} &= \xi_\tau + \mathbf{A}_1 \Phi_\xi + \mathbf{A}_2 \Phi_\eta \\ \mathbf{V} &= \eta_\tau + \mathbf{A}_2 \Phi_\xi + \mathbf{A}_3 \Phi_\eta \end{aligned} \quad (2.7)$$

where  $\mathbf{A}_1$ ,  $\mathbf{A}_2$ , and  $\mathbf{A}_3$  are metric terms defined as

$$\begin{aligned} \mathbf{A}_1 &= \nabla \xi \cdot \nabla \xi = \xi_x^2 + \xi_y^2 \\ \mathbf{A}_2 &= \nabla \xi \cdot \nabla \eta = \xi_x \eta_x + \xi_y \eta_y \\ \mathbf{A}_3 &= \nabla \eta \cdot \nabla \eta = \eta_x^2 + \eta_y^2 \end{aligned} \quad (2.8)$$

## 2.2. Computational Grid

For the present purposes, three characteristics are useful for the computational grid to have. The first characteristic is orthogonality, which is useful because it reduces the complexity of an algorithm. The second characteristic is that the grid lines conform closely to the shape of the airfoil; this increases the accuracy of the solution. The third characteristic is that the grid lines should align with the free stream away from the surface in order to facilitate the branch-cut method of modeling the vortex. For these reasons, an orthogonal H-mesh was chosen to be used

with the current method. The streamlines and potential lines which surround an airfoil in incompressible flow form such a grid. This type of grid may be computed by means of a complex mapping solution. The Joukowski airfoil transformation is used in the present method because it provides a convenient closed-form solution. The grid is generated with the following steps:

1. Produce a satisfactory stretched Cartesian grid using any method
2. Use the  $(\xi, \eta)$  coordinates along the front face of the grid to integrate  $\frac{d\eta}{d\xi}$  to the aft face of the grid (this solves for the streamlines around a circle)
3. Transform the circle solution by using the Joukowski transformation to produce the airfoil solution
4. Select an appropriate distribution of points along the airfoil “streamline”
5. Interpolate  $\Phi(\xi, \eta)$  to find the potential at each of these points
6. Find the location of each of the “off airfoil” streamlines which have matching potential values
7. Form the grid with the resulting set of points

The details of the development are presented in appendix A. Since the grid is orthogonal, the metric term  $\mathbf{A}_2$  is identically zero. Furthermore, since the grid is steady, the contravariant velocities become

$$\begin{aligned} \mathbf{U} &= \mathbf{A}_1 \Phi_\xi \\ \mathbf{V} &= \mathbf{A}_3 \Phi_\eta \end{aligned} \quad (2.9)$$

## 2.3. Metric Derivatives

The transformation of the equations to the computational plane gives rise to metric terms (i.e.,  $\xi_x$ ,  $\eta_y$ ) as a result of the chain rule. In matrix form, the chain rule expansion is

$$\begin{bmatrix} x_\tau & y_\tau & 1 \\ x_\xi & y_\xi & 0 \\ x_\eta & y_\eta & 0 \end{bmatrix} \begin{bmatrix} \partial_x \\ \partial_y \\ \partial_t \end{bmatrix} = \begin{bmatrix} \partial_\tau \\ \partial_\xi \\ \partial_\eta \end{bmatrix} \quad (2.10)$$

The determinant of the matrix is

$$D_n = x_\xi y_\eta - x_\eta y_\xi \quad (2.11)$$

Cramer's rule can be used to solve for

$$\left. \begin{aligned} \partial_x &= \frac{y_\eta \partial_\xi - y_\xi \partial_\eta}{D_n} \\ \partial_y &= \frac{x_\xi \partial_\eta - x_\eta \partial_\xi}{D_n} \end{aligned} \right\} \quad (2.12)$$

These expressions are applied to  $\xi$  and  $\eta$ , respectively, to obtain

$$\left. \begin{aligned} (\xi_x) &= \frac{y_\eta}{D_n} \\ (\eta_x) &= -\left(\frac{y_\xi}{D_n}\right) \\ (\xi_y) &= -\left(\frac{x_\eta}{D_n}\right) \\ (\eta_y) &= \frac{x_\xi}{D_n} \\ \mathbf{J}_n &= D_n^{-1} \end{aligned} \right\} \quad (2.13)$$

The terms  $y_\eta$ ,  $y_\xi$ ,  $x_\eta$ , and  $x_\xi$  are called the primitive metrics and are determined by the following simple central difference formulas (for convenience  $\Delta\xi = \Delta\eta = 1$ ):

$$\left. \begin{aligned} (x_\xi)_{i,j} &= \frac{(x_{i+1} - x_{i-1})}{2} \\ (y_\xi)_{i,j} &= \frac{(y_{i+1} - y_{i-1})}{2} \\ (x_\eta)_{i,j} &= \frac{(x_{j+1} - x_{j-1})}{2} \\ (y_\eta)_{i,j} &= \frac{(y_{j+1} - y_{j-1})}{2} \end{aligned} \right\} \quad (2.14)$$

At the airfoil boundaries, the derivatives in the  $\eta$  direction are computed with the aid of a pseudogrid line inside the airfoil contour. This grid line is determined with a simple linear extrapolation of the grid points off the airfoil.

## 2.4. Boundary Conditions

The four boundary conditions that are imposed on the flow are associated with (1) the airfoil surface, (2) the outer boundary of the grid, (3) the aft face of the grid, and (4) the Kutta condition.

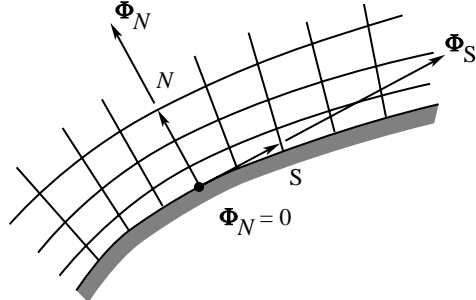
### 2.4.1. Airfoil Surface

For inviscid flow, the surface boundary condition requires that the flow be tangent to the airfoil surface. This requirement can be met by setting the contravariant velocity vector  $\mathbf{V}$  to zero. For a mesh

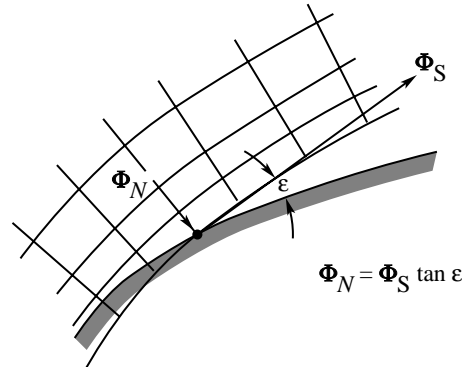
which exactly conforms to the airfoil, this leads to  $\Phi_\eta = 0$ . One problem with employing this boundary condition is that a new mesh must be generated with every new airfoil or airfoil orientation. An alternative to computing a new grid is to use a transpiration rather than a "no-flow" boundary condition. This approach uses a fixed grid which conforms to some convenient profile (e.g., a Joukowski airfoil) to approximate the desired profile. The flow must therefore pass through the grid surface at an angle  $\epsilon$ , which is the angular difference between the grid surface and the actual surface. Figure 4 illustrates this relationship. The flow normal to the grid surface  $\Phi_N$  is

$$\Phi_N = \Phi_S \tan \epsilon \quad (2.15)$$

where  $\Phi_S$  is the flow velocity tangent to the grid surface. This condition is merely a generalization of the usual small-disturbance boundary condition. The value of  $\Phi_\eta$  to be used in the actual algorithm remains to be found. Since the coordinate system is orthogonal, the only difference between the  $N$  and



(a) Flow tangency on body conforming coordinate.



(b) Flow-through condition on coordinate which approximates body (generalization of small-disturbance boundary condition).

Figure 4. Transpiration boundary condition at airfoil surface.

$\eta$  directions is a simple one-dimensional stretching; therefore,

$$\Phi_\eta = \frac{\Phi_N}{\eta_N} \quad (2.16)$$

#### 2.4.2. Outer Boundaries

Along the outer boundaries, the flow is required to return to undisturbed conditions. Often, computational outer boundaries are so close to the airfoil surface that this condition cannot produce an accurate or stable result. For these close-grid boundaries, special nonreflective boundary conditions are imposed. However, the current grid boundaries are sufficiently far away (155 chords horizontally and 80 chords vertically) that the assumption of undisturbed flow is valid. The outer boundary conditions are set with a Dirichlet condition

$$\Phi = M_\infty x \quad (2.17)$$

#### 2.4.3. Aft Face

Along the aft face of the mesh, the flow is also required to be undisturbed. However, because the present method employs a number of branch cuts (lines of potential discontinuity which model vorticity), the potential cannot be easily specified at this boundary. Instead free-stream conditions are imposed by modifying the outgoing flux along the aft

face so that  $\rho = 1$  is ensured. With the Bernoulli condition, the following expression for  $\Phi_\xi$  is derived (see appendix B):

$$\Phi_\xi = \frac{1}{\xi_x} \left( M_\infty - \frac{\Phi_\tau}{M_\infty} \right) \quad (2.18)$$

which is used in the flux computation.

#### 2.4.4. Kutta Condition

For the lifting conditions, allowance must be made for a jump in potential across a wakelike branch cut (Kutta condition). This cut extends from the airfoil trailing edge to the aft face of the mesh (which precludes the use of Dirichlet boundary conditions along the aft face). The cut is aligned with the mean chord line of the airfoil. In an unsteady flow, the jump in potential  $\Gamma$  across the cut must be convected downstream. The following equation, governing the convection of vorticity from the trailing edge, is derived by using the Bernoulli equation and continuity of density across the cut (see appendix B):

$$\Gamma_\tau + \langle \mathbf{U} \rangle \Gamma_\xi = 0 \quad (2.19)$$

where  $\langle \mathbf{U} \rangle$  is the average of the velocities above and below the branch cut. Equation (2.19) is used to determine the value of  $\Gamma$  along the branch cut.

### 2.5. Difference Equation

Two criteria are useful in developing the difference equation. The first criterion is that, at any current time step, the difference equation be a function of  $\Phi$  only. This criterion eliminates the need for solving a system of equations. The second criterion is that the conservation form be maintained. This criterion ensures an accurate computation of shock motion and strength.

Equation (2.5) may be written by using a backward difference in time as

$$\left( \frac{\rho}{\mathbf{J}_n} \right)^{N+1} - \left( \frac{\rho}{\mathbf{J}_n} \right)^N + \Delta t^{N+1} \left[ \left( \frac{\rho \mathbf{U}}{\mathbf{J}_n} \right)_\xi^{N+1} + \left( \frac{\rho \mathbf{V}}{\mathbf{J}_n} \right)_\eta^{N+1} \right] = 0 \quad (2.20)$$

This difference equation maintains the conservation form, but the density still remains at the  $(N+1)$  time level; this can be corrected by expanding the density in a Taylor series expansion as

$$\rho^{N+1} = \rho^N + \frac{\partial \rho^N}{\partial \Phi} (\Phi^{N+1} - \Phi^N) \quad (2.21)$$

The operator  $\frac{\partial \rho}{\partial \Phi}$  is derived from the Bernoulli equation and is expressed in the following conventional form:

$$\left( \frac{\partial \rho}{\partial \Phi} \right)^N \equiv -\rho^{2-\gamma} \left( \frac{\partial}{\partial \tau} + \frac{\mathbf{U} \partial}{\partial \xi} + \frac{\mathbf{V} \partial}{\partial \eta} \right)^N \quad (2.22)$$

A complete derivation of equation (2.22) is provided in appendix C for students who may be unfamiliar with the form. The Taylor series must be taken on both the  $\rho^{N+1}$  and  $\rho^N$  terms in order to maintain conservation form. Application of the appropriate time derivatives  $\partial\tau$  leads to the following *differential* equation:

$$\begin{aligned} \left(\frac{\rho}{\mathbf{J}_n}\right)^{N+1} - \left(\frac{\rho}{\mathbf{J}_n}\right)^N &= \Delta t^N \rho_\tau^N - \left(\frac{\beta}{\mathbf{J}_n}\right)^N [\Phi_{\tau\tau} + \mathbf{U}\Phi_{\xi\tau} + \mathbf{V}\Phi_{\eta\tau}]^N \\ &\quad - \left(\frac{\beta}{\mathbf{J}_n}\right)^{N-1} [\Phi_{\tau\tau} + \mathbf{U}\Phi_{\xi\tau} + \mathbf{V}\Phi_{\eta\tau}]^{N-1} \end{aligned} \quad (2.23)$$

The terms in brackets in equation (2.23) are seen to have a form similar to the time derivatives in the following nonconservative full-potential equation:

$$\Phi_{\tau\tau} + 2\mathbf{U}\Phi_{\xi\tau} + 2\mathbf{V}\Phi_{\eta\tau} = \mathbf{A}_1 (\rho^{\gamma-1} - \mathbf{A}_1 \Phi_\xi^2) \Phi_{\xi\xi} + \mathbf{A}_3 (\rho^{\gamma-1} - \mathbf{A}_3 \Phi_\eta^2) \Phi_{\eta\eta} - 2\mathbf{U}\mathbf{V}\Phi_{\eta\xi} \quad (2.24)$$

Indeed, the term

$$\mathbf{C}^* = \Delta t^N \rho_\tau^N - \beta^{N-1} [\Phi_{\tau\tau} + \mathbf{A}_1 \Phi_\xi \Phi_{\xi\tau} + \mathbf{A}_3 \Phi_\eta \Phi_{\eta\tau}]^{N-1} \quad (2.25)$$

can be thought of as a conservation correction to the equation. This term affects both the mass conservation and time accuracy of the equation. Substituting equation (2.21) into equation (2.20) now yields

$$\begin{aligned} &- \left(\frac{\beta}{\mathbf{J}_n}\right)^N [(\Phi^{N+1} - \Phi^N) + (\Phi^N - \Phi^{N-1}) + \mathbf{U}^N \Phi_\xi (\Phi_\xi^{N+1} - \Phi_\xi^N) + \mathbf{V}^N \Phi_\eta (\Phi_\eta^{N+1} - \Phi_\eta^N)] \\ &+ \Delta t^{N+1} \left[ \delta_\xi \left(\frac{\rho}{\mathbf{J}_n} \mathbf{U}\right)^{N+1} + \delta_\eta \left(\frac{\rho}{\mathbf{J}_n} \mathbf{V}\right)^{N+1} \right] + \mathbf{C}^*(\rho^N, \rho^{N-1}, \Phi^N, \Phi^{N-1}, \Phi^{N-2}) = 0 \end{aligned} \quad (2.26)$$

The density in the space terms in equation (2.26) can be computed at the N time step with an error of only  $\Delta t$ . For convenience the space terms are written in “delta” form. For example, the streamwise flux term is written

$$\delta_\xi \left(\frac{\rho}{\mathbf{J}_n} \mathbf{U}\right)^{N+1} = \delta_\xi \left(\frac{\rho}{\mathbf{J}_n}\right)^N \mathbf{A}_1 \delta_\xi (\Phi^{N+1} - \Phi^N) + \delta_\xi \left(\frac{\rho}{\mathbf{J}_n} \mathbf{U}\right)^N \quad (2.27)$$

After applying the delta form, dividing through by  $-(\hat{\beta}\Delta t^N)$ , and collecting terms, equation (2.26) becomes

$$\begin{aligned} &\left[ \mathbf{I} + \Delta t^N \mathbf{A}_1 \Phi_\xi^N \delta_\xi + \Delta t^N \mathbf{A}_3 \Phi_\eta \delta_\eta - \Delta t^N \Delta t^{N+1} \left(\frac{\mathbf{J}_n}{\beta^N}\right) \delta_\xi \left(\frac{\mathbf{A}_1}{\mathbf{J}_n}\right) \rho^N \delta_\xi \right. \\ &\quad \left. - \Delta t^N \Delta t^{N+1} \left(\frac{\mathbf{J}_n}{\beta^N}\right) \delta_\eta \left(\frac{\mathbf{A}_3}{\mathbf{J}_n}\right) \rho^N \delta_\eta \right] (\Phi^{N+1} - \Phi^N) \\ &= \left(\frac{\mathbf{J}_n}{\beta^N}\right) \Delta t^N \Delta t^{N+1} \left[ \delta_\xi \left(\frac{\mathbf{A}_1}{\mathbf{J}_n}\right) \rho^N \delta_\xi \Phi^N + \delta_\eta \left(\frac{\mathbf{A}_3}{\mathbf{J}_n}\right) \rho^N \delta_\eta \Phi^N \right] \\ &\quad + \left(\frac{\beta^{N-1}}{\beta^N}\right) \left(\frac{\Delta t^N}{\Delta t^{N-1}}\right) (\Phi^N - 2\Phi^{N-1} + \Phi^{N-2}) + (\Phi^N - \Phi^{N-1}) \\ &\quad + \left(\frac{\beta^{N-1}}{\beta^N}\right) \Delta t^N [\mathbf{A}_1 \Phi_\xi^{N-1} \delta_\xi + \mathbf{A}_3 \Phi_\eta^{N-1} \delta_\eta] (\Phi^N - \Phi^{N-1}) + \left(\frac{\mathbf{J}_n}{\beta^N}\right) \Delta t^N (\hat{\rho}^N - \hat{\rho}^{N-1}) \end{aligned} \quad (2.28)$$

Equation (2.28) may be written in the following compact form:

$$\mathbf{L}(\Phi^{N+1} - \Phi^N) = \mathbf{R}^*(\rho^N, \Phi^N) + (\Phi^N - \Phi^{N-1}) + \mathbf{C}^*(\rho^N, \rho^{N-1}, \Phi^N, \Phi^{N-1}, \Phi^{N-2}, \beta^N, \beta^{N-1}) \quad (2.29)$$

where

$$\mathbf{R}^* = \left( \frac{\mathbf{J}_n}{\beta^N} \right) \Delta t^N \Delta t^{N+1} \left[ \delta_\xi \left( \frac{\mathbf{A}_1}{\mathbf{J}_n} \right) \delta_\xi \Phi^N + \delta_\eta \left( \frac{\mathbf{A}_3}{\mathbf{J}_n} \right) \delta_\eta \Phi^N \right] \quad (2.30)$$

and

$$\begin{aligned} \mathbf{C}^* = & \left( \frac{\beta^{N-1}}{\beta^N} \right) \left( \frac{\Delta t^N}{\Delta t^{N-1}} \right) (\Phi^N - 2\Phi^{N-1} + \Phi^{N-2}) + \left( \frac{\mathbf{J}_n}{\beta^N} \right) \Delta t^N (\hat{\rho}^N - \hat{\rho}^{N-1}) \\ & + \left( \frac{\beta^{N-1}}{\beta^N} \right) \Delta t^N [\mathbf{A}_1 \Phi_\xi^{N-1} \delta_\xi + \mathbf{A}_3 \Phi_\eta^{N-1} \delta_\eta] (\Phi^N - \Phi^{N-1}) \end{aligned} \quad (2.31)$$

The left-hand side term  $\mathbf{L}$  is simply the time update term which arises from the delta form of the equation. The term  $\Delta \Phi^N$  actually arises from the left-hand side operator but is placed on the right-hand side for operational reasons,  $\mathbf{R}^*$  is the spatial flux evaluated at time step N, and  $\mathbf{C}^*$  is the conservation correction term.

## 2.6. Implementing the Algorithm

### 2.6.1. Basic Difference Operators

Equation (2.28) must now be implemented. The basic difference operator for time is

$$\delta_\tau \Phi = \frac{\Phi^{N+1} - \Phi^N}{\Delta t^{N+1}} = \Phi_\tau \quad (2.32)$$

The velocity term  $\Phi_\xi$ , which is used in the computation of  $\mathbf{L}$  and  $\mathbf{R}$ , is formed with a central difference

$$(\Phi_\xi)_i = \frac{\Phi_{i+1} - \Phi_{i-1}}{2} \quad (2.33)$$

The computation of the corresponding  $\Phi_\eta$  term must allow for jumps in  $\Phi$  across branch cuts. For convenience, the grid is assumed to be permeated with horizontal branch cuts which lie slightly above the grid points. Each grid point has a jump in potential  $\Gamma$  associated with it. The value of  $\Gamma$  is zero everywhere except along an actual branch cut. A difference expression which accounts for this field of branch cuts is

$$(\Phi_\eta)_j = \frac{1}{2} [\Phi_{j+1} - (\Phi_j + \Gamma_j) + \Phi_j - (\Phi_{j-1} + \Gamma_{j-1})] \quad (2.34)$$

Figure 5 illustrates the velocity computation near a vortex branch cut.

### 2.6.2. Flux Operator Differencing

Each of the spatial flux terms is made up of the product of three terms: (1) a velocity term, (2) a density term, and (3) a metric term. This product, which is the local mass flux, is computed at the midpoint between two grid nodes. The velocity term is computed by using a one-sided difference

$$(\Phi_\xi)_{i+(1/2)} = \Phi_{i+1} - \Phi_i \quad (2.35)$$

*2.6.2.1. Flux density term (switching).* The density terms are used to aid the stability of the algorithm. Because the HSI problem is transonic, the type of the equation will change from elliptic to hyperbolic depending on local Mach number. Stability is achieved by switching the type of operator with the equation type. To illustrate the requirement for switching, consider the following two-dimensional equation:

$$(1 - M_\infty^2) \Phi_{xx} + \Phi_{yy} = 0 \quad (2.36)$$

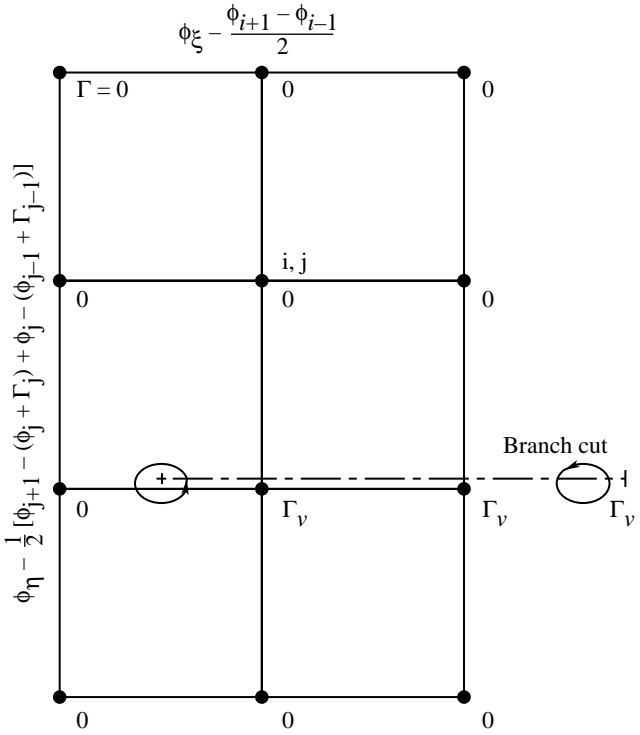


Figure 5. Computation of velocity at grid point in field permeated with branch cuts.

We define operators such that

$$\nabla_x \Phi_i = \frac{\Phi_i - \Phi_{i-1}}{\Delta x} \quad (2.37a)$$

$$\Delta_x \Phi_i = \frac{\Phi_{i+1} - \Phi_i}{\Delta x} \quad (2.37b)$$

It has long been recognized that the scheme

$$(1 - M_\infty^2) \nabla_x \Delta_x \Phi + \nabla_y \Delta_y \Phi = 0 \quad (2.38)$$

is stable for  $M_\infty < 1$ , and that

$$(1 - M_\infty^2) \nabla_x \nabla_x \Phi + \nabla_y \Delta_y \Phi = 0 \quad (2.39)$$

is stable for  $M_\infty > 1$ . A problem arises when we try to use either of these schemes alone for a transonic flow. Equation (2.39) is divergent if  $M_\infty < 1$  and equation (2.38) is convergent for  $M_\infty > 1$  only if

$$\left| \frac{\Delta_x}{(1 - M_\infty^2) \Delta_y} \right| \leq 1$$

which is impractical for  $M_\infty$  near 1. Stability is achieved by switching from equation (2.38) to equation (2.39) depending on local Mach number. In the present algorithm, this switching would lead to a complex matrix form which is costly to evaluate. However, Holst and Ballhaus (ref. 19) introduced another type of switching which is well suited to the conservative form of the equation and reduces the complexity of the matrix. In their scheme, the density is evaluated centered in midcell for subsonic flow. For supersonic flow the density is upwind biased, that is, evaluated at the upstream cell center. (See sketch A.) A parameter is then employed

Spacial differencing and stability:

Stable difference for spacial flux in subsonic flow is

$$(\rho\phi_x)_x = \nabla(\rho_{i+1/2}\Delta\phi) \quad \begin{array}{c} \xrightarrow{\hspace{1cm}} \\ \bullet - \overset{\curvearrowright}{\underset{\curvearrowleft}{\underset{\curvearrowright}{x}}} - \overset{\curvearrowright}{\underset{\curvearrowleft}{\underset{\curvearrowright}{x}}} - \bullet \end{array} \quad \begin{array}{l} i-1 \quad i \quad i+1 \\ \swarrow (\rho_{i+1/2} = \frac{1}{2}(\rho_i + \rho_{i+1})) \end{array}$$

Centered difference:

Stability in supersonic regions requires upwing biasing and a simple way to accomplish this is

$$(\rho\phi_x)_x = \nabla(\rho_{i+1/2}\Delta\phi) \quad \begin{array}{c} \xrightarrow{\hspace{1cm}} \\ \bullet - \overset{\curvearrowright}{\underset{\curvearrowleft}{\underset{\curvearrowright}{x}}} - \overset{\curvearrowright}{\underset{\curvearrowleft}{\underset{\curvearrowright}{x}}} - \bullet \end{array} \quad \begin{array}{l} i-1 \quad i \quad i+1 \\ \swarrow \rho_{i-3/2} \quad \swarrow \rho_{i-1/2} \end{array}$$

This remains a centered scheme;  $\rho$  is shifted however

Sketch A

which switches the density from centered to upstream based on the local Mach number. The flux (without the metric term for simplicity) is

$$\begin{aligned} \delta_\xi(\rho\delta_\xi\Phi) &= \left[ (1 - \nu_i) \frac{\rho_{i+1} + \rho_i}{2} + \nu_i \frac{\rho_i + \rho_{i-1}}{2} \right] (\Phi_{i+1} - \Phi_i) \\ &\quad - \left[ (1 - \nu_{i-1}) \frac{\rho_i + \rho_{i-1}}{2} + \nu_{i-1} \frac{\rho_{i-1} + \rho_{i-2}}{2} \right] (\Phi_i - \Phi_{i-1}) \end{aligned} \quad (2.40)$$

The switching parameter  $\nu$  is defined as

$$\left. \begin{array}{ll} \nu_i^* = \left(1 - \frac{\rho_i}{\rho^*}\right) C & (1 \leq C \leq 10) \\ \nu = 0 & (\nu^* < 0 \text{ (subsonic)}) \\ \nu = 1 & (\nu^* > 1 \text{ (supersonic)}) \end{array} \right\} \quad (2.41)$$

The parameter  $C$  is used to provide additional numerical viscosity in the supersonic region. The form of  $C$  is completely arbitrary. In the present method,  $C$  is varied linearly with the local Mach number  $M_l$ , by using the following equation:

$$C = 16M_l - 10.8$$

where this form was determined by numerical experiment. The critical density  $\rho^*$  is determined with the free-stream Mach number as

$$\rho^* = \left[ \frac{2}{\gamma+1} \left( 1 + \frac{\gamma-1}{2} M_\infty \right) \right]^{1/(\gamma-1)}$$

*2.6.2.2. Flux metric term (consistent differencing).* Computation of the flux metric terms poses a special problem. The flux metric term is

$$\left( \frac{\mathbf{A}_1}{\mathbf{J}_n} \right)_{i+1/2} = \left( \frac{\xi_x^2 + \xi_y^2}{\mathbf{J}_n} \right)_{i+1/2} \quad (2.42)$$

The simplest method of evaluating this is to average the values at the nodes so that

$$\left( \frac{\mathbf{A}_1}{\mathbf{J}_n} \right)_{i+1/2} = \frac{\left( \frac{\xi_x^2 + \xi_y^2}{\mathbf{J}_n} \right)_{i+1} + \left( \frac{\xi_x^2 + \xi_y^2}{\mathbf{J}_n} \right)_i}{2} \quad (2.43)$$

This evaluation can lead to an error for a grid with stretching. The error occurs because the values  $\xi_x$  and  $\eta_y$  are computed by using central differences (eqs. (2.13) and (2.14)), and therefore, information from node  $(i-1)$  to  $(i+2)$  is used to compute the metric term at  $(i+1/2)$ . This “extra” data acts to reduce the accuracy of the metric computation especially for regions where the metrics change rapidly. The effect of the diminished accuracy is to introduce an artificial mass into the flux computation. The extra mass can be removed by the use of a free-stream subtraction matrix. This matrix is generated by specifying free-stream conditions on the mesh ( $\Phi = M_\infty x$ ) and computing the value of  $\mathbf{R}_\infty = \mathbf{R}(\Phi = M_\infty x)$ . The matrix  $\mathbf{R}_\infty$  is then subtracted from  $\mathbf{R}$  in subsequent computations to restore the mass balance.

Flores et al. (ref. 20) recently proposed a superior method of computing the metric which eliminates this problem. Their method involves calculating the flux metric terms at the same points in space at which the flux is differenced. The method is referred to as the “consistent-metric method.” Consider, for example, the incompressible mass conservation equation which must hold for the free-stream subtraction to be zero

$$\left( \frac{\mathbf{A}_1 \Phi_\xi}{\mathbf{J}_n} \right)_\xi + \left( \frac{\mathbf{A}_3 \Phi_\eta}{\mathbf{J}_n} \right)_\eta = 0 \quad (2.44)$$

Here, the density is set to 1, and from the chain rule,

$$\left. \begin{aligned} \Phi_\xi &= \frac{1}{\xi_x} (\Phi_x - \eta_x \Phi_\eta) = \frac{1}{\eta_y} (\Phi_y - \eta_y \Phi_\eta) \\ \Phi_\eta &= \frac{1}{\eta_x} (\Phi_x - \xi_x \Phi_\xi) = \frac{1}{\xi_y} (\Phi_y - \xi_y \Phi_\xi) \end{aligned} \right\} \quad (2.45)$$

With equations (2.45) and (2.13), equation (2.44) becomes, for free-stream conditions,

$$M_\infty (y_{\eta\xi} - y_{\xi\eta}) = 0 \quad (2.46)$$

It therefore follows that the metric difference operators must commute in order to produce a zero free-stream subtraction. For this method, the primitive metrics (in the  $\xi$  direction) are computed by using a backward difference

$$\left. \begin{aligned} \tilde{x}_{\xi_{i+1/2,j}} &= x_{i+1} - x_i \\ \tilde{y}_{\xi_{i+1/2,j}} &= y_{i+1} - y_i \end{aligned} \right\} \quad (2.47)$$

the  $\eta$  derivatives are

$$\left. \begin{aligned} \tilde{x}_{\eta_{i+1/2,j}} &= \frac{1}{2} \left[ \left( \frac{x_{j+1} - x_{j-1}}{2} \right)_{i+1} + \left( \frac{x_{j+1} - x_{j-1}}{2} \right)_i \right] \\ \tilde{y}_{\eta_{i+1/2,j}} &= \frac{1}{2} \left[ \left( \frac{y_{j+1} - y_{j-1}}{2} \right)_{i+1} + \left( \frac{y_{j+1} - y_{j-1}}{2} \right)_i \right] \end{aligned} \right\} \quad (2.48)$$

The determinant  $D_m$  is

$$D_m = \tilde{x}_\xi \tilde{y}_\eta - \tilde{x}_\eta \tilde{y}_\xi \quad (2.49)$$

and

$$\left. \begin{aligned} \tilde{\xi}_x &= \frac{\tilde{y}_\eta}{D_m} \\ \tilde{\eta}_x &= -\left(\frac{\tilde{y}_\xi}{D_m}\right) \\ \tilde{\xi}_y &= -\left(\frac{\tilde{x}_\eta}{D_m}\right) \\ \tilde{\eta}_y &= \frac{\tilde{x}_\xi}{D_m} \\ \mathbf{J}_m &= D_m^{-1} \end{aligned} \right\} \quad (2.50)$$

The flux metric term becomes

$$\left(\frac{\mathbf{A}_1}{\mathbf{J}_n}\right)_{i+1/2} = \frac{\tilde{\xi}_x^2 + \tilde{\xi}_y^2}{\mathbf{J}_m} \quad (2.51)$$

The metric term  $\left(\frac{\mathbf{A}_3}{\mathbf{J}_n}\right)_{j+1/2}$  is computed in an analogous fashion.

The consistent difference therefore localizes the computation of the metric; thus, the extraneous data are eliminated from the computation. Therefore, three sets of metrics exist: one each for the  $\xi$  and  $\eta$  flux terms and one at the nodes. Although the consistent metric method requires more storage space and complicates the coding, it provides a more robust method of computing the metrics and has been incorporated in the present method. The final form of the flux term is

$$\begin{aligned} \delta_\xi[\rho \mathbf{A}_1 \delta_\xi \Phi] &= \left[ (1 - \nu_i) \frac{\rho_{i+1} + \rho_i}{2} + \nu_i \frac{\rho_i + \rho_{i-1}}{2} \right] \left(\frac{\mathbf{A}_1}{\mathbf{J}_n}\right)_{i+1/2} (\Phi_{i+1} - \Phi_i) \\ &\quad - \left[ (1 - \nu_{i-1}) \frac{\rho_i + \rho_{i-1}}{2} + \nu_{i-1} \frac{\rho_{i-1} + \rho_{i-2}}{2} \right] \left(\frac{\mathbf{A}_1}{\mathbf{J}_n}\right)_{i-1/2} (\Phi_i - \Phi_{i-1}) \end{aligned} \quad (2.52)$$

Equations (2.52), (2.41), (2.40), (2.35), (2.34), (2.33), and (2.32) are used in the implementation of equation (2.28).

### 2.6.3. Approximate Factorization

A noncompact matrix inversion as follows is still required to solve equation (2.29):

$$\mathbf{L} \Delta \Phi^{N+1} = \mathbf{R}^N$$

In order to reduce the matrix to compact form, the operator  $\mathbf{L}$  is approximately factored. The equation becomes

$$\mathbf{L}_\eta \mathbf{L}_\xi \Delta \Phi^{N+1} = \mathbf{R}^N \quad (2.53)$$

The operators  $\mathbf{L}_\xi$  and  $\mathbf{L}_\eta$  are chosen so that (1) their product is approximately equal to  $\mathbf{L}$  (to within an error which does not exceed the discretization error), (2) only simple matrix operations are required to obtain the solution, and (3) the overall scheme is stable. The present method uses factors which are associated with the two space derivatives, and this leads to an ADI type scheme. The factor  $\mathbf{L}_\eta$  is

$$\mathbf{L}_\eta = \left[ \mathbf{I} + \Delta t^N \mathbf{A}_3 \Phi_\eta^N \delta_\eta - \Delta t^N \Delta t^{N+1} \left( \frac{\mathbf{J}_n}{\beta^N} \right) \partial_\eta \left( \frac{\mathbf{A}_3}{\mathbf{J}} \right) \rho^N \partial_\eta \right] \quad (2.54)$$

The form of  $\mathbf{L}_\xi$  is similar. The final form of equation (2.29) is

$$\begin{aligned}
& \left[ \mathbf{I} + \Delta t^N \mathbf{A}_3 \Phi_\eta \delta_\eta - \Delta t^N \Delta t^{N+1} \left( \frac{\mathbf{J}_n}{\beta^N} \right) \partial_\eta \left( \frac{\mathbf{A}_3}{\mathbf{J}_n} \right) \rho^N \partial_\eta \right] \\
& \times \left[ \mathbf{I} + \Delta t^N \mathbf{A}_1 \Phi_\xi \delta_\xi - \Delta t^N \Delta t^{N+1} \left( \frac{\mathbf{J}_n}{\beta^N} \right) \partial_\xi \left( \frac{\mathbf{A}_1}{\mathbf{J}_n} \right) \rho^N \partial_\xi \right] (\Phi^{N+1} - \Phi^N) \\
& = \left( \frac{\mathbf{J}_n}{\beta^N} \right) \Delta t^N \Delta t^{N+1} \left[ \delta_\xi \left( \frac{\mathbf{A}_1}{\mathbf{J}_n} \right) \rho^N \delta_\xi \Phi^N + \delta_\eta \left( \frac{\mathbf{A}_3}{\mathbf{J}_n} \right) \rho^N \delta_\eta \Phi^N \right] \\
& + (\Phi^N - \Phi^{N-1}) + \left( \frac{\beta^{N-1}}{\beta^N} \right) \left( \frac{\Delta t^N}{\Delta t^{N-1}} \right) (\Phi^N - 2\Phi^{N-1} + \Phi^{N-2}) \\
& + \left( \frac{\beta^{N-1}}{\beta^N} \right) \Delta t^N \left[ \mathbf{A}_1 \Phi_\xi^{N-1} \delta_\xi + \mathbf{A}_3 \Phi_\eta^{N-1} \delta_\eta \right] (\Phi^N - \Phi^{N-1}) + \left( \frac{\mathbf{J}_n}{\beta^N} \right) \Delta t^N (\hat{\rho}^N - \hat{\rho}^{N-1}) \quad (2.55)
\end{aligned}$$

Both operators  $\mathbf{L}_\xi$  and  $\mathbf{L}_\eta$  yield tridiagonal matrices. For example,

$$\mathbf{L}_\eta \Phi^* = \mathbf{A} \Phi_{j-1}^* + \mathbf{B} \Phi_j^* + \mathbf{C} \Phi_{j+1}^* \quad (2.56)$$

where

$$\left. \begin{aligned}
\mathbf{A} &= \left[ \frac{-\Delta t^N \mathbf{A}_3 \Phi_\eta^N}{2} - \Delta t^N \Delta t^{N+1} \left( \frac{\mathbf{J}_n}{\beta^N} \right) \left( \frac{\mathbf{A}_3}{\mathbf{J}_n} \right)_{j-1/2} \frac{\rho_j + \rho_{j-1}}{2} \right] \\
\mathbf{B} &= \left[ 1 + \Delta t^N \Delta t^{N+1} \left( \frac{\mathbf{J}_n}{\beta^N} \right) \left( \frac{\mathbf{A}_3}{\mathbf{J}_n} \right)_{j+1/2} \frac{\rho_{j+1} + \rho_j}{2} \right. \\
&\quad \left. + \Delta t^N \Delta t^{N+1} \left( \frac{\mathbf{J}_n}{\beta^N} \right) \left( \frac{\mathbf{A}_3}{\mathbf{J}_n} \right)_{j-1/2} \frac{\rho_j + \rho_{j-1}}{2} \right] \\
\mathbf{C} &= \left[ \frac{\Delta t^N \mathbf{A}_3 \Phi_\eta^N}{2} - \Delta t^N \Delta t^{N+1} \left( \frac{\mathbf{J}_n}{\beta^N} \right) \left( \frac{\mathbf{A}_3}{\mathbf{J}_n} \right)_{j+1/2} \frac{\rho_{j+1} + \rho_j}{2} \right]
\end{aligned} \right\} \quad (2.57)$$

#### 2.6.4. Implementing Boundary Conditions

The boundary conditions are implemented implicitly in the algorithm. This implementation will require modifications to both the right- and left-hand sides of the  $\eta$  sweep of the equation. For the upper surface of the airfoil, the operator  $\mathbf{L}_\eta$  becomes

$$\mathbf{L}_\eta \Phi^* = \Phi_j^* + \frac{\Delta t^{N+1} \mathbf{A}_3 \Phi_\eta \Delta S_u}{2} - \frac{\Delta t^N \Delta t^{N+1}}{\beta^N} \left[ \left( \frac{\mathbf{A}_3}{\mathbf{J}_n} \right)_{j+(1/2)} \frac{\rho_{j+1} + \rho_j}{2} (\Phi_{j+1} - \Phi_j) - \left( \frac{\mathbf{A}_3}{\mathbf{J}_n} \right)_S \rho_S \Delta S_u \right] \quad (2.58)$$

Here the term  $\Delta S_u$  refers to the change in velocity on the upper surface from time  $N$  to  $N+1$ . Because this is a known quantity, it can be brought to the right-hand side. The equation then becomes

$$\begin{aligned}
\mathbf{A} \Phi_{j-1}^* + \mathbf{B} \Phi_j^* + \mathbf{C} \Phi_{j+1}^* &= \hat{\mathbf{R}} + \Delta S^{N-1} \Delta t^N \mathbf{A}_3 \Phi_\eta^{N-1} \frac{\beta^{N-1}}{\beta^N} - \left( \frac{\mathbf{J}_n}{\beta^N} \right) \Delta t^N \Delta t^{N+1} \left( \frac{\mathbf{A}_3}{\mathbf{J}_n} \right)_S \rho_S S_u \\
&\quad - \Delta t^N \mathbf{A}_3 \Phi_\eta \Delta S_u^N - \Delta t^N \Delta t^{N+1} \left( \frac{\mathbf{J}_n}{\beta^N} \right) \left( \frac{\mathbf{A}_3}{\mathbf{J}_n} \right)_S \rho_S \Delta S_u^N \quad (2.59)
\end{aligned}$$

where

$$\mathbf{A} = 0$$

$$\mathbf{B} = \left[ 1 + \frac{\Delta t^{N+1} \Delta t^N}{\beta^N} \left( \frac{\mathbf{A}_3}{\mathbf{J}_n} \right)_{j+1/2} \frac{\rho_{j+1} + \rho_j}{2} \right]$$

$$\mathbf{C} = - \left[ \frac{\Delta t^{N+1} \Delta t^N}{\beta^N} \left( \frac{\mathbf{A}_3}{\mathbf{J}_n} \right)_{j+1/2} \frac{\rho_{j+1} + \rho_j}{2} \right]$$

$\hat{\mathbf{R}}$  represents that portion of the right-hand side which is unchanged at the boundary, and the subscript  $u$  refers to the upper surface conditions. The modification on the lower surface is similar to that on the upper surface and can be determined by symmetry.

### 2.6.5. Solution Steps

The solution is obtained in three steps by the following equations:

$$\mathbf{L}_\eta \Phi^* = \mathbf{R} \quad (2.60)$$

$$\mathbf{L}_\xi \Delta \Phi^{N+1} = \Phi^* \quad (2.61)$$

$$\Phi^{N+1} = \Phi^N + \Delta \Phi^{N+1} \quad (2.62)$$

The value  $\Phi^{N+1}(\xi, \eta)$  is the solution of the full-potential equation for the flow about the airfoil at the next time step. Given this solution, the velocity and pressure on the airfoil surface may be calculated. The vortex model is introduced as a modification to either the boundary conditions or the basic algorithm.

## 2.7. Steady-State Algorithm

A special form of the algorithm is employed in the solution of a steady problem. For steady problems, equation (2.55) is modified to remove all temporal terms and the resulting equation is solved with pseudo time terms which act to update the solution. Equation (2.55) becomes

$$\begin{aligned} & \left[ \mathbf{I} - \Delta t^N \left( \frac{\mathbf{J}_n}{\beta^N} \right) \partial_\eta \left( \frac{\mathbf{A}_3}{\mathbf{J}_n} \right) \rho^N \partial_\eta \right] \left[ \mathbf{I} - \Delta t^N \left( \frac{\mathbf{J}_n}{\beta^N} \right) \partial_\xi \left( \frac{\mathbf{A}_1}{\mathbf{J}_n} \right) \rho^N \partial_\xi \right] (\Phi^{N+1} - \Phi^N) \\ &= \left( \frac{\mathbf{J}_n}{\beta^N} \right) \Delta t^N \left[ \delta_\xi \left( \frac{\mathbf{A}_1}{\mathbf{J}_n} \right) \rho^N \delta_\xi \Phi^N + \delta_\eta \left( \frac{\mathbf{A}_3}{\mathbf{J}_n} \right) \rho^N \delta_\eta \Phi^N \right] \end{aligned} \quad (2.63)$$

The value of  $\Delta t^N$  is then oscillated for a number of time steps. Each successive value of  $\Delta t$  acts to reduce the magnitude of the error in a limited frequency range. By oscillating  $\Delta t$ , the error for a wide range of frequencies is reduced to make the most efficient use of each computational sweep. With this method, approximately 400 “time steps” are required to drive the residual to an acceptable value, whereas 2000 steps are required with the full algorithm (with all the time terms included).

The residual is determined by the following steps:

1. Compute the value of  $\mathbf{R}$  at the first step
2. Survey  $\mathbf{R}$  to obtain its maximum local value  $\mathbf{R}_1$
3. At each subsequent computational step, obtain  $\mathbf{R}_n$  (the maximum local value of  $\mathbf{R}$ )
4. Determine the value of  $\mathbf{R}_n/\mathbf{R}_1$  which is the normalized residual

When this value reaches  $10^{-4}$  the computation has converged.

### 3. Vortex Models

In section 2, an algorithm for solving for the potential flow field around an airfoil in transonic flow was presented. This algorithm is now modified to include the effect of a two-dimensional vortex passing near the airfoil. The four models for the vortex discussed in section 1.3 are used: the angle-of-attack method, the lifting-surface method, the branch-cut method, and the split-potential method. These methods may be grouped into two categories. (See fig. 6.)

The first category called the surface-specification methods model the effect of the vortex as an imposed normal velocity distribution on the airfoil surface. Both the angle-of-attack and lifting-surface methods fall into this category. These methods originated within linear-integral rotor theories. The effect of the vortex on the general flow field is usually not considered in these theories. These models are valid for linear flow fields.

For problems characterized by the transonic non-linearity (that is, with a speed of sound that varies

throughout the flow field), a surface effect cannot completely model the effect of the vortex; therefore, it is necessary to insert the vortex explicitly into the grid. This category is called explicit models; both the branch-cut and split-potential models fall into this category.

The vortex modeling begins with the ideal two-dimensional vortex potential:

$$\mathbf{G} = \frac{\Gamma}{2\pi} \theta \quad (3.1)$$

where  $\theta$  is the angle subtended by the vortex and the field point. The tangential velocity at the field point is

$$V_\theta = \frac{\Gamma}{2\pi r} \quad (3.2)$$

The singularity at  $r = 0$  is the source of numerical instabilities and requires the use of an artificial core. In the following tasks, the model developed by Scully (ref. 21) given in the following equation is used:

$$V_\theta = \frac{\Gamma}{2\pi r} \left( \frac{r^2}{r^2 + a^2} \right) \quad (3.3)$$

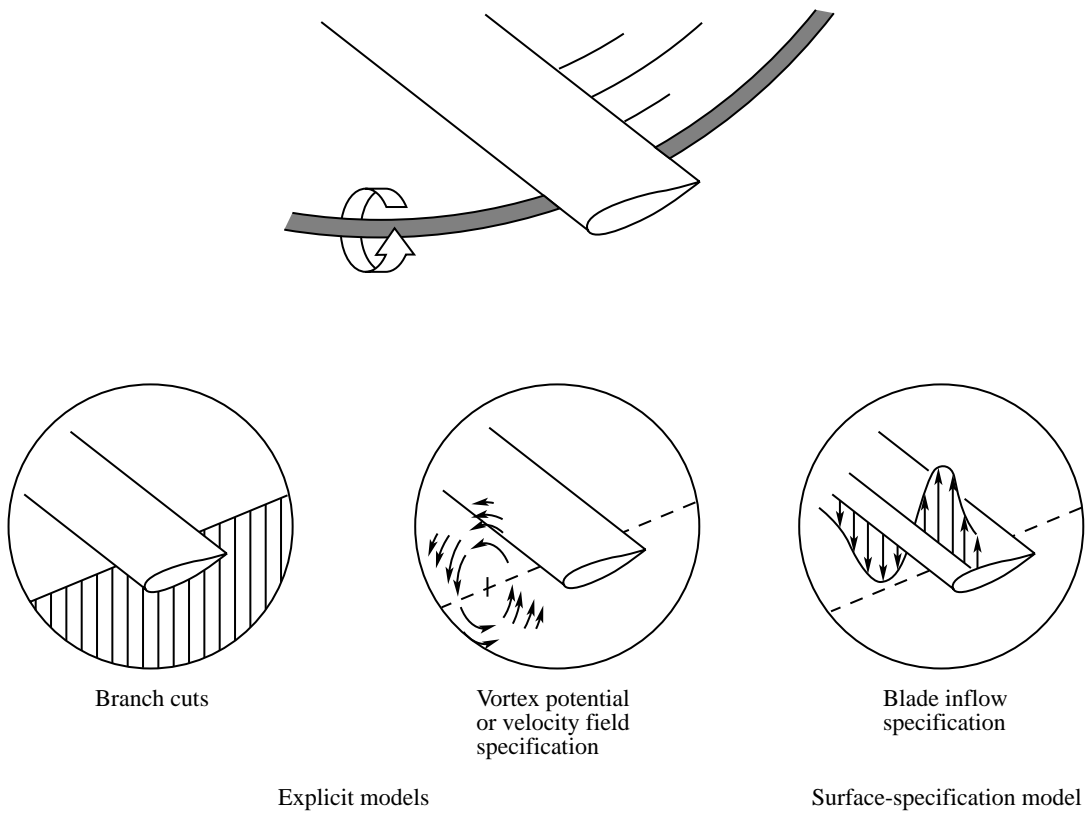


Figure 6. Principal vortex models.

where  $a$  is the vortex “core” radius. The word core is used in the conventional sense that is used in the helicopter industry; that is, it refers to a region of rotational flow near the vortex center of rotation. This rotational flow may be restricted to a discrete region in some models or it may be modeled by a decay function as in equation (3.3). The radius  $a$  defines the region in which the flow is rotational; within this region, the potential equation model of the vortex is invalid.

The vortex is moved through the computational grid by integrating the flow velocity at the vortex over the current time step

$$\left. \begin{aligned} X_v^{N+1} &= X_v^N + U_v \Delta t^N \\ Y_v^{N+1} &= Y_v^N + V_v \Delta t^N \end{aligned} \right\} \quad (3.4a)$$

The vortex convection velocities  $U_v$  and  $V_v$  can be determined by three different methods: (1) a priori specification, (2) interpolation, and (3) the velocity field of a point vortex.

By far, the easiest method is to specify an initial position and then allow the vortex to convect at the free-stream speed. The equations most often used are

$$\left. \begin{aligned} U_v &= M_\infty \\ V_v &= 0 \end{aligned} \right\} \quad (3.4b)$$

Equations (3.4b) produce a “fixed-path” interaction. Although specifying the vortex is a trivial matter in a 2-D flow problem, it is the usual procedure in 3-D integral computations of advancing rotors because of the cost and complexity of finding the wake deformation. This method is also very useful for various comparison studies.

### 3.1. The Surface-Specification Methods

The surface-specification models are produced by modifying the airfoil surface boundary conditions based on an assumed vortex velocity field. This approach is basically the same as assuming that the vortex velocity may be superimposed on the general flow problem in the same way as a gust velocity would be modeled. The accuracy of this assumption depends on the location of the vortex with respect to the airfoil. If the vortex is far enough away, the field which it produces does resemble a gust field. A constant velocity field produces the angle-of-attack method, and a variable velocity field produces the lifting-surface method. Furthermore, if the vortex is far enough away from the airfoil, the signal arrives at the various points along the airfoil at approximately

the same time; such a solution would be a close approximation to the exact solution of the flow field. However, the effect of a finite signal propagation speed is still violated by these methods and this becomes increasingly important as the vortex nears the airfoil particularly for transonic flow conditions. The surface specification models are not capable of modeling the “time lag” between a signal arriving at a point on the airfoil surface near the airfoil and the signal arriving on the opposite side of the airfoil.

#### 3.1.1. Angle-of-Attack Method

The angle-of-attack method is the simplest possible model of the effect of a vortex on an airfoil. Equation (3.3) is used to compute the velocity at the airfoil quarter-chord. With this velocity, a vortex-induced angle of attack is computed. (See fig. 7.) The velocity perpendicular to the chord line is (if the leading edge is at  $x = 0$ )

$$V_\perp = V_\theta \cos \theta = \frac{\Gamma}{2\pi} \left( \frac{0.25 - X_v}{r^2 + a^2} \right) \quad (3.5)$$

The vortex-induced angle of attack is

$$\alpha_v = \tan^{-1} \frac{V_\perp}{U_\infty} \quad (3.6)$$

This angle is added to the airfoil angle of attack. The potential field is then computed as before. The angle of attack is updated at each time step as the vortex moves by the airfoil.

The airfoil is therefore assumed to be a point in space. In order for this solution to be valid, the vortex must be far enough away for this approximation to be accurate (e.g., the signal must arrive at every point on the airfoil simultaneously).

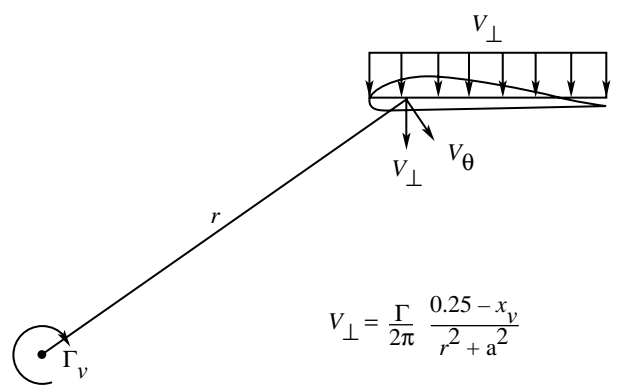


Figure 7. Angle-of-attack vortex model.

### 3.1.2. Lifting-Surface Method

The lifting-surface method is the most general form of the surface-specification models. As with the angle-of-attack method, equation (3.3) is used to compute the induced velocity at the airfoil surface. (See fig. 8.) However, unlike the angle-of-attack method, the velocity is allowed to vary over the surface. This provides a more physically accurate model of the effect. For the lifting-surface method, equation (3.5) is modified and is

$$V_{\perp} = V_{\theta} \cos \theta = \frac{\Gamma}{2\pi} \left[ \frac{(x/c) - X_v}{r^2 + a^2} \right] \quad (3.7)$$

With this change, the computation proceeds as in the angle-of-attack method.

The airfoil is therefore assumed to be a lifting surface. In order for this solution to be accurate, the signal must arrive at the upper and lower surface simultaneously.

## 3.2. Explicit Models

### 3.2.1. Branch-Cut Method

Caradonna (ref. 22) was the first to use an explicit method vortex model with a finite-difference rotor computation. The branch-cut method, which he used for steady 3-D flows, is based upon the known potential solution for a two-dimensional vortex (eq. (3.1)). This potential is implemented by means of a branch cut which extends from the center of the vortex to the aft face of the computational grid. (See fig. 9.) A jump in potential equal to  $\Gamma$  is imposed across the cut. Because equation (2.34) has already been implemented to account for the wake cut, no changes in the algorithm are required.

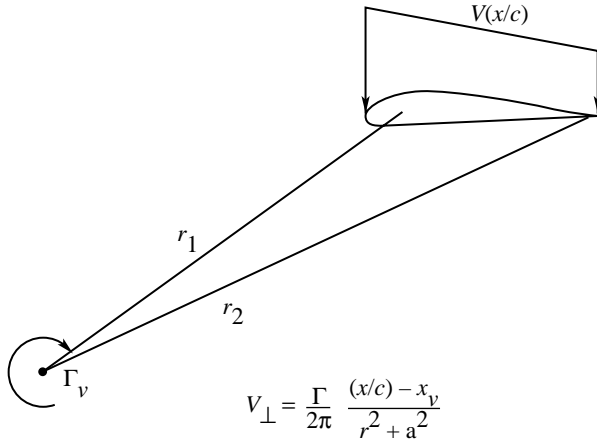


Figure 8. Lifting-surface vortex model.

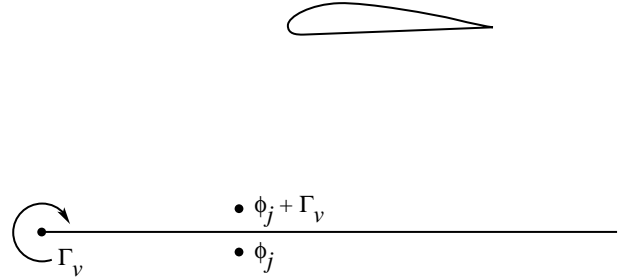


Figure 9. Branch-cut vortex model.

At first the branch-cut method seems to be well suited to a potential finite-difference algorithm. Difficulties arise, however, in unsteady problems whenever the vortex is moved. As the edge of the cut moves past a node, an abrupt change in the local potential occurs. This sharp change causes spurious waves which affect the entire flow field. The problem can be solved by spreading the edge of the branch cut, that is, by distributing vorticity on the various nodes which surround the vortex center. The simplest distribution involves the use of the nearest four grid points. The distribution is weighted so that the "center of gravity" of the vorticity represents the center of the vortex. With four grid points, this will uniquely determine the vorticity distribution. Increasing the number of points would require an arbitrary distribution to be imposed upon the vorticity. With this modification, the vortex may be moved from cell to cell smoothly and the spurious waves are reduced (not eliminated). The method of distributing the vorticity is illustrated in figure 10. The vertical distribution of vorticity is

$$\Gamma_1 = \Gamma_v \left( 1 - \frac{y_1 - y_v}{y^*} \right) \quad (3.8)$$

and

$$\Gamma_2 = \Gamma_v - \Gamma_1 \quad (3.9)$$

The horizontal distribution of vorticity is

$$\Gamma_4 = \Gamma_1 \frac{x_1 - x_v}{x^*} \quad (3.10)$$

and

$$\Gamma_3 = \Gamma_2 \frac{x_2 - x_v}{x^*} \quad (3.11)$$

The main vortex at  $(x_v, y_v)$  is then modeled with two branch cuts of varying strength; this can be called a two-cut model. The vortex may, in fact, be modeled by any arbitrary distribution. Stremel (ref. 23) uses a method in which the vortex is modeled with an area-weighted distribution of vorticity. A parabolic

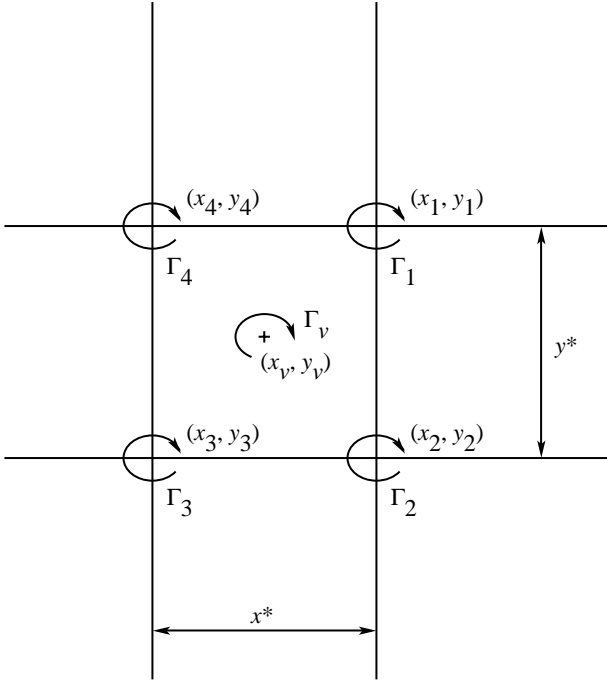


Figure 10. Distribution of vorticity to four points nearest vortex.

distribution of vorticity in the horizontal direction coupled with a linear vertical variation was used in reference 24. The effect of distributing the branch cuts is to create an artificial core for the vortex. The efficacy of the core is dependent upon the distribution of the nodes which are in the vicinity of the vortex. Because each of the separate branch cuts represents a separate subvortex and each subvortex has its own singular point, the core is very sensitive to the grid geometry.

Another problem associated with moving the vortex is concerned with computing the vortex convection velocity. Interpolation of the local velocities near the vortex is the only available means of computing the vortex velocity directly. The interpolation is complicated by the fact that the vortex creates such a large local disturbance; separating the effect of the flow field on the vortex from the effect of the vortex on the flow field is difficult. One major shortcoming of the branch-cut method is no good way exists to separate the effects because the branch cut contains the combined potential of the vortex, the free stream, and the airfoil. The vortex-induced velocities dominate the flow near the vortex and make an accurate interpolation very difficult. The velocity at the vortex may be approximated by using the velocity field of a point vortex in conjunction with the lift on the airfoil. In this approach, equation (3.3) is essentially used in "reverse" with  $\Gamma$  being the jump in potential

at the airfoil trailing edge (and hence a measure of the airfoil lift).

Another feature of the branch-cut method is the fact that it requires a difference equation (eq. (2.34)) to implement the effect of the vortex. That is, the vortex effect is specified entirely by the potential jump which is represented by the differencing across the branch cut. The accuracy of this difference is also dependent upon the local grid geometry. Therefore the accuracy of the vortex model changes as the vortex moves through the mesh. The distribution of the vorticity on the mesh further distorts the model by increasing the mesh dependence. A successful branch-cut model is therefore a compromise between an effective core model and an accurate vortex model.

### 3.2.2. Split-Potential Method

An alternative to the branch-cut method is the split-potential method. (See fig. 11.) In this approach, the velocity is assumed to be a combination of a known velocity and a perturbation velocity as follows:

$$\mathbf{q} = \nabla\phi + \mathbf{V}_G \quad (3.12)$$

where  $\mathbf{V}_G$  is the known velocity field solution and  $\nabla\phi$  is a perturbation velocity, which need not be small. The total potential for the blade-vortex problem can be split between the perturbation potential (associated with the airfoil) and the potential  $\mathbf{G}$ , which describes the vortex velocity field, as follows:

$$\Phi = \phi + \mathbf{G} \quad (3.13)$$

Any potential algorithm may be modified in this way to include the effects of a known velocity component and a perturbation velocity. Furthermore, the potential  $\mathbf{G}$  need not represent a vortex but can in fact represent any flow field which independently satisfies the potential equation. When equation (3.13)

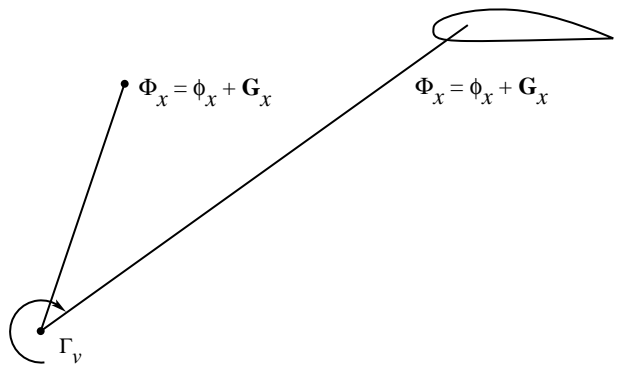


Figure 11. Split-potential vortex model.

is applied to equation (2.28), the following equation results (in the compact form similar to eq. (2.29)):

$$\begin{aligned}\mathbf{L}(\rho^N, \Delta\phi^{N+1}) &= \mathbf{R}^*(\rho^N, \phi^N + \mathbf{G}^N) \\ &\quad + \mathbf{C}^*(\rho^N, \rho^{N-1}, \phi^N, \phi^{N-1}, \phi^{N-2}, \beta^N, \beta^{N-1}) \\ &\quad + \mathbf{C}^*(\mathbf{G}^N, \mathbf{G}^{N-1}, \mathbf{G}^{N-2}, \beta^N, \beta^{N-1}) \\ &\quad + \Delta\phi^N + \Delta\mathbf{G}^N - \mathbf{L}(\rho^N, \Delta\mathbf{G}^{N+1})\end{aligned}\quad (3.14)$$

The Bernoulli equation undergoes a similar modification

$$\rho^N = \rho(\phi^N + \mathbf{G}^N) \quad (3.15)$$

The left-hand side of equation (3.14) is identical to the original algorithm (eq. (2.28)). The right-hand side contains additional spatial and temporal gradient terms in  $\mathbf{G}$ , including the update operator  $\mathbf{L}(\mathbf{G})$ .

Implementation of equation (3.14) has proven to be a challenge to several researchers who have sought to simplify the equation. (See refs. 7, 13, and 17.) The principal focus of these studies has been in eliminating the temporal gradient terms in  $\mathbf{G}$ . These terms pose a particular problem because they involve the potential  $\mathbf{G}$  explicitly. Computing these terms requires the tracking of a branch cut through the flow, in effect, the split-potential model is reduced to a branch-cut model. This will be particularly difficult for the complex geometry of the full 3-D problem. Furthermore, it is advantageous to minimize the computational requirements as much as possible. McCroskey and Goorjian (ref. 13) have shown (for a small disturbance formulation) that  $\mathbf{L}(\mathbf{G})$  and  $\Delta\mathbf{G}^N$  can be eliminated since the vortex potential (eq. (3.1)) is a solution to

$$\mathbf{L}\Delta\mathbf{G} = 0 \quad (3.16)$$

Therefore, a “small disturbance version” of equation (3.14) would be

$$\mathbf{L}(\rho^N, \Delta\phi^{N+1}) = \mathbf{R}^*(\rho^N, \phi^N + \mathbf{G}^N) + \Delta\phi^N \quad (3.17)$$

because  $\mathbf{C}^*$  terms are not present in a small disturbance form. Sankar and Malone (ref. 17) restricted the solution to his algorithm to a so-called “weak split-potential” approach in which the temporal gradient and most of the spatial terms in  $\mathbf{G}$  are simply dropped.

The present method is neither a small disturbance or weak split-potential form. In spite of this, the algorithm can be simplified by using a method proposed by Roger Strawn, Aeroflight dynamics Directorate, U.S. Army Aviation and Missile Command,

Ames Research Center. The first step is to recast equation (3.14) as

$$\begin{aligned}\mathbf{L}(\rho^N, \Delta\Phi^{N+1}) &= \mathbf{R}^*(\rho^N, \phi^N + \mathbf{G}^N) \\ &\quad + \mathbf{C}^*(\rho^N, \rho^{N-1}, \phi^N, \phi^{N-1}, \phi^{N-2}, \beta^N, \beta^{N-1}) \\ &\quad + \mathbf{C}^*(\mathbf{G}^N, \mathbf{G}^{N-1}, \mathbf{G}^{N-2}, \beta^N, \beta^{N-1}) \\ &\quad + \Delta\phi^N + \Delta\mathbf{G}^N\end{aligned}\quad (3.18)$$

The update operators  $\mathbf{L}$  have been recombined to include the total potential. The temporal conservation correction term  $\mathbf{C}^*$  in  $\mathbf{G}$  has been retained, since there is no way to effectively separate the  $\mathbf{G}$  and  $\phi$  parts of the density. The effect of these terms on the solution is discussed in section 4. Solution of equation (3.18) is achieved as before with equations (2.60), (2.61), and (2.62), which produces  $\Phi^{N+1}$ . A final step is added to obtain  $\phi$

$$\phi^{N+1} = \Phi^{N+1} - \Delta\mathbf{G}^{N+1} \quad (3.19)$$

In implementing these equations, the velocity due to the vortex is computed by equation (3.3). The velocity components are

$$\mathbf{G}_x = -\frac{\Gamma}{2\pi} \left( \frac{y - y_v}{\mathbf{r}^2 + a^2} \right) \quad (3.20)$$

and

$$\mathbf{G}_y = \frac{\Gamma}{2\pi} \left( \frac{x - x_v}{\mathbf{r}^2 + a^2} \right) \quad (3.21)$$

These equations are transformed into  $\mathbf{G}_\xi$  and  $\mathbf{G}_\eta$  by

$$\mathbf{G}_\xi = \mathbf{G}_x x_\xi + \mathbf{G}_y y_\xi \quad (3.22)$$

and

$$\mathbf{G}_\eta = \mathbf{G}_x x_\eta + \mathbf{G}_y y_\eta \quad (3.23)$$

The time derivative terms are obtained with the chain rule as

$$\mathbf{G}_\tau = \mathbf{G}_\xi \xi_\tau + \mathbf{G}_\eta \eta_\tau + \mathbf{G}_t t_\tau \quad (3.24)$$

This value may be determined most easily in an axis system fixed to the vortex. In this system, the vortex is fixed and the airfoil, to which the grid is attached, moves past it. In this system

$$\left. \begin{aligned}\mathbf{G}_t &= 0 \\ \eta_\tau &= -V_v \\ \xi_\tau &= -U_v\end{aligned} \right\} \quad (3.25)$$

therefore,

$$\Delta\mathbf{G} = \Delta t^N \mathbf{G}_\tau \quad (3.26)$$

Use of equation (3.26) eliminates the need to compute  $\mathbf{G}$  explicitly and hence the need to track a branch cut. Equations (3.20) through (3.26) are used to implement the split-potential method in the present algorithm.

## 4. Computational Results

The presentation of computed results is divided into four sections. Section 4.2 reports results obtained for simple flows (with no vortex interaction) in order to establish the validity of the basic algorithm. Section 4.3 is an introduction to the results obtained in a HSI computation. The major features of the interaction are presented for a typical case. The graphical presentation of data which describes the interaction is presented and explained. The sensitivity of the algorithm to both time step and random disturbances is discussed. Section 4.4 presents a comparison of the results obtained with the four vortex models. Comparisons with experimental data are also made. Section 4.5 presents a parametric study of the effects of some key parameters such as Mach number, vortex strength, miss distance, vortex core size, and angle of attack.

### 4.1. Executing the Algorithm

#### 4.1.1. Executing Basic Airfoil Solution

A basic airfoil solution consists of the steady flow around an airfoil at a fixed angle of attack. The steady-state version of the algorithm (eq. (2.59)) is used to generate this solution. Figure 12 depicts the maximum residual convergence history for an NACA 0012 airfoil at  $\alpha = 0^\circ$  and several Mach numbers. The residual is reduced by oscillating the pseudo time  $\Delta t$  between the values 0.001 and 5 for the first 20 iteration steps. This oscillation drops the value of  $\mathbf{R}_{\max}$  approximately 1 order of magnitude. The pseudo time is then fixed at  $\Delta t = 0.001$  to minimize shock oscillation problems for the higher Mach numbers. Fixing  $\Delta t$  results in the unusual flattening of the curve at about 100 time steps. After this point,  $\Delta t = 0.001$  is not the optimum choice to reduce  $\mathbf{R}$ . However, the current scheme provides a suitable method for reducing  $\mathbf{R}$  to an acceptable value over the widest range of flow conditions.

#### 4.1.2. Executing HSI Problem

The solution of a blade-vortex interaction problem proceeds in two steps. The first step is the computation of a steady-state solution. The steady-state

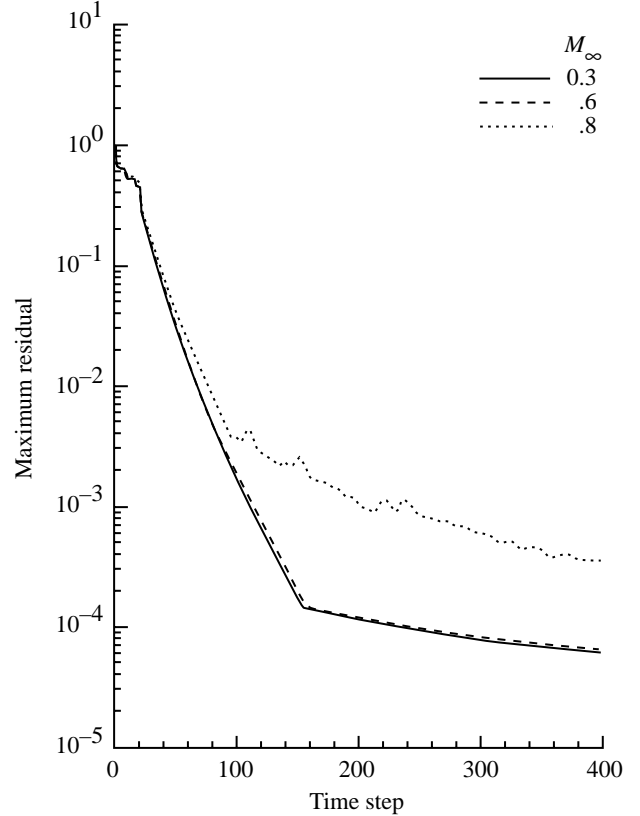


Figure 12. Maximum residual convergence history for NACA 0012 airfoil at several Mach numbers and  $\alpha = 0^\circ$ .

solution may be produced with or without the presence of the vortex; however, for convenience the vortex is included. The vortex is initially fixed at some distance upstream (usually about 10 chords) and the steady flow about the airfoil is computed. After the steady-state solution is obtained, the vortex is allowed to move along a path determined by equations (3.4a). A specified path is produced by using equations (3.4b) to compute vortex velocities. As the vortex moves through the computational grid, the time step is varied by using the following relationship which was established by numerical experimentation:

$$\Delta t = \left\{ \frac{0.5 \cos[\pi(x_v + 10.405)]}{10.405} + 0.522 \right\} / M_\infty \quad (4.1)$$

Equation (4.1) is designed to provide a sufficient number of steps within each grid cell to assure proper resolution of the vortex. Thus, when the vortex is far from the airfoil,  $\Delta t$  is large to minimize the number of steps required for the solution; and when it is near the airfoil,  $\Delta t$  is small to enhance accuracy. Application of a varying time step reduces the time requirements

for computation by as much as a factor of 6 over a constant time step.

#### 4.1.3. Data Recovery

The velocities in the flow field are computed by the central difference equations (2.33) and (2.34). In the physical frame they become

$$\left. \begin{aligned} u &= \Phi_\xi \xi_x + \Phi_\eta \eta_x \\ v &= \Phi_\xi \xi_y + \Phi_\eta \eta_y \end{aligned} \right\} \quad (4.2)$$

Pressure is calculated by using the isentropic flow relations which lead to

$$c_p = \frac{\tilde{p}_\infty}{(1/2)\tilde{\rho}\tilde{U}_\infty^2} (\rho^\gamma - 1) \quad (4.3)$$

Lift on the airfoil is calculated by using the trapezoid rule to integrate the pressures to get

$$c_l = 2 \int_0^1 \zeta \Delta c_p d\zeta \quad (4.4)$$

where  $\zeta = \sqrt{x/c}$ . The integration with respect to the square root of the surface coordinate increases the accuracy in the leading-edge region. The Mach number is

$$M_l^2 = \frac{u^2 + v^2}{a_\infty^2} \quad (4.5)$$

The density is computed directly from the Bernoulli equation (eq. (2.2))

$$\tilde{\rho} = \rho_\infty \left[ 1 + \frac{\gamma - 1}{2} \left( M_\infty^2 - 2\Phi_t - \Phi_x^2 - \Phi_y^2 \right) \right]^{1/(\gamma-1)}$$

## 4.2. Results From Basic Airfoil Solution

Before presenting the results for the HSI problem, it is useful to demonstrate the validity of the basic algorithm by comparisons with the results obtained by other researchers and by experiment for steady and unsteady flow problems.

### 4.2.1. Comparison With Original Algorithm

The basic scheme used in the present method is an extension of a method developed by Steger and Caradonna (ref. 2). The first step in verifying the present method is to demonstrate the ability to reproduce their results. The predicted midchord values of  $c_p$  of a parabolic arc airfoil as it thickens then thins for a free-stream Mach number of 0.85

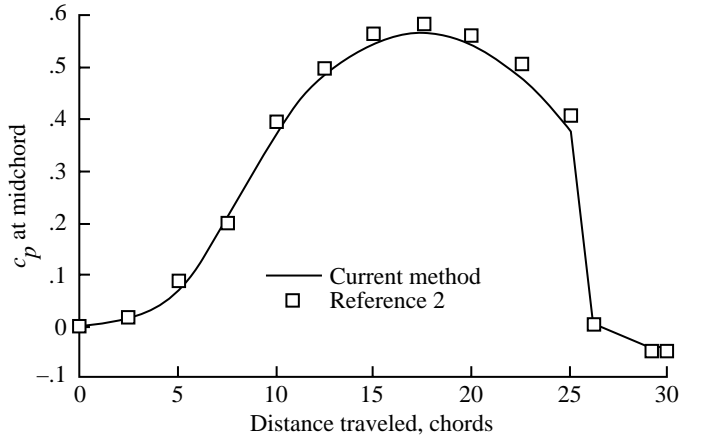


Figure 13. Pressure coefficients at midchord for parabolic arc airfoil as it thickens then thins for  $M_\infty = 0.85$  and  $\tau = 0.104$ . Small disturbance grid used.

and maximum thickness  $\tau$  of 0.104 are presented in figure 13. The results for the present method were predicted by using a “small-disturbance” type mesh (see step 1 in section 2.2); reference 2 also uses such a mesh. Figure 13 demonstrates very close agreement between the present method and reference 2.

### 4.2.2. Subcritical Flow

Although HSI is, in general, a transonic flow problem, the demonstrated ability to compute subcritical flows is necessary to establish confidence in the algorithm. Figure 14 presents computed results for an NACA 0012 airfoil at  $M_\infty = 0.63$  and  $\alpha = 2^\circ$  along with the results of Holst (ref. 25).

Figure 15 presents calculated results (performed by Michel Costes of the Office National d’Etudes et de Recherches Aerospatiale (ONERA), who had been provided with the present code) for an Aerospatiale RA16SC1 airfoil at  $M_\infty = 0.30$  and  $\alpha = 0^\circ$ . The results are compared with experimental data generated by ONERA and provided for this comparison. Both comparisons demonstrate the ability of the present algorithm to predict accurately the subcritical flow about an airfoil. The correlation with the Aerospatiale RA16SC1 airfoil is particularly good considering the large difference between the surface grid line (obtained from the Joukowski airfoil) used to represent the airfoil surface and the actual airfoil surface.

### 4.2.3. Supercritical Case

A demonstrated ability to compute supercritical flow is necessary in order to proceed with the HSI problem. Figure 16 presents computed results for

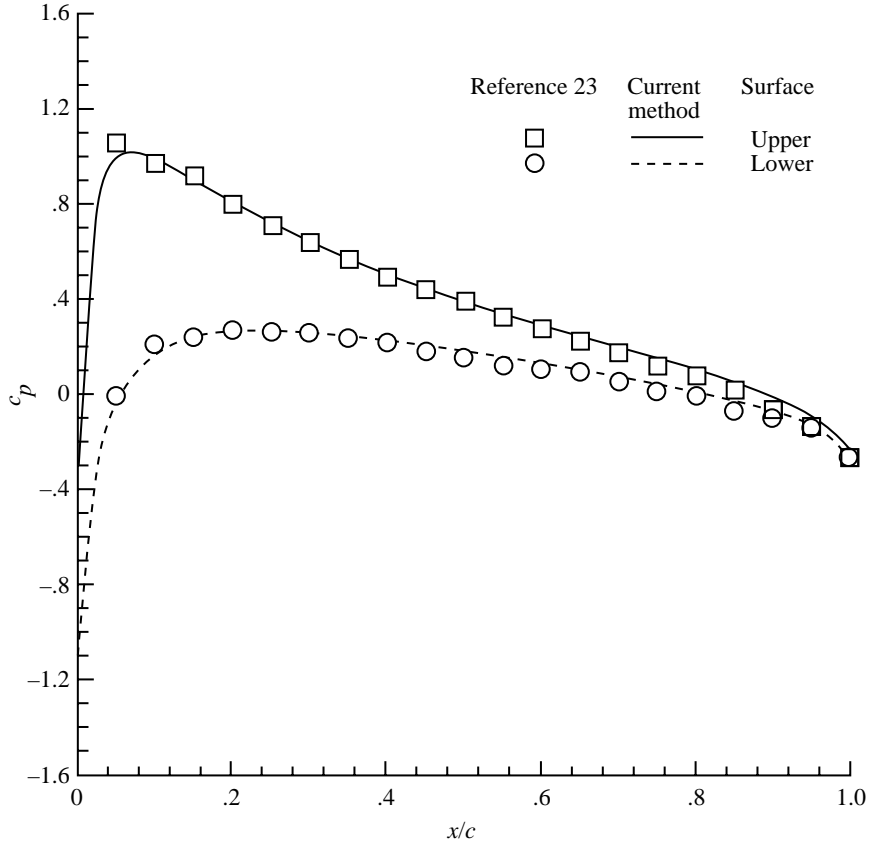


Figure 14. Pressure coefficients for NACA 0012 airfoil at  $M_\infty = 0.63$  and  $\alpha = 2^\circ$ .

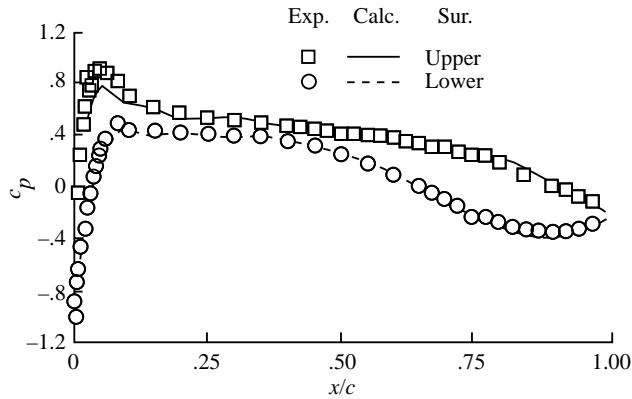


Figure 15. Pressure coefficients for Aerospatiale RA16SC1 airfoil at  $M_\infty = 0.30$  and  $\alpha = 0^\circ$ . Data from Michel Costes, ONERA.

an NACA 0012 airfoil at  $M_\infty = 0.8$  and  $\alpha = 0^\circ$ . The surface pressures are compared with results generated by Bridgeman, Steger, and Caradonna (ref. 10), which were provided by him for this comparison. Close examination of the figure reveals a

slight difference in shock location between the two models. This difference is probably caused by the difference in grid metric computation. The Bridgeman method uses the free-stream subtraction method to remove the metric truncation error and the present method uses consistent metric differencing.

Figure 17 presents calculated results for an Aerospatiale RA16SC1 airfoil at  $M_\infty = 0.76$  and  $\alpha = 0^\circ$  (provided by Costes). The results are compared with experimental data generated by ONERA. The correlation is good, except for a slight difference in shock location which is probably due to viscous effects on the real airfoil.

#### 4.2.4. Oscillating Airfoil

The ability to predict unsteady flows is necessary in order to proceed with the HSI problem. Figure 18 presents calculated results for an NACA 0012 airfoil at  $M_\infty = 0.755$  and  $\alpha = 0^\circ$  and experimental results from Goorjian and Guruswamy (ref. 26). Comparison of the two results shows excellent agreement. Figure 19 presents the results for an oscillating NACA 0012 airfoil. Figure 18 is the steady

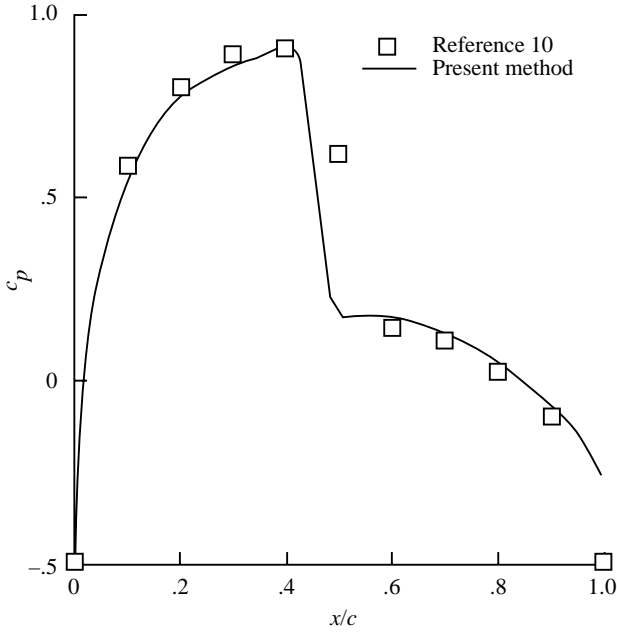


Figure 16. Pressure coefficients for NACA 0012 airfoil at  $M_\infty = 0.80$  and  $\alpha = 0^\circ$ .

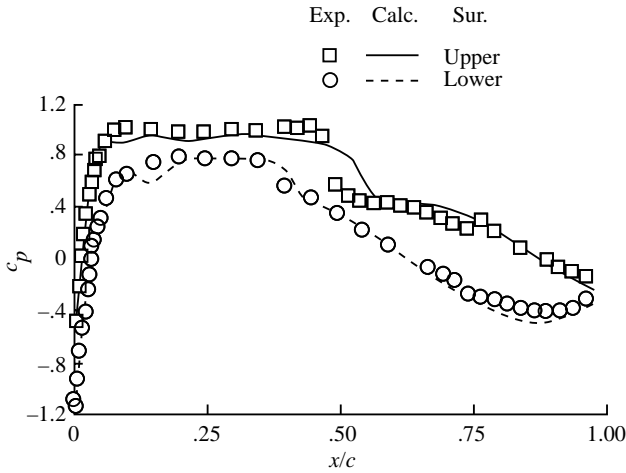


Figure 17. Pressure coefficients for Aerospatiale RA16SC1 airfoil at  $M_\infty = 0.76$  and  $\alpha = 0^\circ$ .

starting point. The airfoil is oscillating at a reduced frequency of  $k = \omega c/U_\infty = 0.1628$  about  $\alpha = 0^\circ$  with  $\alpha_{\max} = \pm 2.51$ . The predicted pressures are slightly different from the measured values because of the difficulty in exactly matching the test points. These results indicate that the algorithm can predict unsteady transonic flow.

Figure 20 presents calculated results for an Aerospatiale RA16SC1 airfoil with an oscillating 25-percent flap at  $M_\infty = 0.30$  and  $\alpha = 0^\circ$ . The results are compared with experimental data for three

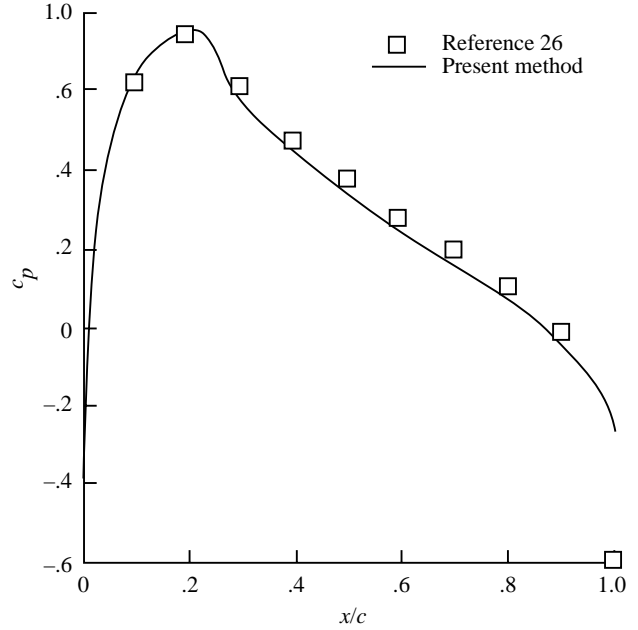


Figure 18. Pressure coefficients for NACA 0012 airfoil at  $M_\infty = 0.755$  and  $\alpha = 0^\circ$ .

periods of motion. The pressures are presented in a format based on the following equation:

$$c_p = (c_p)_0 + \sum_k (c_p)_k e^{ik\omega t + \varphi} \quad (4.6)$$

where  $(c_p)_0$  is the steady pressure and  $\varphi$  is the phase angle of the oscillation. The correlation is good except for the flap pressures themselves. However, the grid is sparse in this region and the difference could easily be due to poor resolution.

### 4.3. Introduction to HSI

#### 4.3.1. Generic Vortex Interaction

Before presenting the vortex model comparison, a discussion of the basic features of the blade-vortex interaction will be useful. Figure 21 is a representative plot of lift coefficient versus vortex location for an NACA 0012 airfoil at  $\alpha = 0^\circ$  and  $M_\infty = 0.60$ , and a vortex with an equivalent lift of  $c_{l,v} = 0.400$ , and a vertical miss distance of 0.251 chord moving along a fixed path at constant speed. The computation uses the split-potential method to model the vortex. The several points of interest which occur during the interaction are labeled in the figure. Point 1 is the initial condition of the airfoil in relatively undistorted flow (the vortex is far upstream). The sign of the vortex is such that it generates a downwash on the

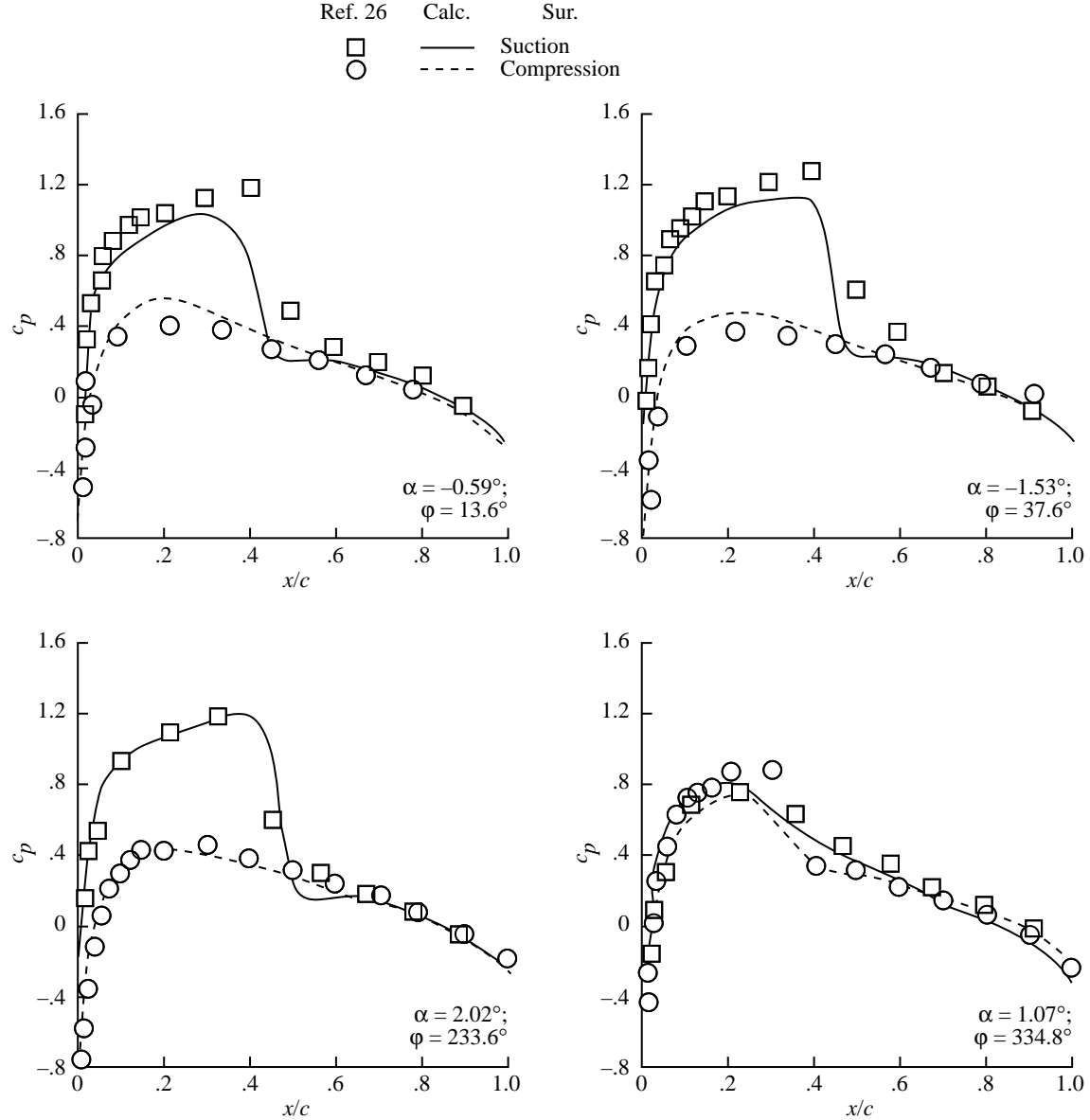


Figure 19. Pressure coefficients for oscillating NACA 0012 airfoil at  $M_{\infty} = 0.755$ .

airfoil, which has the same effect as reducing the angle of attack. When the vortex approaches, the pressure on the lower side of the airfoil diminishes and drives the lift coefficient to increasingly negative values. This region is labeled 2 in the figure and is called the approach phase of the interaction. As the vortex approaches the leading edge of the airfoil, the lift rapidly diminishes to a minimum point, labeled 3. As the vortex passes under the airfoil the velocities induced by it become an upwash on a larger and larger portion of the airfoil. While the vortex is passing under the airfoil, the pressures change rapidly and the lift rebounds to positive values, labeled 4; this is

the interaction phase. As the vortex approaches the trailing edge, the lift begins to level out, labeled 5 in the curve; this is called the recovery phase. After the vortex passes the trailing edge of the airfoil, the lift levels out and remains relatively constant as the vortex moves away. This region is labeled 6 in the figure and is called the departure phase. An interesting phenomenon occurs during the departure phase. The lift is found to rebound to a level which is higher than the initial condition and to return to the initial condition only after a considerable time. This behavior has been seen in most (if not all) other BVI computational results reported in the literature

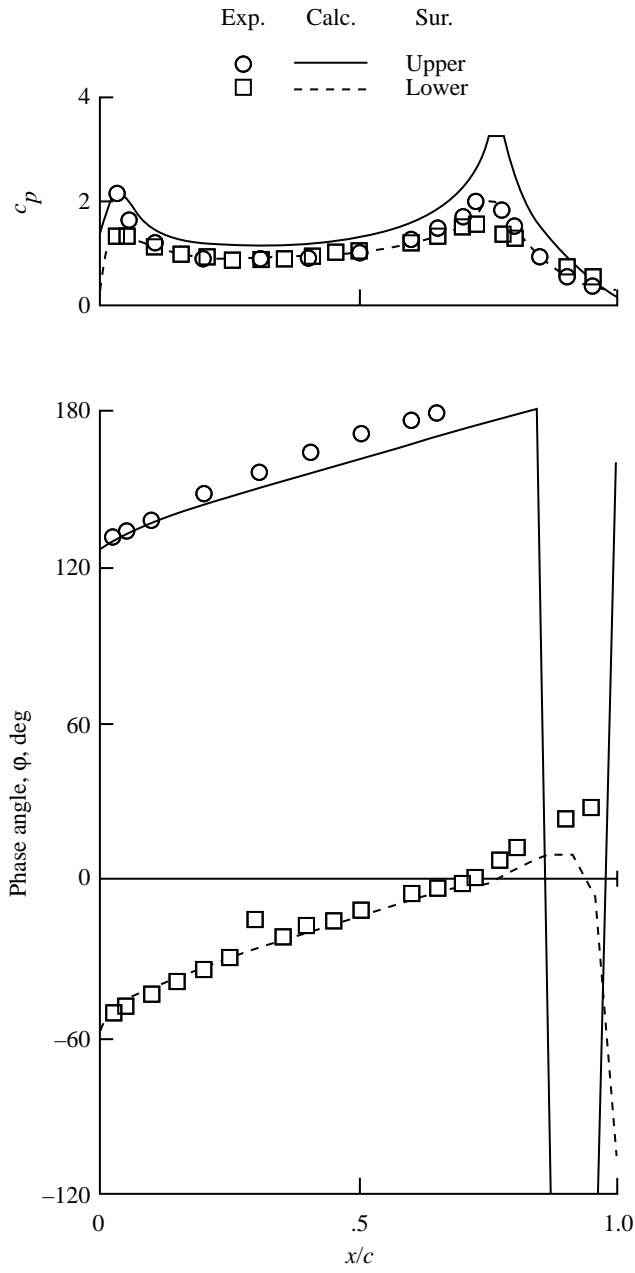


Figure 20. Pressure coefficients for Aerospaciale RA16SC1 airfoil with oscillating 25-percent flap.  $M_\infty = 0.30$ ;  $\alpha = 0^\circ$ .

but has not been explained yet. This decay effect may be explained by recalling that the HSI problem is a limiting case of an infinite line vortex interacting with an infinite aspect ratio wing. As the vortex passes under the wing, it generates waves all along it. These signals cannot arrive simultaneously at any point. Therefore a “delay” effect is caused by the time lag in the arrival of waves from the rest of the wing. This “lag” could account for the delay in lift recovery. This response characteristic is familiar in

the field of acoustics but is unusual in aerodynamic problems.

Figure 22 is a composite of the airfoil lift history and surface pressures at selected points during the interaction. The airfoil lift history is presented in the upper left-hand plot and the surface pressure coefficients are presented at points 1 through 5 in the other plots. These plots show that the presence of the vortex affects the airfoil primarily through changes in the lower surface pressure. The passage of the vortex is seen in the distortion of the lower surface pressure near the vortex location. (See plots for 2, 3, and 4.) The plot for 4 shows a slight breakdown in the Kutta condition when the vortex is just past the airfoil trailing edge; this is shown later to be an effect of the time step.

Figure 23 shows the time history of the lower surface pressures during BVI. Pressure coefficients as a function of time are presented at 10 locations on the airfoil. The points 2, 3, and 4, placed here for reference, correspond to the pressure plots in figure 22. From this figure, it can be seen that the primary effect is in the leading-edge pressure with a secondary effect propagating with the location of the vortex. The format used in figures 21, 22, and 23 is used in the rest of this report.

#### 4.3.2. Effects of Time Terms

Because of the time linearization, testing the algorithm for sensitivity to the size of the time step is necessary. Recall that the time step is varied with vortex location (eq. (4.1)); this variation tends to increase the error when the vortex is far from the airfoil. Figure 24(a) shows the effect on airfoil lift history of reducing  $\Delta t$  by a factor of 2 from the values computed by equation (4.1). The figure shows the interaction of an NACA 0012 airfoil with a vortex of strength  $c_{l,v} = 0.496$ , a miss distance of  $-0.433$  chord, and a free-stream Mach number of 0.536 (i.e., the same condition as the sample case). Figure 24(b) shows the interaction of an NACA 0012 airfoil with a vortex of strength  $c_{l,v} = 0.40$ , a miss distance of  $-0.251$ , and a free-stream Mach number of 0.80. The split-potential method was used to make these computations. Further reduction has no effect on the solution. The primary effect of reduced  $\Delta t$  is to improve the pressure coefficient prediction when the vortex is near the trailing edge (recall plot for 3 in fig. 22); that is, the lower time step maintains a more accurate Kutta condition. This effect is a relatively minor one. Equation (4.1) was used for the following comparisons. Since the purpose of these runs was to compare vortex models and explore parametric

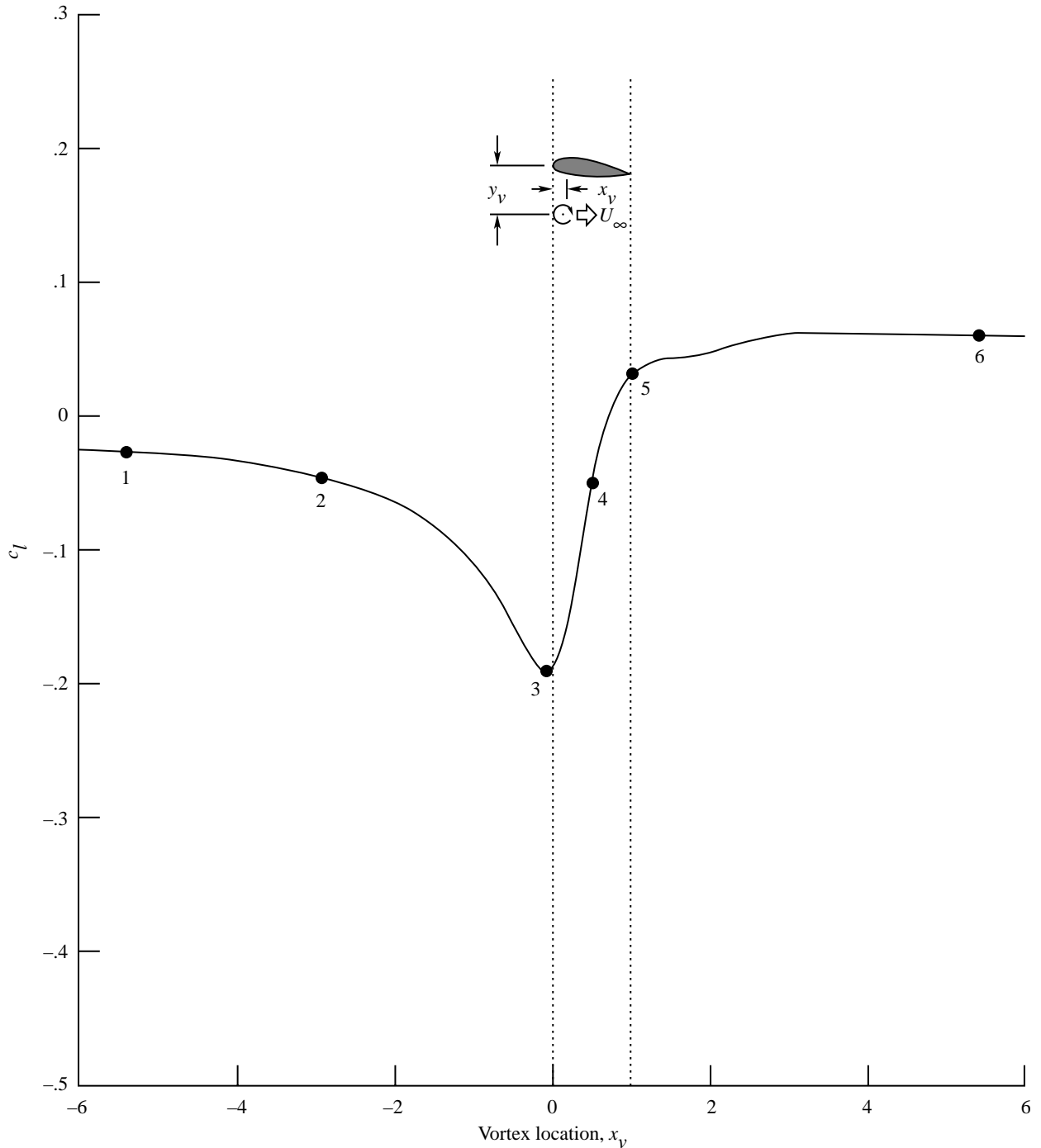


Figure 21. Variation of airfoil lift with vortex location for typical BVI.  $a = 0.05$ ;  $\alpha = 0^\circ$ ;  $M_\infty = 0.60$ ;  $y_v = -0.251$ ;  $c_{l,v} = 0.400$ ; NACA 0012 airfoil; fixed path.

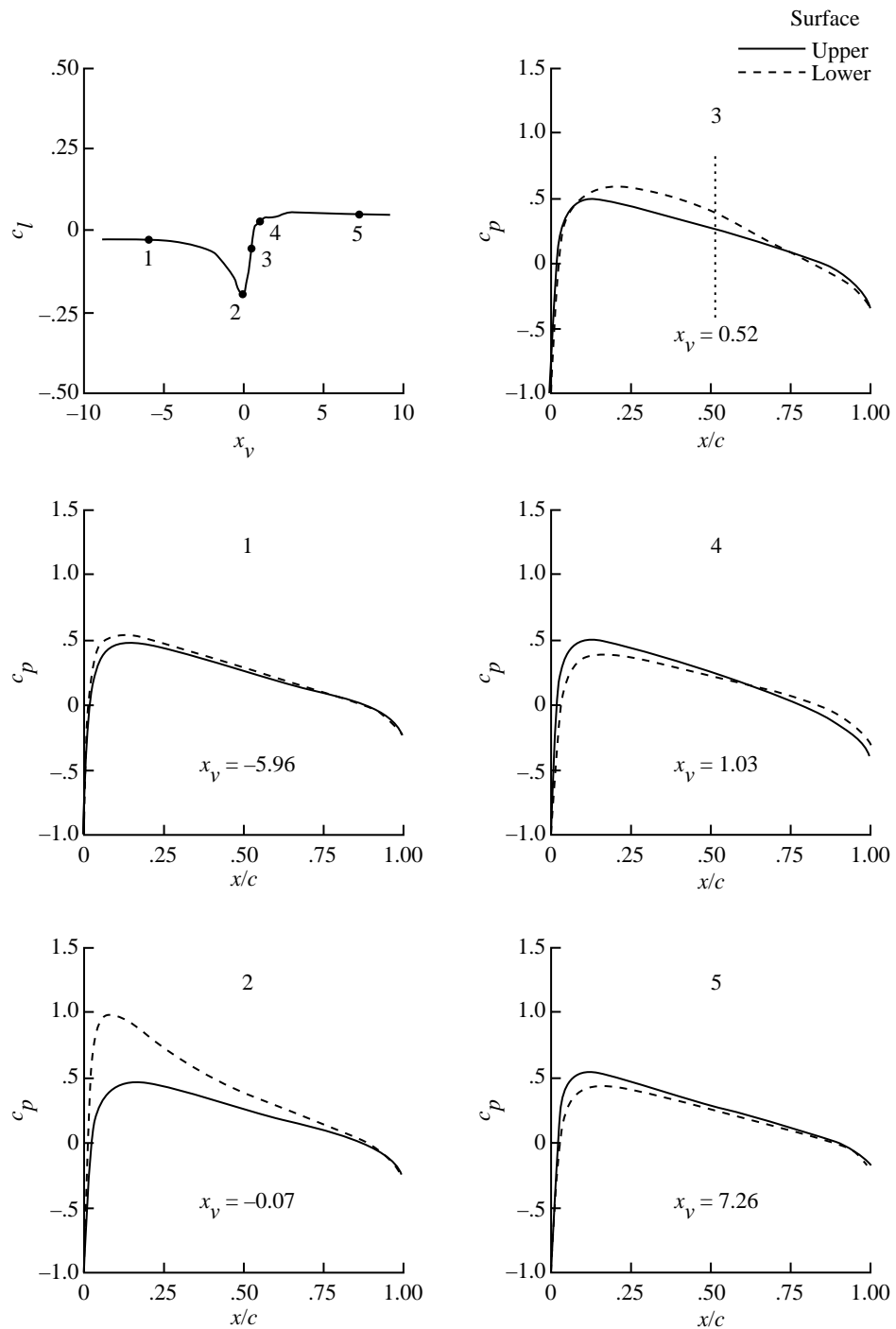


Figure 22. Airfoil surface pressure distribution for typical BVI.

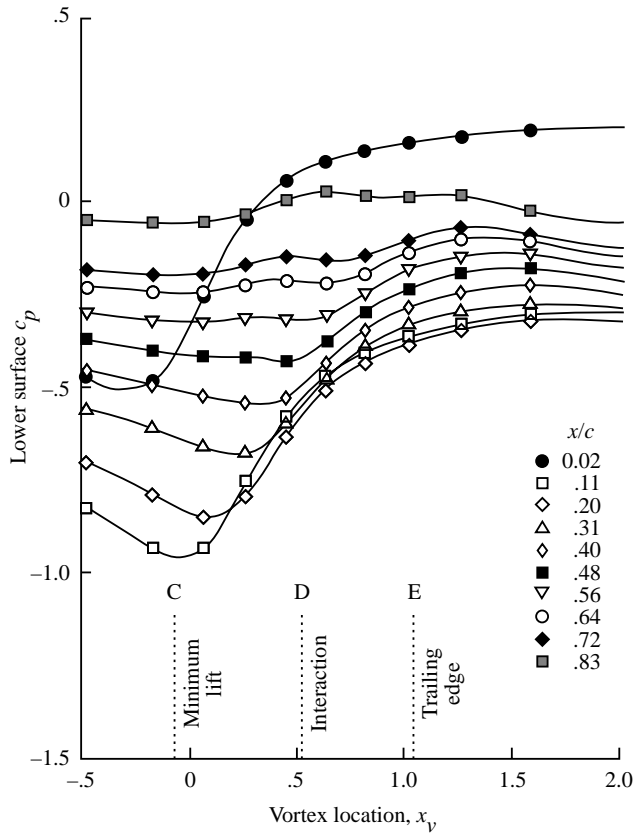
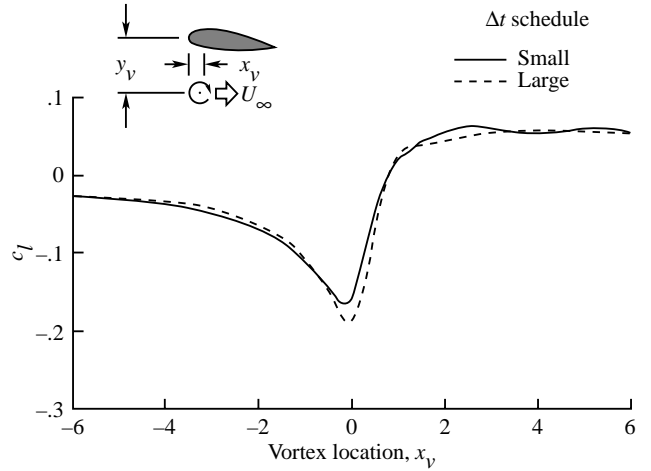


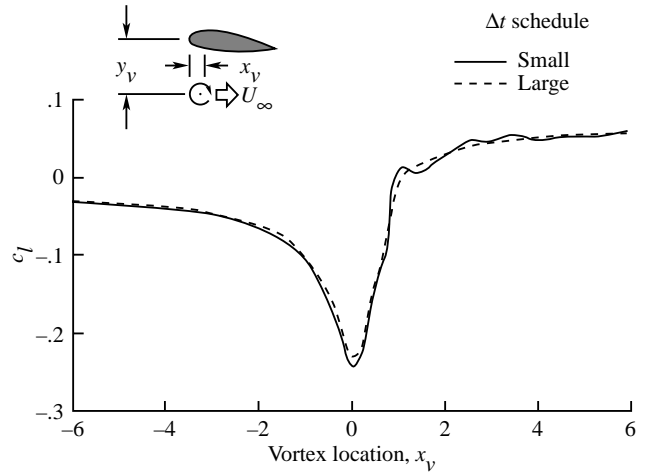
Figure 23. Variation of lower surface pressure coefficient with vortex location for typical BVI.

effects, use of the larger time step makes little difference.

However the reduced time step computations do indicate the presence of “waves” superimposed on the basic solution especially for the departure phase of the high-speed case. These waves are generated as the vortex moves past nodes in the grid causing an abrupt change in local velocity. The wave appears to behave exactly as an ordinary acoustic wave and is propagated with a Doppler effect. That is, a low-speed disturbance travels with equal strength upstream and downstream; a high-speed disturbance travels with increased strength upstream. Figure 25(a) is a plot of pressure at a fixed point in space as the vortex passes at low speed; figure 25(b), at high speed. The high-speed disturbance is seen to occur after the vortex has passed the low-speed disturbance, before and after the vortex has passed. Reducing the time step in figure 24 more accurately captures this effect. These waves are seen to be minor disturbances on the basic solution and do not affect the comparisons.



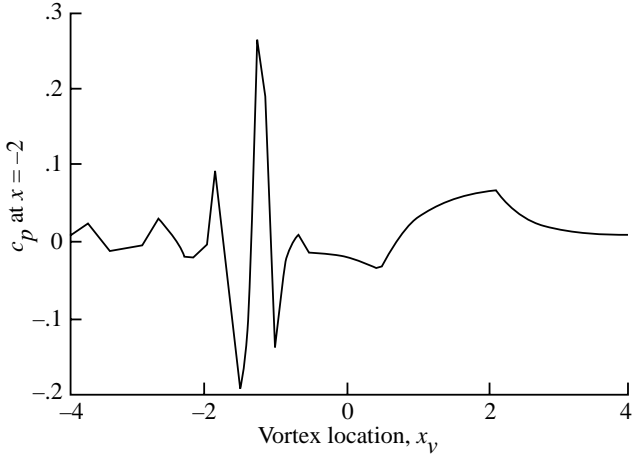
(a) Subcritical flow;  $a = 0.15$ ;  $\alpha = 0^\circ$ ;  $M_\infty = 0.536$ ;  $y_v = -0.433$ ;  $c_{l,v} = 0.496$ ; NACA 0012 airfoil; fixed path.



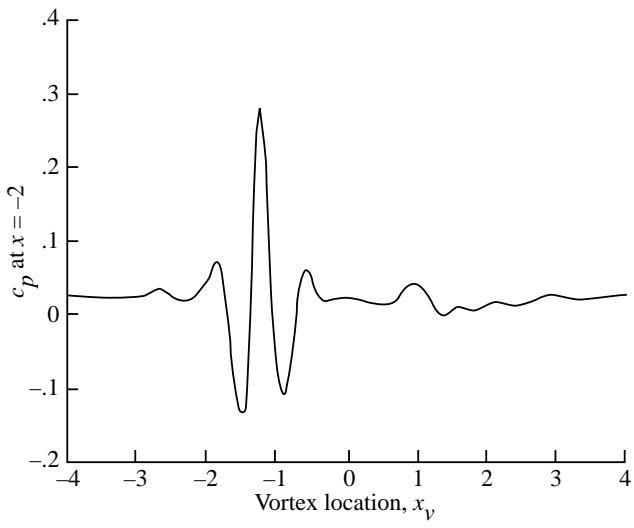
(b) Supercritical flow;  $a = 0.05$ ;  $\alpha = 0^\circ$ ;  $M_\infty = 0.80$ ;  $y_v = -0.251$ ;  $c_{l,v} = 0.40$ ; NACA 0012 airfoil; fixed path.

Figure 24. Effect of time step on airfoil lift during BVI.

One of the key unanswered questions associated with the use of the split-potential model is the effect on the solution of temporal difference terms in  $\mathbf{G}$ , ( $\mathbf{C}^*$ ,  $\mathbf{L}$ ,  $\Delta \mathbf{G}$ ). (See eq. (3.14).) These terms can have a serious impact on a 3-D computation because of the geometric complexity of the wake and the difficulty of computing  $\mathbf{G}_t$  for each wake element. Figure 26(a) shows the effects of the  $\mathbf{G}_t$  terms on the integrated lift curve for a subcritical flow condition. From the figure, little difference is seen between the two curves. However, this flow condition is for low speed and the vortex is not very close to the airfoil (a so-called weak interaction). Figure 26(b) shows a similar comparison for a close supercritical interaction



(a)  $M_\infty = 0.30$ .

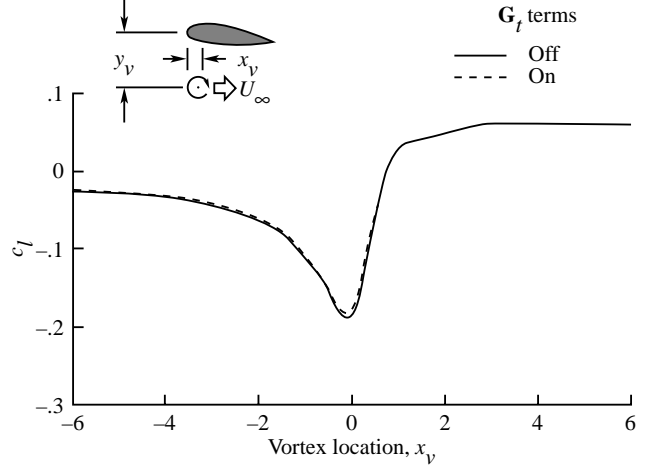


(b)  $M_\infty = 0.80$ .

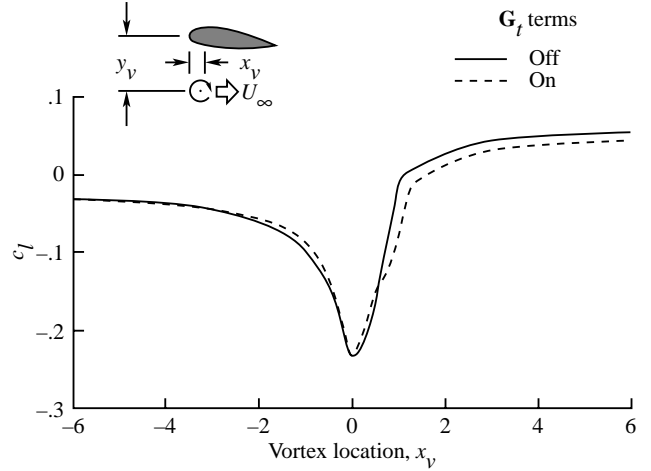
Figure 25. Effect of error wave propagation during BVI.

(a “strong” interaction). Here the effect of the terms is much more apparent. In particular, the  $\mathbf{G}_t$  terms show a marked effect during the interaction phase and the departure phase. Notice especially the region in which the slope of the curve undergoes a rapid change. This region corresponds to the vortex passing through the airfoil shock. The combination of these velocities (shock and vortex) causes high pressures on the airfoil surface, which are reflected in the loading curve.

In summary, the  $\mathbf{G}_t$  terms seem to have little effect on the solution except for the strong interaction cases. For the parametric studies, these terms are dropped from any further computations involving the split-potential method in order to minimize run time and costs.



(a) Subcritical flow;  $a = 0.15$ ;  $\alpha = 0^\circ$ ;  $M_\infty = 0.536$ ;  $y_v = -0.433$ ;  $c_{l,v} = 0.496$ ; NACA 0012 airfoil; fixed path.

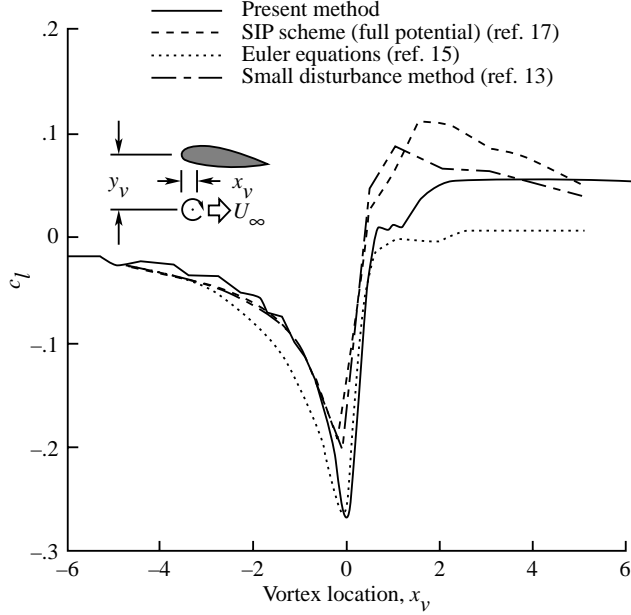


(b) Supercritical flow;  $a = 0.05$ ;  $\alpha = 0^\circ$ ;  $M_\infty = 0.80$ ;  $y_v = -0.25$ ;  $c_{l,v} = 0.40$ ; NACA 0012 airfoil; fixed path.

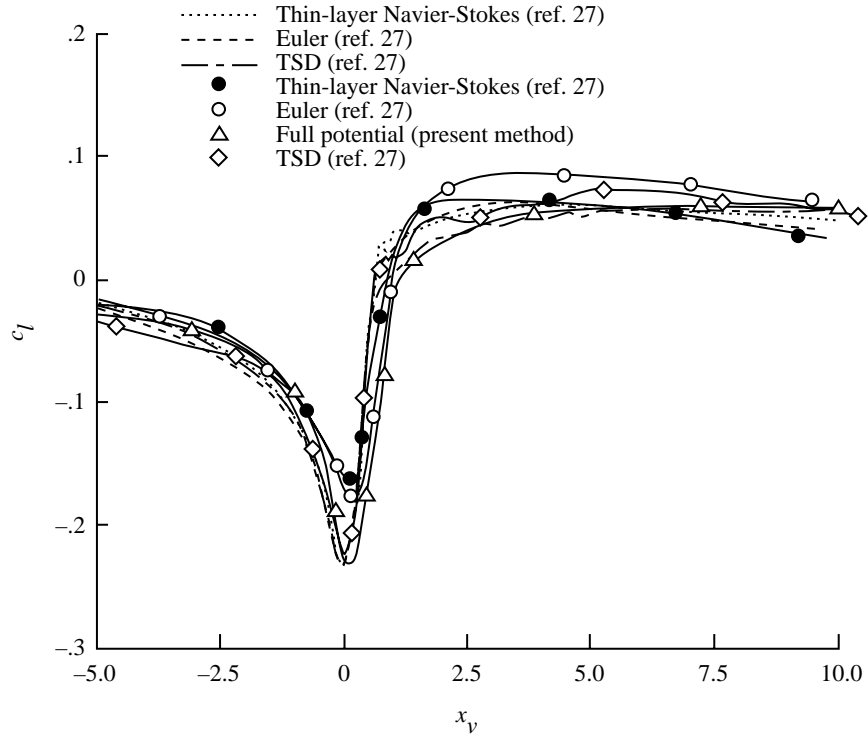
Figure 26. Effect of  $\mathbf{G}_t$  terms on split-potential model.

#### 4.3.3. Comparison With Other Codes

Figure 27(a) shows the airfoil lift history from the split-potential results and related computations of several other researchers (refs. 13, 15, and 17). The various other methods shown range from small disturbance algorithms to Euler methods. The interaction depicted is for an NACA 0012 airfoil at  $M_\infty = 0.30$  and  $\alpha = 0^\circ$  and for an equivalent lift of the vortex  $c_{l,v} = 0.40$ . The present method compares well with the results from the Euler equations (ref. 15), which has a more complete physical modeling, especially in prediction of minimum lift. Both the small disturbance (ref. 13) and the strongly implicit scheme (ref. 17) predict similar results.



(a) Subcritical flow;  $a = 0.05$ ;  $\alpha = 0^\circ$ ;  $M_\infty = -0.30$ ;  $y_v = -0.251$ ;  $c_{l,v} = 0.40$ ; NACA 0012 airfoil; fixed path.



(b) Supercritical flow.  $M_\infty = 0.80$ .

Figure 27. Airfoil lift variation with vortex location for various algorithms.

Figure 27(b) shows a similar comparison for the NACA 0012 airfoil at  $M = 0.80$  and  $\alpha = 0^\circ$ ,  $c_{l,v} = 0.40$ , and a vertical miss distance  $y_v$  of  $-0.25$ . These results were taken from a survey paper

by Srinivasan and McCroskey (ref. 27). Figure 27 demonstrates that the present method produces results for the integrated lift history comparable with those generated by other researchers.

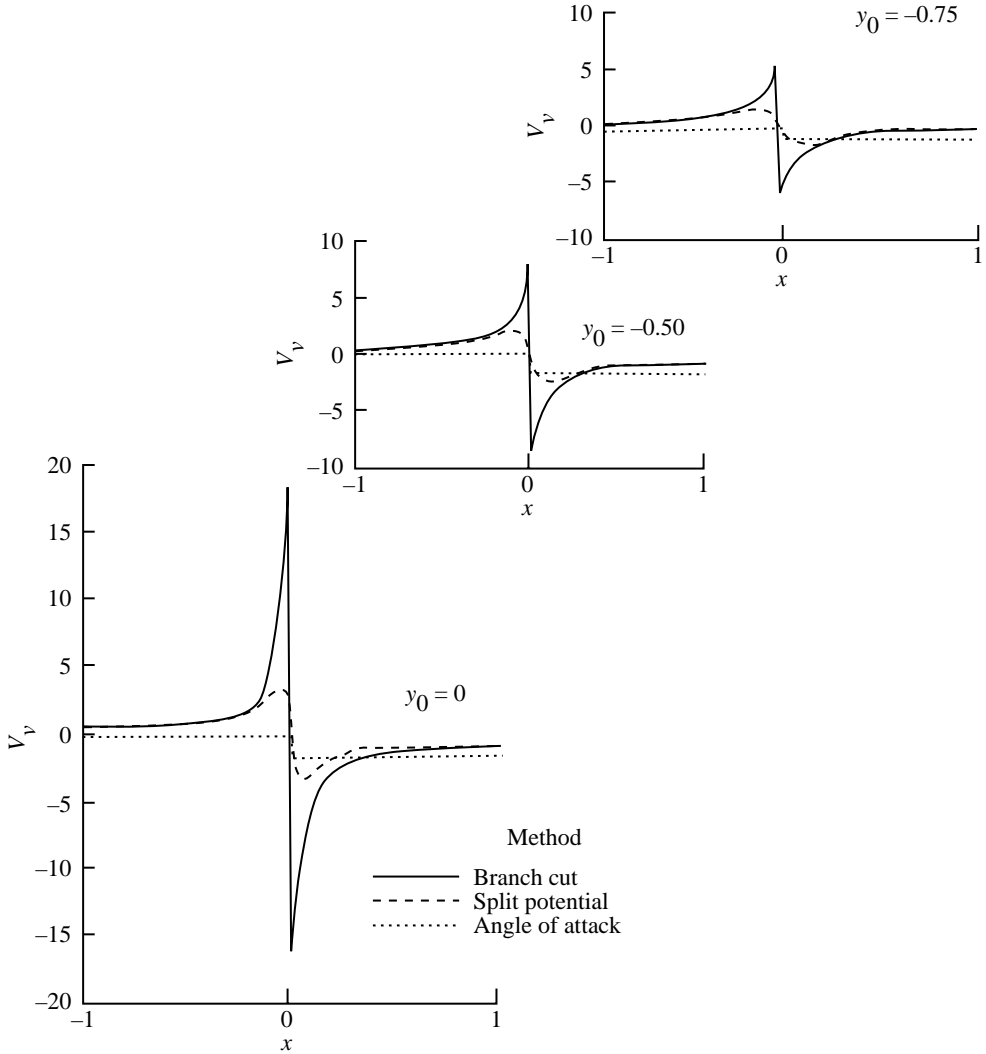


Figure 28. Vortex-induced velocity on airfoil surface.

#### 4.4. Comparison of Vortex Models

##### 4.4.1. Vortex Velocity Field

A straightforward way of comparing the four vortex models is to compare the induced velocity produced on the airfoil by each model. Figure 28 presents a series of vortices located at the airfoil leading edge and at selected vertical distances. These computations were made with a small disturbance mesh. (See section 2.2, step 1.) The computations were made for a flow field with no airfoil present in order to eliminate airfoil-induced velocities from the results. The lifting-surface model is not indicated in the figure because it has the same effect as the split-potential method. The angle-of-attack method in sharp contrast to the other methods is a simple step change in velocity. The branch-cut and split-potential methods both predict an impulsive type

velocity curve. The sharpness of the impulse is modified in the split-potential method by the vortex core. The velocity induced by the branch cut is generated implicitly by the model. These velocities tend to be higher than the others because of the interaction of the four subvortices with the dense grid region near the airfoil. Distance for the airfoil reduces the size of the velocities and reduces the differences produced by the vortex on the airfoil.

##### 4.4.2. Related Experiment

Comparison of the four vortex modeling methods is made with the help of experimental data. Caradonna, Laub, and Tung (ref. 28) presented experimental results for a rotor interacting with a vortex. The rotor had two blades with a constant 0012 airfoil section. The blades were untwisted and the rotor had a teetering hub. The rotor aspect ratio

was 7. A vortex was generated upstream of the rotor by a fixed, constant-section, NACA 0015 wing. Figure 29 depicts the experimental setup. When the rotor blade is at an azimuth angle of  $180^\circ$ , HSI occurs. Pressure at 10 locations on the airfoil surface were measured and these data were presented as a function of time (vortex location) and space (airfoil chord).

The data were collected for several rotor tip speeds and vortex locations. Two of these conditions are used as reference data in comparing the vortex models. The first condition is for a subcritical flow,  $M_\infty = 0.536$ , and a vertical miss distance of  $y_v = -0.433$ . The second case is for a critical flow,  $M_\infty = 0.714$ , and the same vertical miss distance.

There are two factors that compromise the correlation. The first factor is the low aspect ratio of the rotor. Because the present method is strictly two-dimensional, one should expect to see a higher pressure predicted due simply to aspect ratio effects. The second factor is the rotational velocity of the rotor. The measurements used in the comparison were made at an azimuth location of  $180^\circ$ . The effect of the vortex on the blade, however, begins much earlier. The blade is, therefore, experiencing a steadily changing free-stream flow modified by the vortex. The variable free stream is not modeled by the current method. For the subcritical flow, this does not pose a problem because unsteady effects are small at low Mach numbers. However, the critical flow is much more sensitive to this effect. The rotor is experiencing a high transonic speed at the azimuth location of  $90^\circ$  which decreases as the blade moves forward. As the speed decreases, the shocks on the airfoil surface begin to collapse. The vortex is encountered during this collapsing process. The computation of this flow field requires a three-dimensional model complete with an accurate unsteady shock model; this is beyond the capability of the current method.

#### 4.4.3. Subcritical Interaction

Comparison of the various vortex models is made first for a subcritical flow. The condition selected is the same as that used in the sample computation presented in the introduction, that is, an NACA 0012 airfoil at  $\alpha = 0^\circ$ ,  $M_\infty = 0.536$ , a vortex strength  $c_{l,v} = 0.496$ , and a constant miss distance of  $-0.433$  chord. This condition should be relatively insensitive to unsteady effects and free from shock waves.

Figure 30 shows lift versus vortex location for the four vortex models. The four methods show little difference in the initial condition solution. As

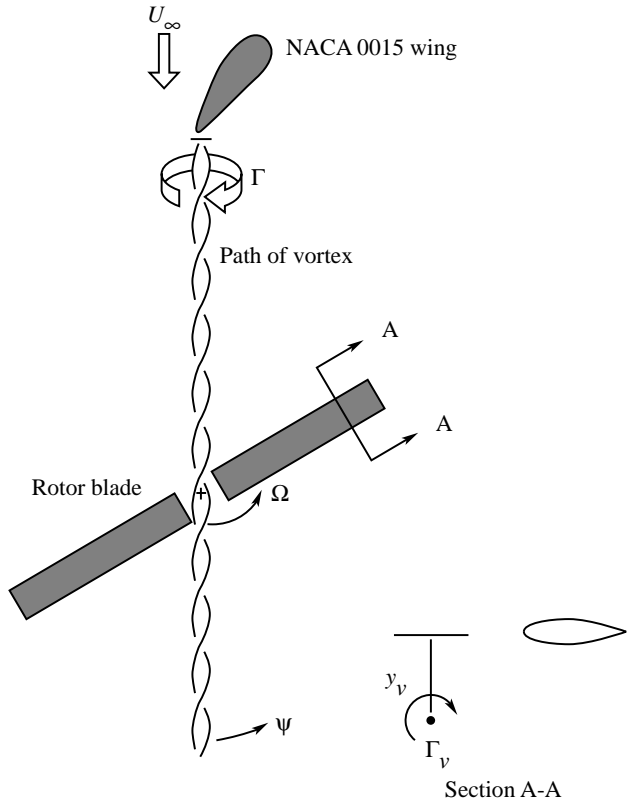


Figure 29. Experimental measurement of blade-vortex interaction.

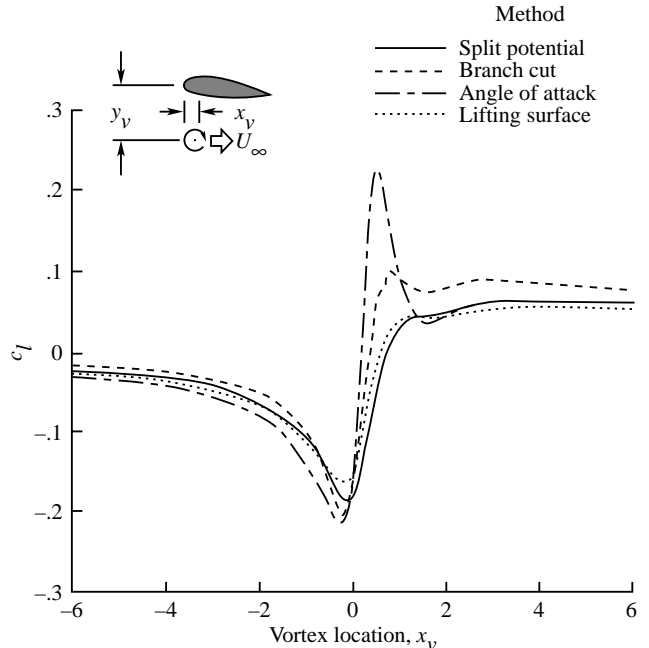


Figure 30. Variation of airfoil lift with vortex location for the four vortex models. Subcritical flow;  $a = 0.15$ ;  $\alpha = 0^\circ$ ;  $M_\infty = 0.536$ ;  $y_v = -0.433$ ;  $c_{l,v} = 0.496$ ; NACA 0012 airfoil; fixed path.

the vortex approaches, the curves begin to separate, reflecting the effect of the various methods on the flow-field solution. When the vortex is between 2 and 3 chords upstream, the separation of the curves becomes large. This point can therefore be considered the outer boundary of the close interaction. The curves continue to separate until they reach a maximum difference when the vortex is at the airfoil leading edge. During the interaction phase, the methods display several interesting features. The angle-of-attack method predicts a rapid (almost instantaneous) change in lift as the vortex passes the quarter-chord because the airfoil undergoes an abrupt change in angle of attack from negative to positive at this point; in effect the curve is inverted. An interesting feature of the branch-cut method is that during the interaction phase it predicts a small “spike” in the loading curve. This spike occurs when the vortex is in the densest part of the grid and reflects the locally high velocities predicted by this method. This spike increases in size as the Mach number increases. For a very strong interaction ( $M = 0.80$ ,  $y_v = -0.25$ , and  $c_{l,v} = 0.40$ ), this spike leads to an instability in the algorithm which destroys the solution. The split-potential and lifting-surface methods are in agreement overall even though they are somewhat different during the closest part of the interaction. Neither method shows any unusual features in their predicted loading histories.

Figure 31\* presents pressure time histories for the four methods. Here the difference between the lifting-surface and split-potential methods is more apparent. The spike in the branch-cut loading curve is also more apparent in figure 31(c) than in the integrated data. Figure 31(a) highlights the change in pressure on the airfoil caused by the sharp change in lift predicted by the angle-of-attack method.

Figure 32 presents measured and calculated data for each of the methods. Comparisons can only be considered qualitatively valid because of the aspect ratio and unsteady rotational flow field of the experiment. The split-potential, lifting-surface, and branch-cut methods all show qualitatively good comparisons but differ in detail. (Compare plots for 1 and 2 in figs. 32(b), (c), and (d).) The angle-of-attack method is clearly not accurate for this condition. (See plots for 1 and 2 in fig. 32(a).) This inaccuracy is caused by the sharp change in lift predicted by the model which clearly does not occur in the experiment.

#### 4.4.4. Critical Interaction

In section 4.4.3, the various vortex models were compared for a subcritical flow condition. A more interesting comparison is for a flow condition just below critical, that is, a flow condition which if undisturbed would remain subcritical. The introduction of a vortex in such a flow field would be expected to drive the flow into a supercritical state. An NACA 0012 airfoil at  $\alpha = 0^\circ$  and  $M = 0.714$  experiences this type of flow.

Figure 33 presents lift versus vortex location for each of the models at this “critical” flow condition. Inspection of this figure shows qualitatively the same results as the subcritical case: the models begin to separate between 2 and 3 chords upstream, the angle-of-attack method predicts a sharp “lift inversion” as before, the branch-cut method predicts a spike in the loading curve of increased size at this higher Mach number (0.714), and the split-potential and lifting-surface methods both predict smooth curves.

Figure 34 presents the pressure time histories on the airfoil. The angle-of attack and lifting-surface methods both predict pressure histories which are similar to those at the lower Mach number. However, the branch-cut and split-potential curves are markedly different. Both methods indicate the presence of shock waves although the branch-cut method is obscured by the presence of the spike. The presence of the shock wave in these models is more easily seen when comparing the measured and calculated data (fig. 35). The split-potential method predicts a shock which is also present in the data. (See plots for 2, 3, and 4 in fig. 35(d).) The branch-cut method predicts a sharp pressure peak which appears to be the beginning of a shock formation; however, the velocity spike may be delaying the formation. The lifting-surface and angle-of-attack methods do not predict shocks.

The surface specification models also predict that the vortex affects the pressure on both surfaces of the airfoil. This is caused by the assumption of infinite signal speed which is inherent in these methods. The explicit methods show an effect on the lower surface only due to the additional time required for the signal to arrive at the upper surface.

#### 4.4.5. Summation

The previous discussions show that all four models produce qualitatively similar results for the integrated load but differ considerably in detail. The split-potential and lifting-surface methods produce

---

\*Figures 31 through 47 are at the end of section 4.

the most accurate curves for integrated loads. Direct comparison between computation and experiment is not possible except in the most qualitative sense because the experiment contains large three-dimensional and unsteady effects which are not modeled in the theory. The angle-of-attack and branch-cut methods both generate spurious spikes in the loading curve. Comparison of the pressure time histories of the models shows considerable differences in the details of the pressure loading. Comparison of the methods for a critical flow condition shows that only the explicit models predict the presence of supercritical flow. Only the explicit models are capable of predicting the variation in local Mach number which is necessary to capture accurately the nonlinear nature of the flow field. Numerous computational experiments have indicated that the split-potential method is the most robust of these two methods. It also allows for more control of the vortex modeling because it models the vortex as a specified velocity field. In fact the method is not restricted to modeling vortices and can be used to predict the effect of any flow field which is described by a known irrotational potential function. Because of this versatility and robustness, the split-potential method is the recommended method. The rest of the calculated results presented in this report were generated by using the split-potential method.

#### 4.5. Parametric Sweeps

This section contains a study of the effect of several key parameters on HSI. The split-potential method is used in all comparisons.

##### 4.5.1. Effect of Mach Number

One of the key parameters is Mach number. For an airfoil in steady flow, the effect of increased Mach number is the increase in local velocities on the surface which leads to lower surface pressures. The variation of the local pressure and lift coefficient can be predicted with good accuracy by using the Prandtl-Glauert correction. As the Mach number increases the local velocities increase until, finally, a shock develops on the surface of the airfoil. The linear Prandtl-Glauert correction breaks down completely with the onset of local sonic flow, and the problem becomes nonlinear.

The presence of a vortex in the flow simply adds an extra component to the local velocity because of the induced velocity field which the vortex generates. This extra velocity tends to induce the supercritical flow at a free-stream Mach number lower than the critical point for the airfoil alone. Figure 36 shows the effect that Mach number has on the blade-vortex

interaction. The three curves are for an NACA 0012 airfoil at  $\alpha = 0^\circ$  and  $c_{l,v} = 0.40$ . The miss distance is  $-0.251$  chord, the vortex core size is 0.05 chord, and the path of the vortex is specified by setting the vortex velocity equal to the free-stream value. The Mach numbers are 0.4, 0.6, and 0.8. Almost no difference is seen between the subcritical flows except during the interaction and departure phases. The supercritical flow, however, shows a broader pulse width than the subcritical flows. This effect was also noted experimentally in reference 28 and is caused by the effect of signal propagation speed. The signal speed is the sum of the speed of sound and the flow velocity. The waves propagating from an upstream vortex arrive at the airfoil sooner for a higher speed interaction. A wave generated by a downstream vortex takes longer to arrive at the airfoil, and hence, the effect of the vortex decreases more gradually if the propagation speed is increased. This is reflected in the figure as a separation of the curves during the interaction and departure phases. Figure 37 presents the pressure distributions on the airfoil surface for selected vortex locations. The curves reflect the effect of Mach number and strongly resemble the variation one might see for an isolated airfoil at negative angle of attack except for the suction peaks induced when the vortex is very near to the blade surface.

##### 4.5.2. Effect of Vortex Strength

A helicopter rotor airfoil interacts with a series of vortices generated by the preceding blade. The strength of these vortices is dependent upon the conditions under which the generating blade sheds them. Modeling vortex strength and understanding its effect are, therefore, important. The primary effect of vortex strength is to increase the peak velocities generated by the vortex and consequently the velocities imposed on the airfoil. This effect can be deduced from the tangential velocity equation (eq. (3.3)). An interaction of particular interest would be the “critical” interaction described in section 4.5.1. Figure 38 is the integrated lift history of an NACA 0012 airfoil for three different vortex strengths ( $c_{l,v} = 0.20$ , 0.40, and 0.60) for the critical Mach number 0.714. The loading curve shows what appears to be a linear variation with vortex strength. However the airfoil pressures (fig. 39) show an increasingly stronger shock wave on the airfoil surface. (See plots for 3 and 4 in fig. 39.) The shock location and strength vary linearly with the vortex strength. For strong vortices ( $c_{l,v} = 0.60$ ), the shock extends into the flow field and interacts with the vortex directly to cause very high suction peaks. (See plot for 3 in fig. 39(c).)

#### 4.5.3. Effect of Miss Distance

The location of the vortices also affect the airfoil response. Consider again equation (3.3) and note that the geometry effect is primarily in the denominator. The effect of miss distance should be the inverse of the effect of  $c_{l,v}$ . Figure 40 shows the effect of miss distance on the integrated lift history of an NACA 0012 airfoil at  $M_\infty = 0.714$ ,  $\alpha = 0^\circ$ , and  $c_{l,v} = 0.40$ . The miss distance varies from  $y_v = -0.75$  to  $-0.25$ . The miss-distance variation in figure 40 is strictly a vertical displacement. Since the peak vortex velocity depends on radial distance, the effect of a vertical displacement does not become large until the proportion of  $\mathbf{r}$  which it contributes is large. This effect begins to occur at approximately 1 chord upstream from the airfoil leading edge. After this point, the change in loading appears to vary linearly with the inverse of the miss distance. The pressure distribution curves (fig. 41) show a similar trend with respect to shock strength and location.

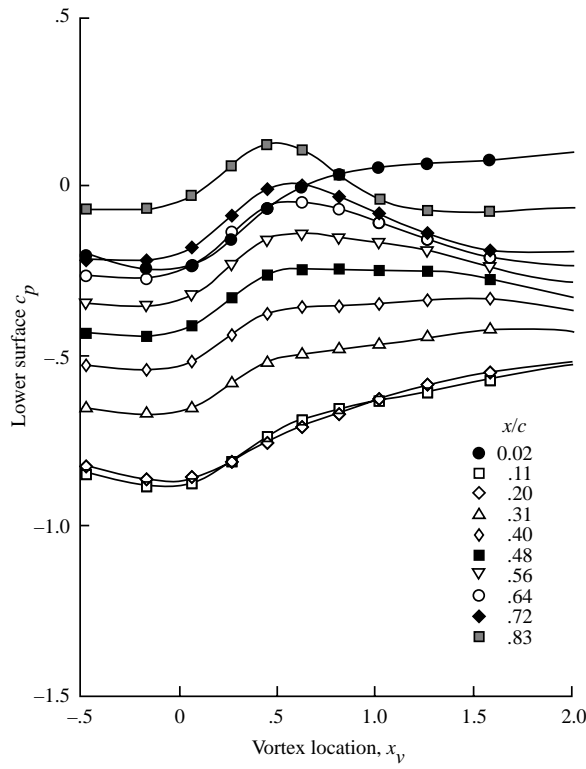
#### 4.5.4. Effect of Core Size

The effect of core size on the airfoil response is more intricate. In equation (3.3), the vortex core size has the effect of modifying the denominator. As  $a$  increases, the denominator grows for a given value of  $r$ . Furthermore, the minimum value of lift occurs at the minimum value of the denominator when the vortex is at the leading edge. After this point,  $r$  increases and  $V$  decreases. At the point where  $r$  is a minimum, the value of  $a$  determines  $V$ . The effect of  $a$  is, therefore, to change the effective location of the vortex, and this is what gives rise to the phase shift in figure 42. Figure 42 shows the pressure on the airfoil surface at selected vortex locations. As before, the shock strength and location vary directly with the inverse of  $a$ .

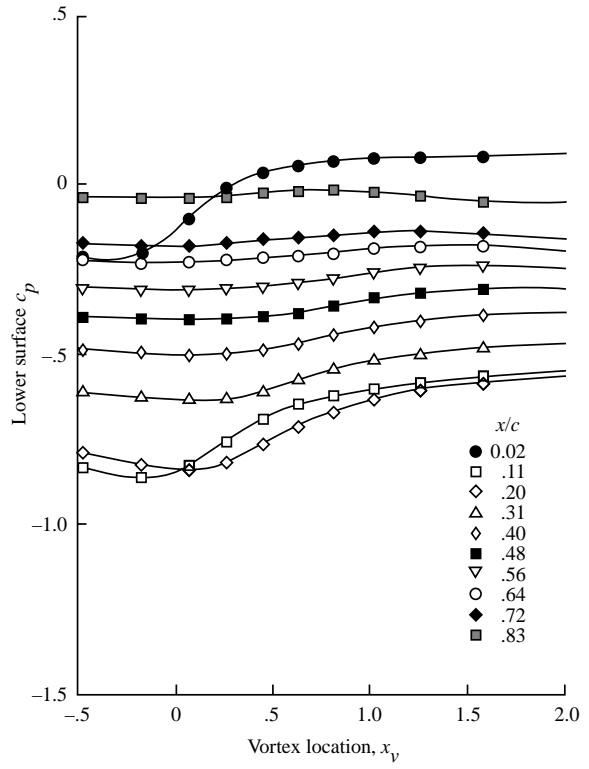
#### 4.5.5. Effect of Angle of Attack

A helicopter rotor blade experiences a cyclic change in angle of attack as it rotates. The effect of the airfoil angle of attack on BVI is therefore important. The angle of attack of the airfoil affects the response primarily by changing the initial conditions of the solution. Figure 44 shows the effect of  $\alpha$  on the interaction between an NACA 0012 airfoil and a vortex of strength  $c_{l,v} = 0.40$ . The Mach number is 0.60 and  $\alpha = 0^\circ$ ,  $0.5^\circ$ , and  $1^\circ$ . The lift history for the curve for  $\alpha = 0^\circ$  has been subtracted from the others to illustrate the difference between the interactions. As can be seen in the figure, the effect of angle of attack is purely linear for this subcritical interaction. The airfoil pressure distributions are presented in figure 45. One interesting feature is that the suction peaks on the airfoil are reduced as the angle of attack increases. (See plots for 2 and 3.) The positive angle of attack tends to offset the effect of the vortex which induces a negative lift.

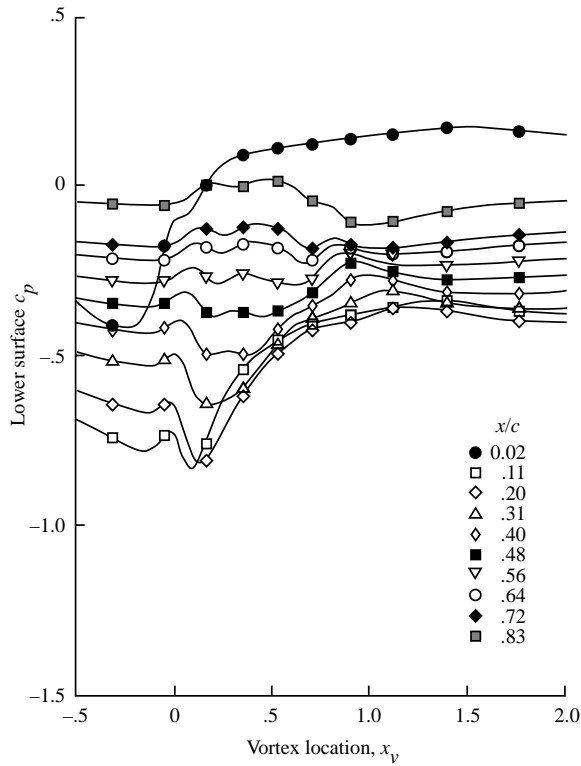
The effect of angle of attack at a transonic Mach number is similar to that at subsonic conditions. Figure 46 presents integrated lift curves for a Mach number of 0.8 and the same conditions as figure 44. The pressure coefficients indicate a decrease in shock strength as the airfoil angle of attack increases. An inverse effect would lead to increased shock strength with increasing negative angle of attack. A combination of high negative vortex strength and high negative angle of attack would produce a very strong shock which could possibly lead to a shock-induced separation. The very high suction peaks ( $c_p = -1.5$ ) seen in the airfoil pressure distributions (plots for 3 in figs. 47(a), (b), and (c)) occur as the vortex moves through the supersonic region near the airfoil surface.



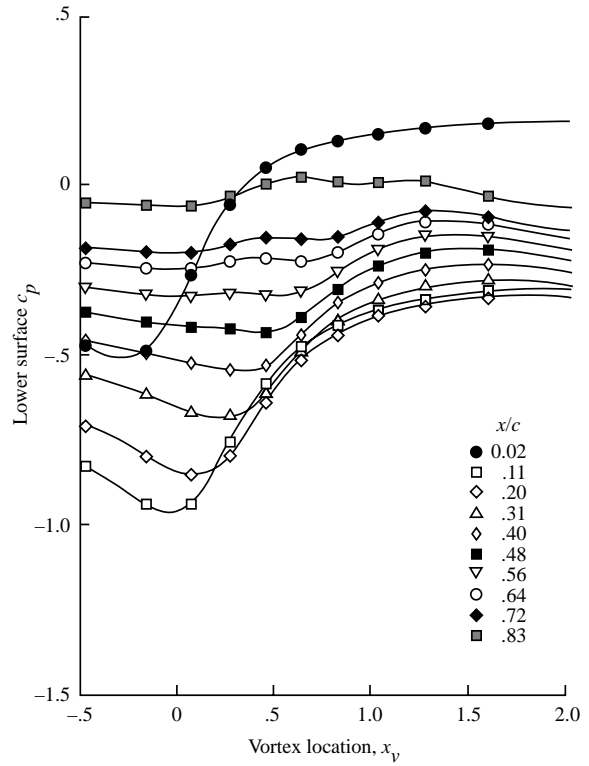
(a) Angle-of-attack method.



(b) Lifting-surface method.

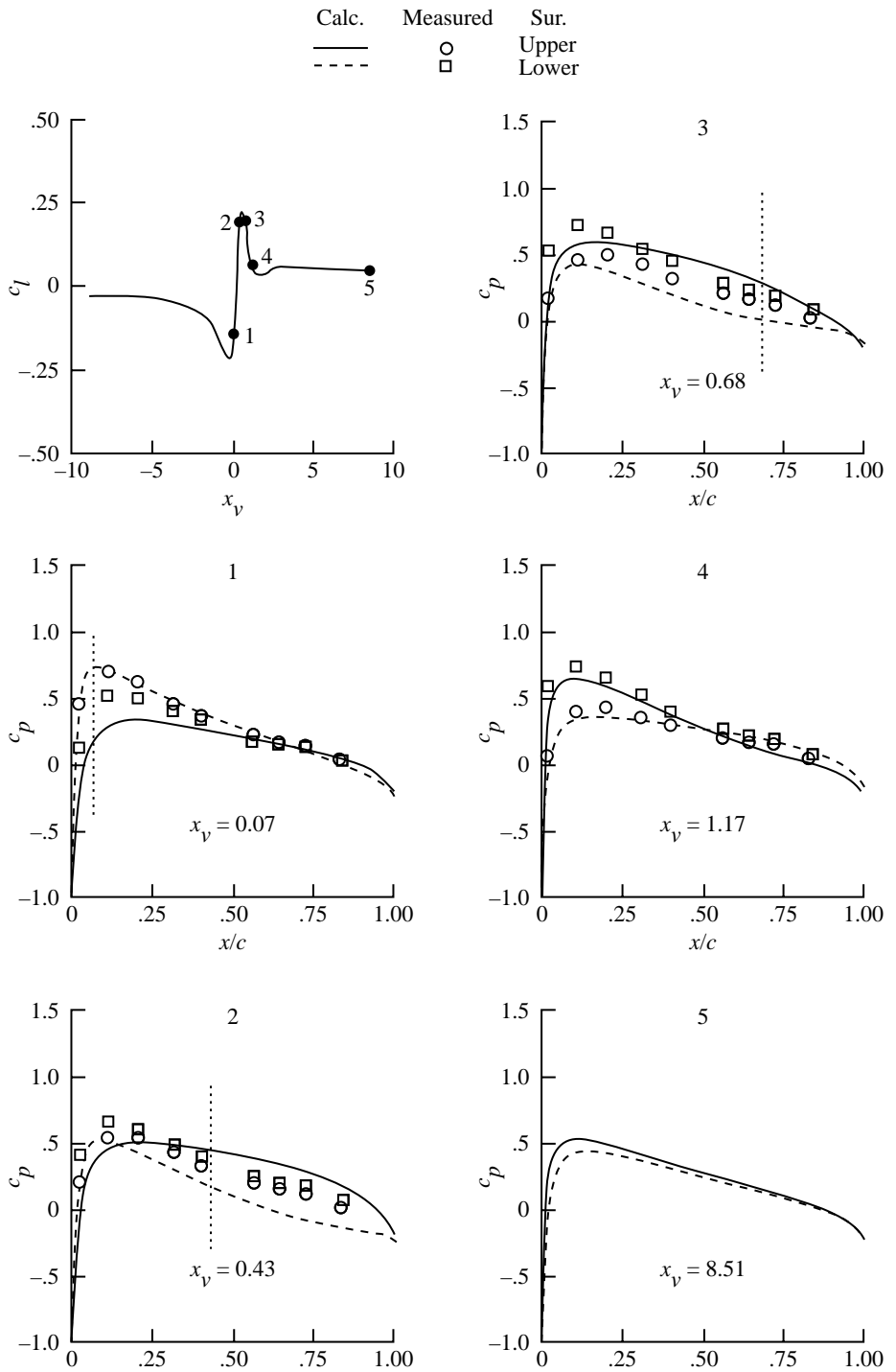


(c) Branch-cut method.



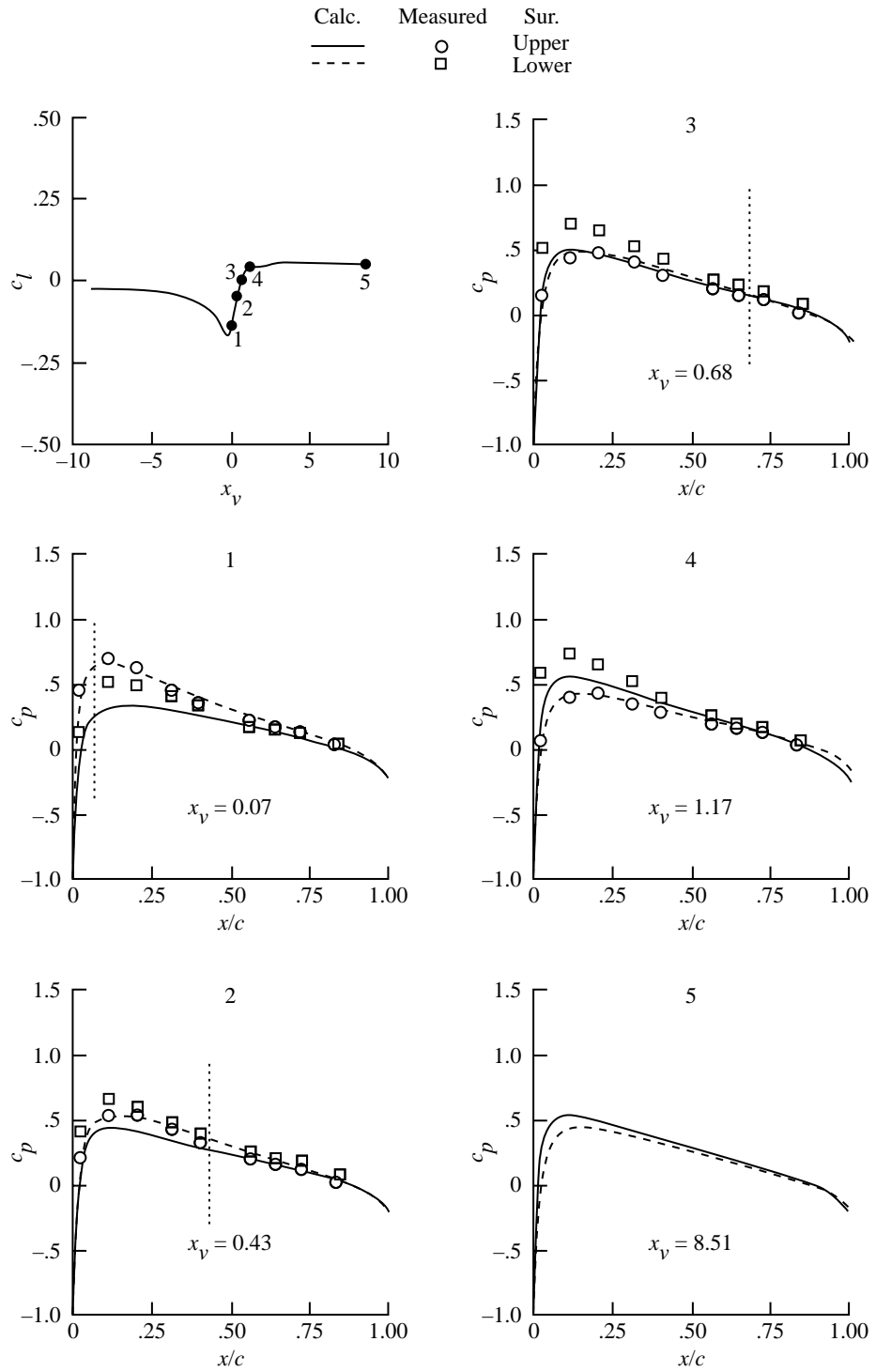
(d) Split-potential method.

Figure 31. Variation of airfoil pressure with vortex location. Subcritical flow.



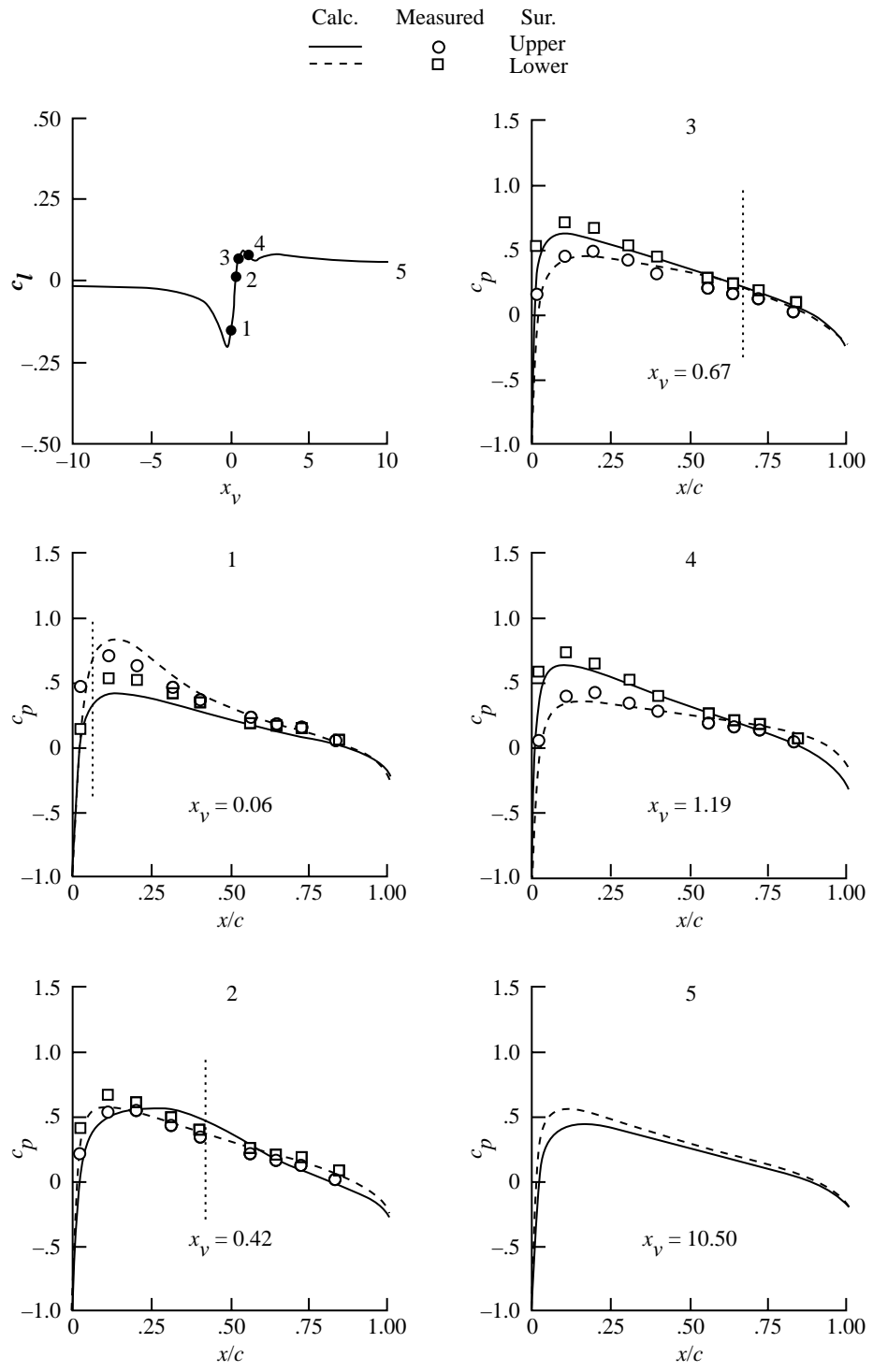
(a) Angle-of-attack method.

Figure 32. Computed and measured airfoil surface pressures for  $M_\infty = 0.536$ .  $\alpha = 0^\circ$ ;  $y_v = -0.433$ ;  $c_{l,v} = 0.496$ ; NACA 0012 airfoil.



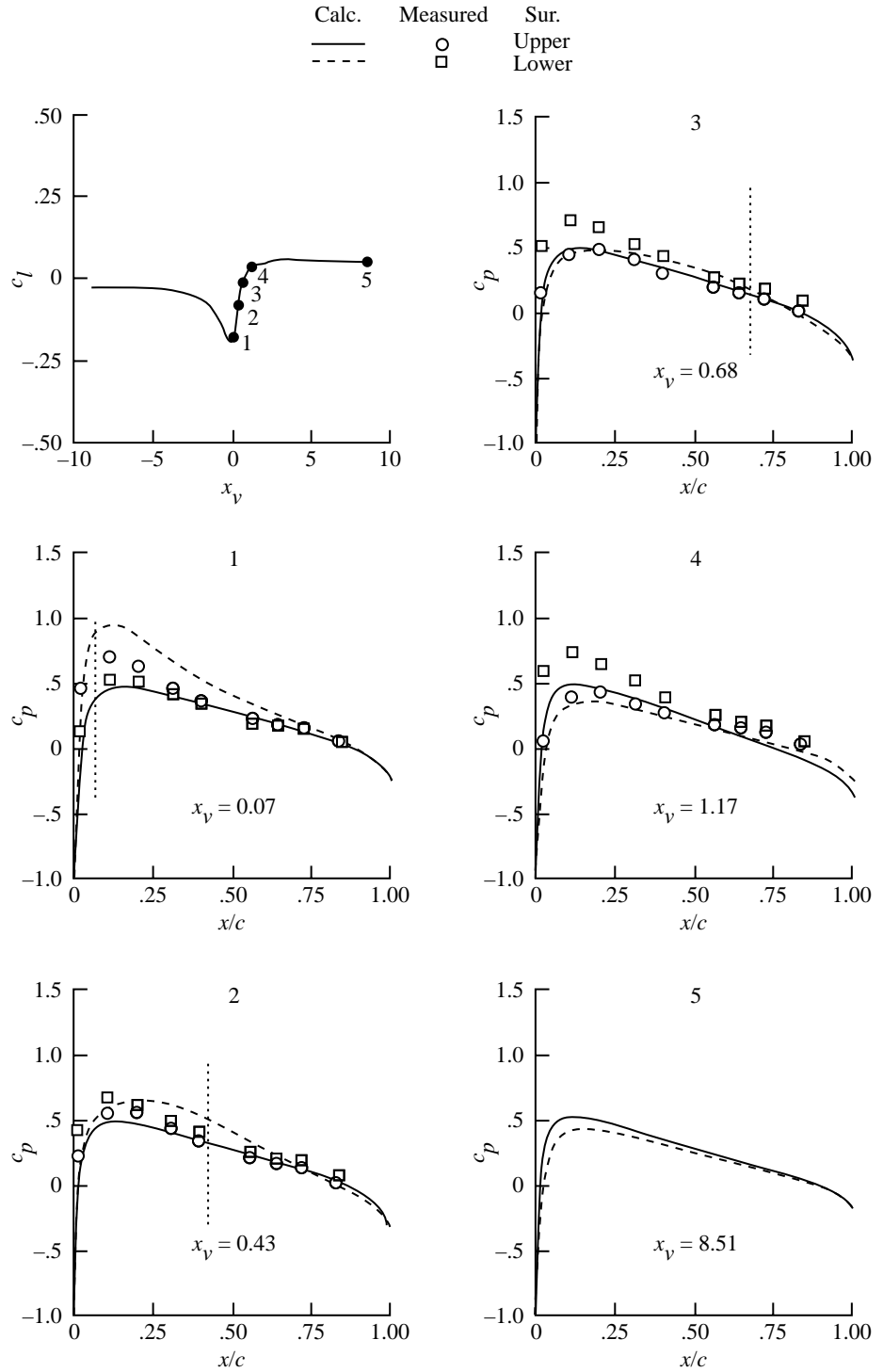
(b) Lifting-surface method.

Figure 32. Continued.



(c) Branch-cut method.

Figure 32. Continued.



(d) Split-potential method.

Figure 32. Concluded.

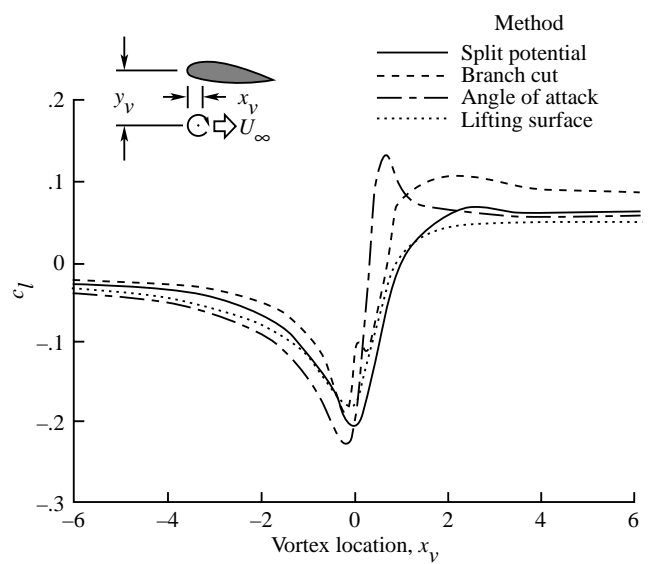
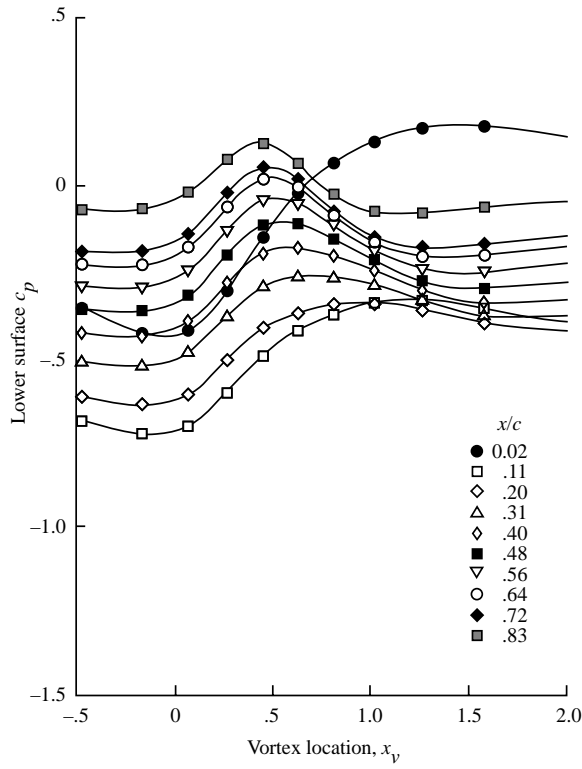
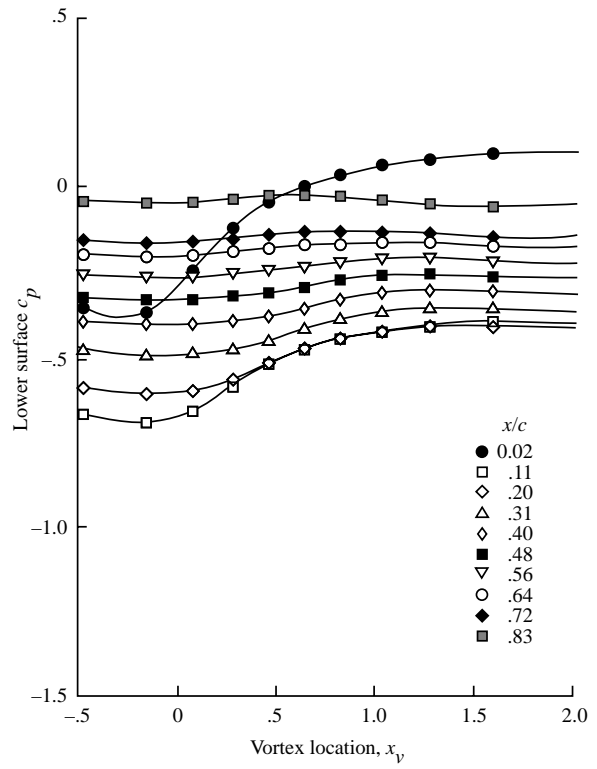


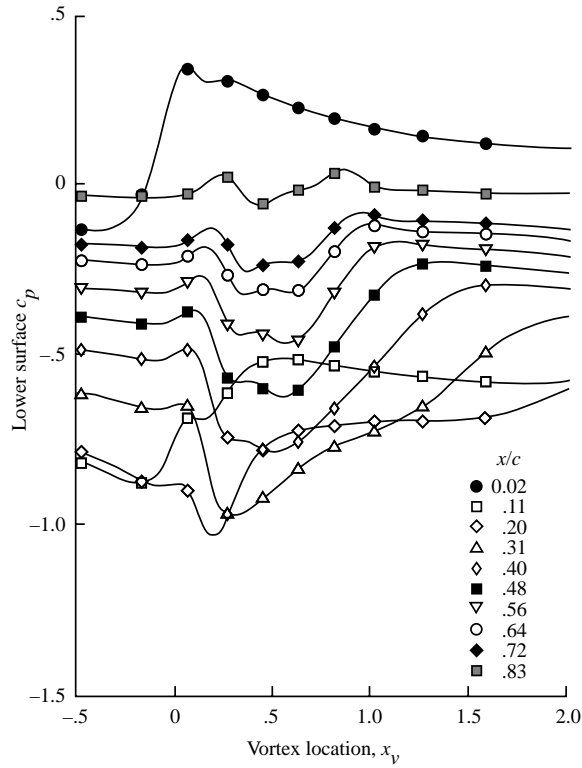
Figure 33. Airfoil lift variation with vortex location for the four vortex models at critical flow.  $a = 0.15$ ;  $\alpha = 0^\circ$ ;  $M_\infty = 0.714$ ;  $y_v = -0.433$ ;  $c_{l,v} = 0.495$ ; NACA 0012 airfoil; fixed path.



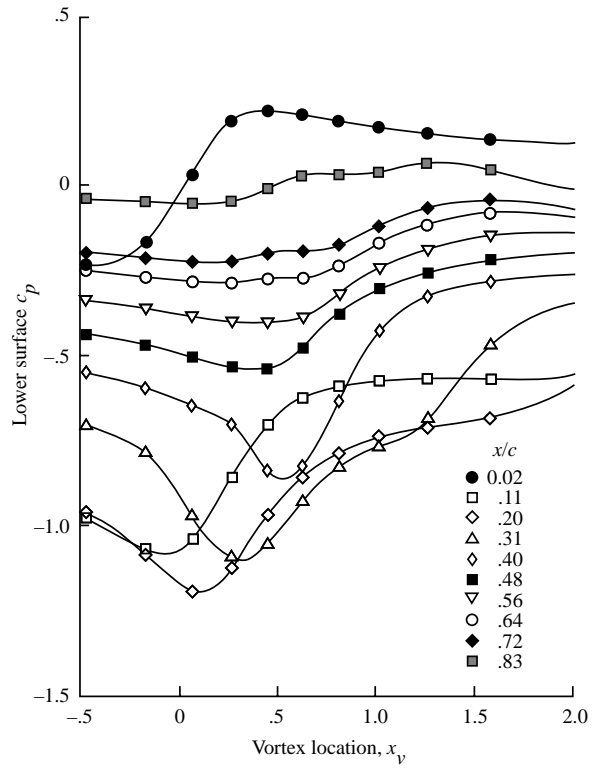
(a) Angle-of-attack method.



(b) Lifting-surface method.

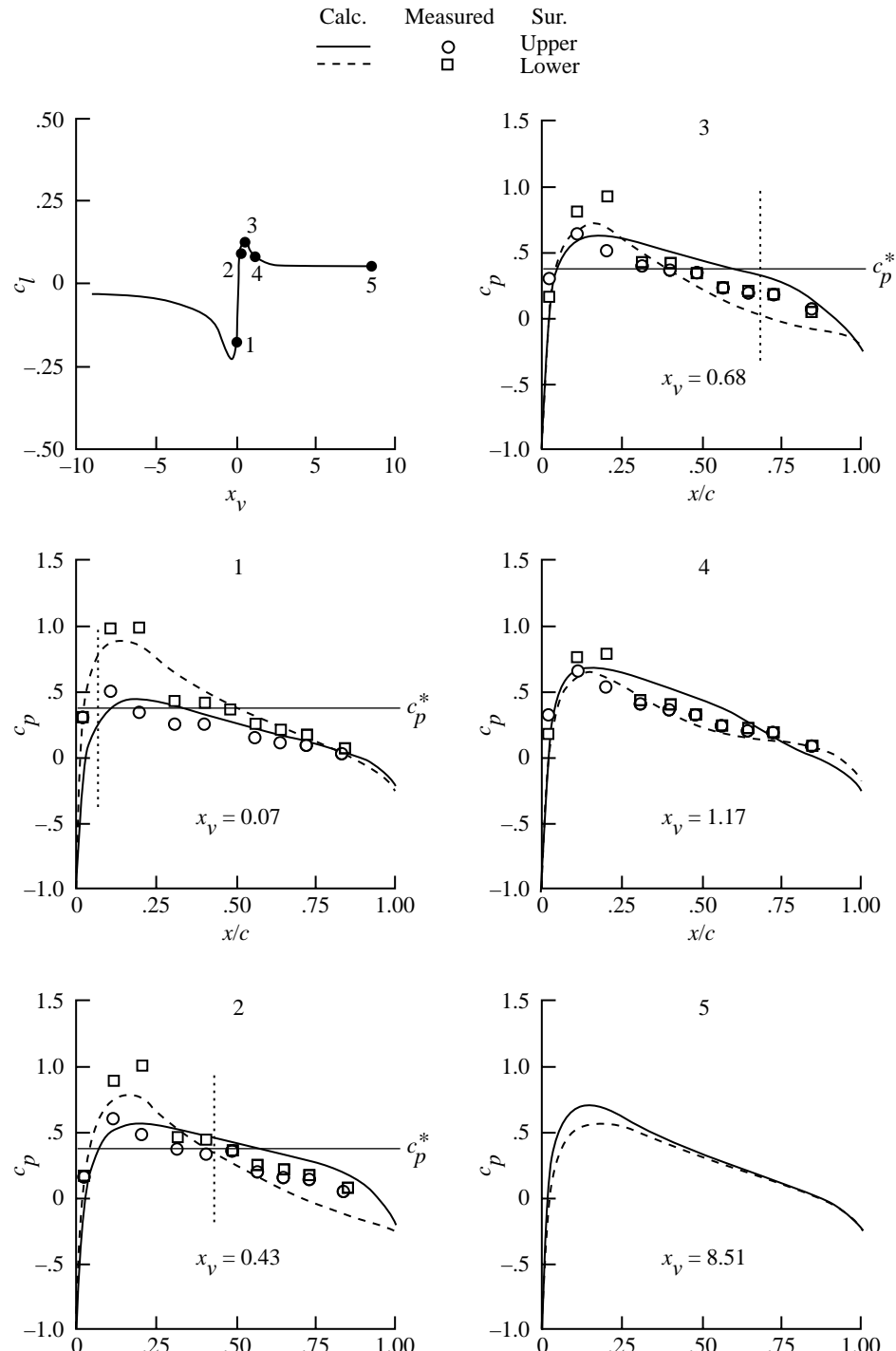


(c) Branch-cut method.



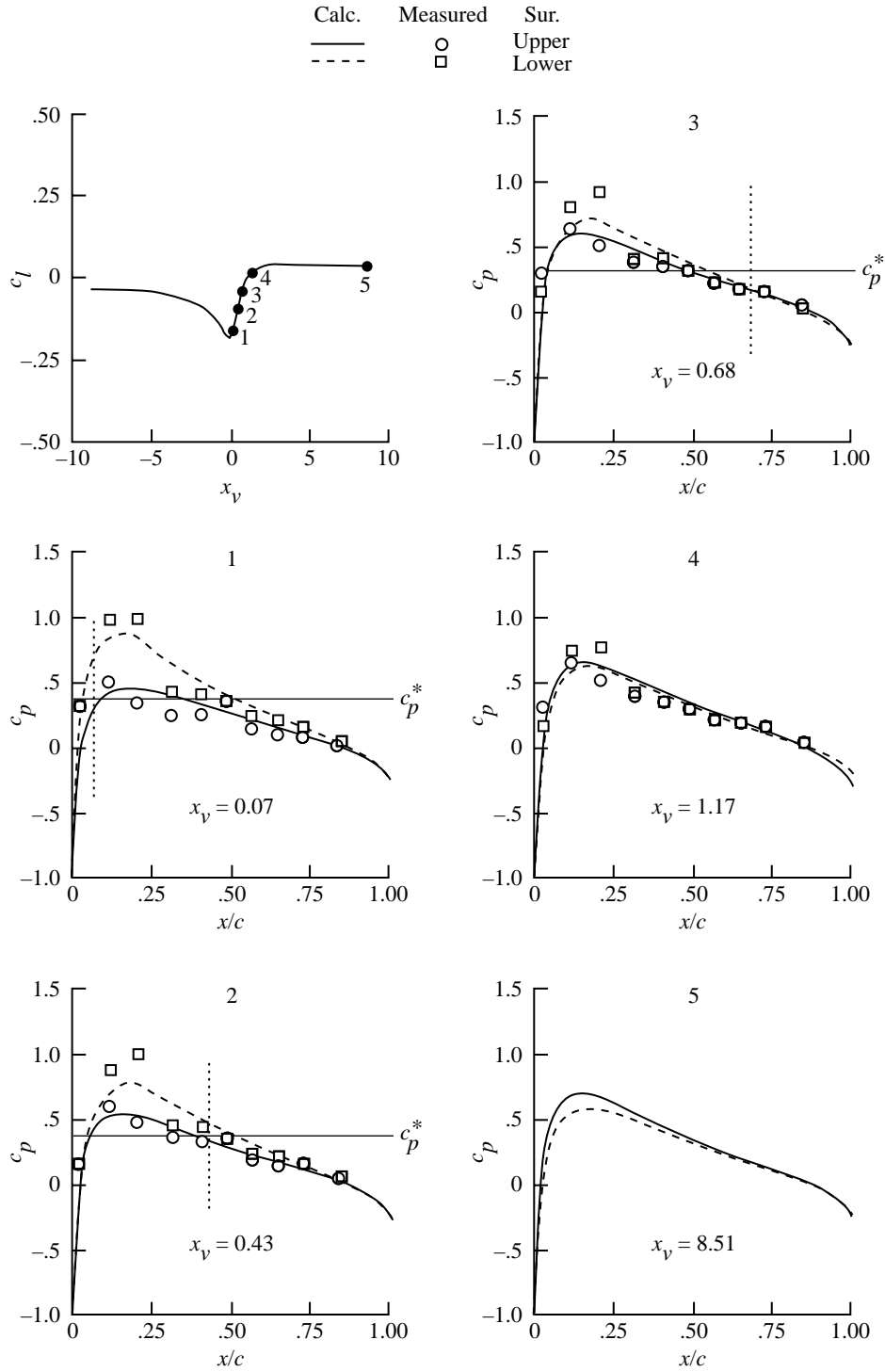
(d) Split-potential method.

Figure 34. Variation of airfoil pressure with vortex location at critical flow.



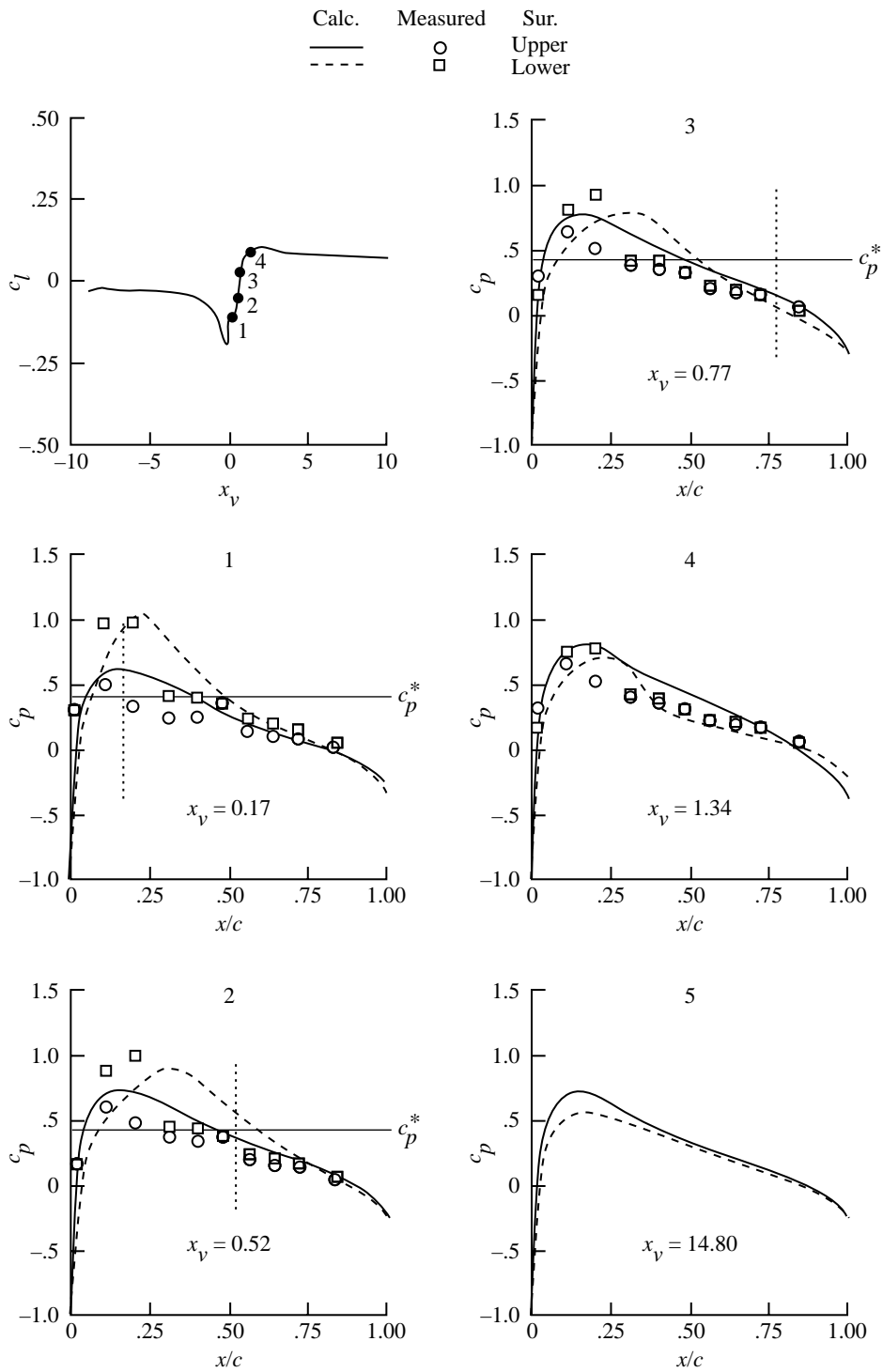
(a) Angle-of-attack method.

Figure 35. Computed and measured airfoil surface pressures for  $M_\infty = 0.714$ ,  $\alpha = 0^\circ$ ;  $y_v = -0.433$ ;  $c_{l,v} = 0.496$ ; NACA 0012 airfoil.



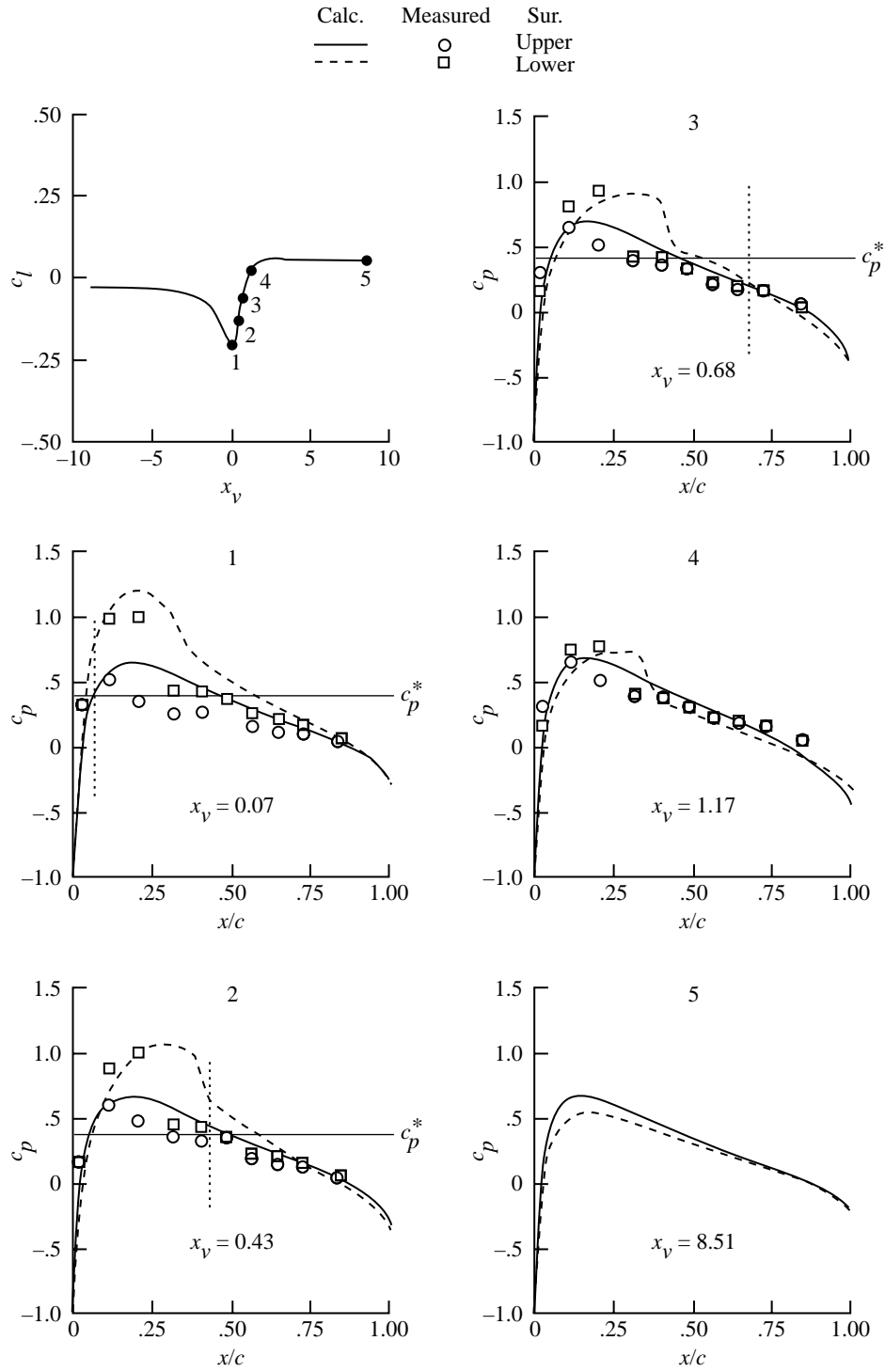
(b) Lifting-surface method.

Figure 35. Continued.



(c) Branch-cut method.

Figure 35. Continued.



(d) Split-potential method.

Figure 35. Concluded.

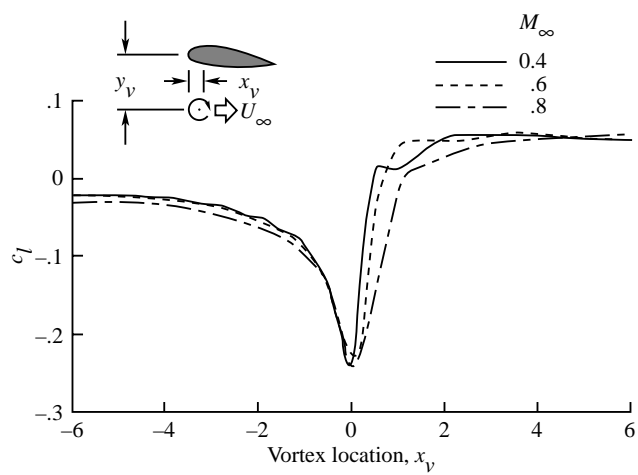
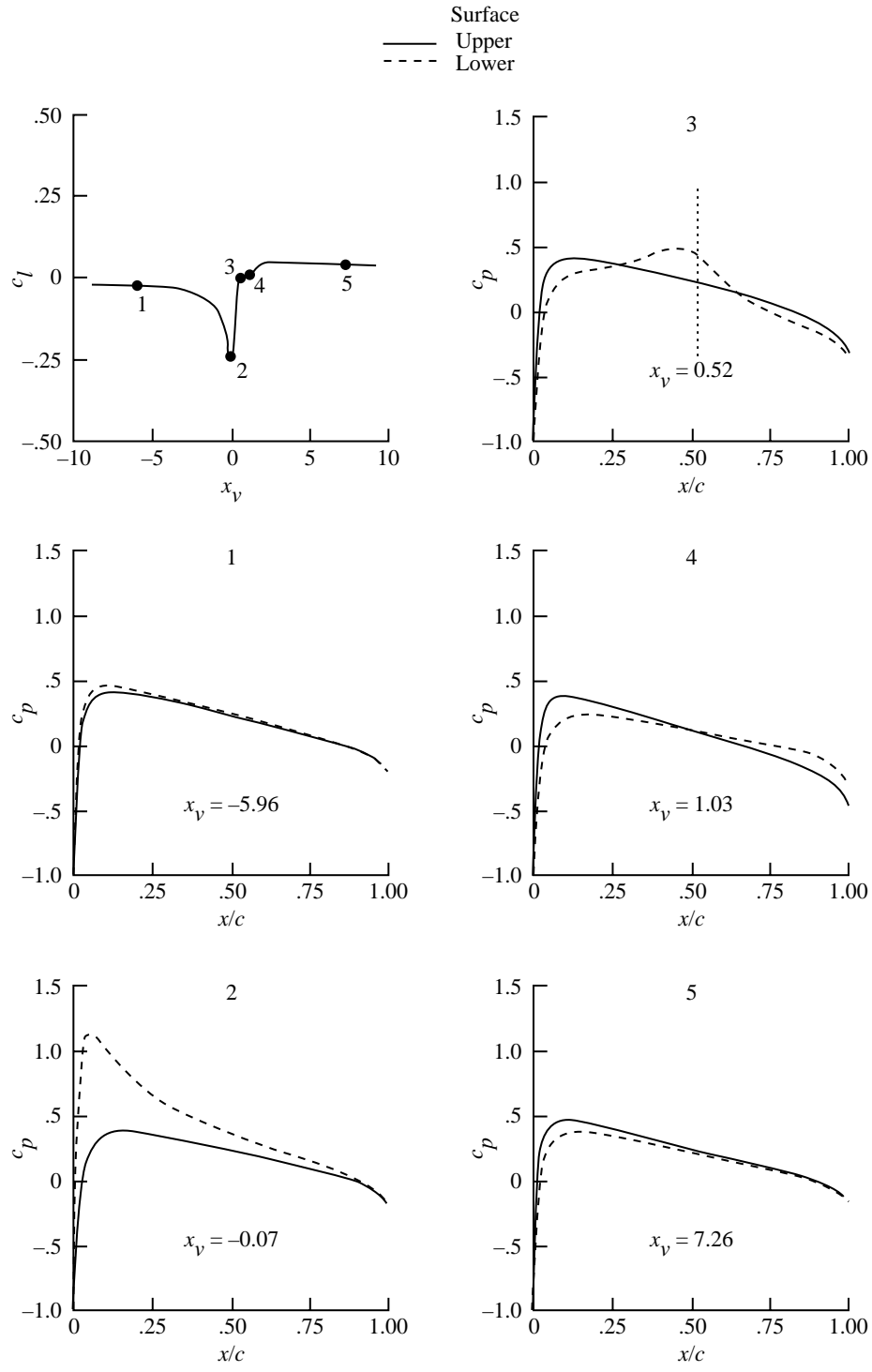
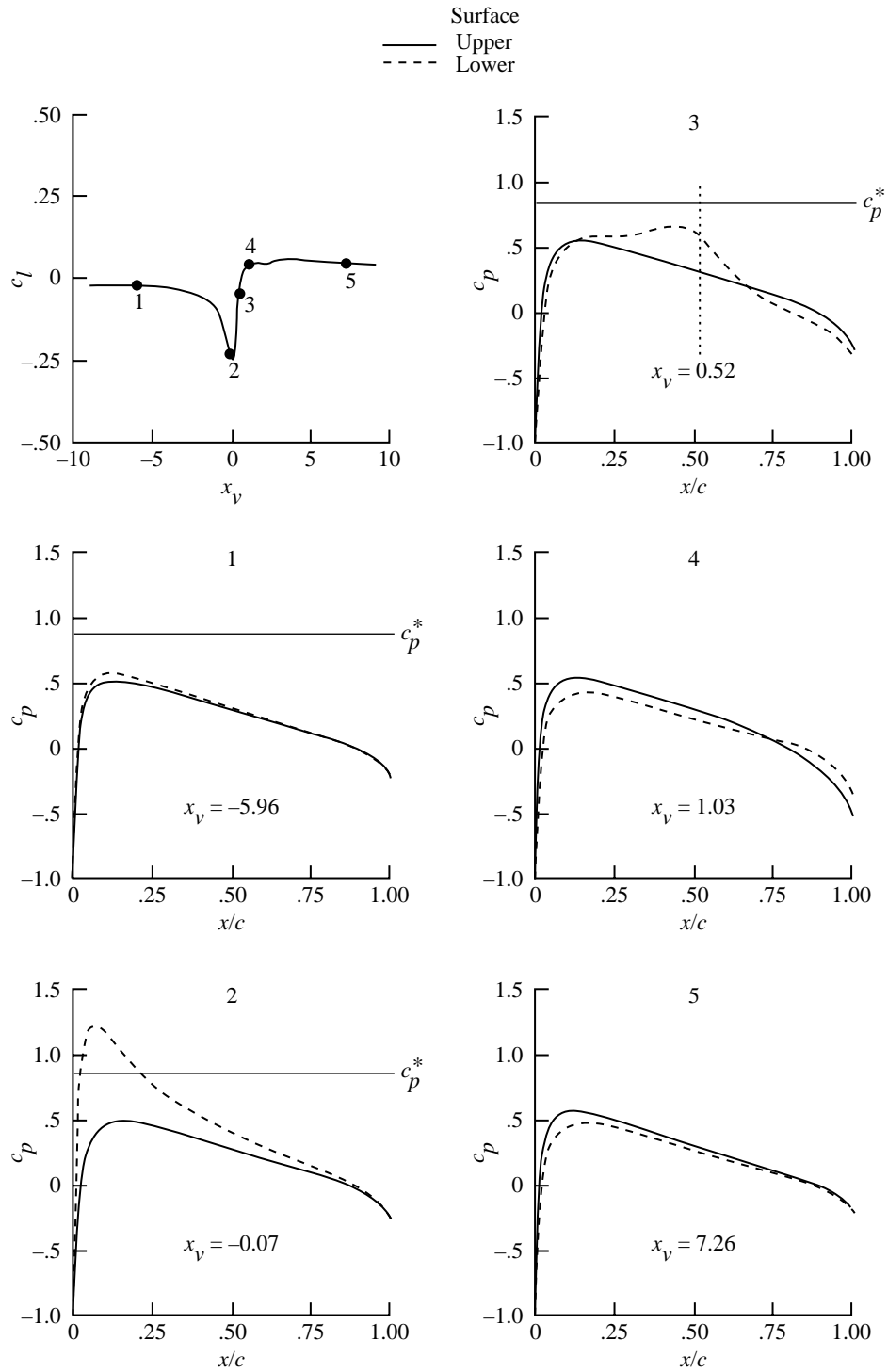


Figure 36. Effect of Mach number on variation of airfoil lift.  $a = 0.05$ ;  $\alpha = 0^\circ$ ;  $y_v = -0.251$ ;  $c_{l,v} = 0.400$ ; NACA 0012 airfoil; fixed path.



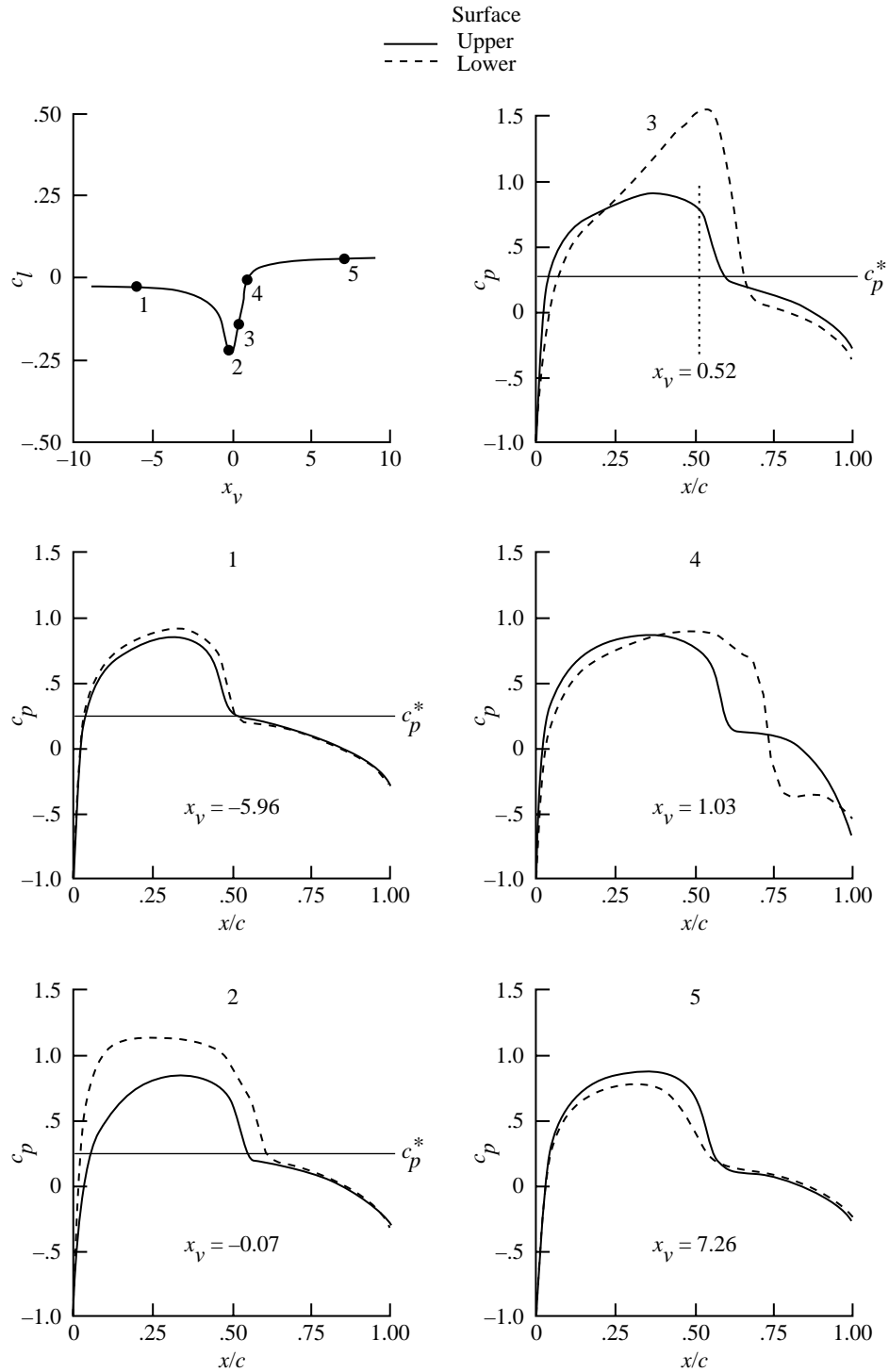
(a)  $M_\infty = 0.40$ .

Figure 37. Airfoil pressure distribution at selected vortex locations for several free-stream Mach numbers.



(b)  $M_\infty = 0.60$ .

Figure 37. Continued.



(c)  $M_\infty = 0.80$ .

Figure 37. Concluded.

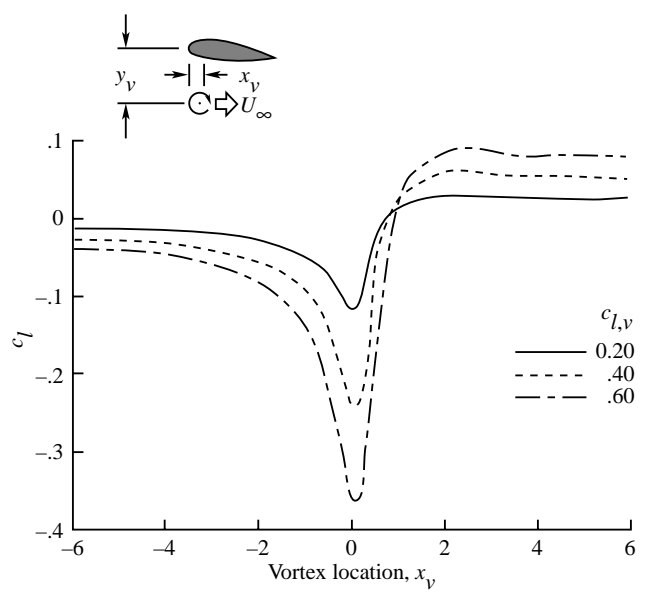


Figure 38. Effect of vortex strength on variation of airfoil lift.  $a = 0.05$ ;  $\alpha = 0^\circ$ ;  $M_\infty = 0.714$ ;  $y_v = -0.251$ ; NACA 0012 airfoil; fixed path.

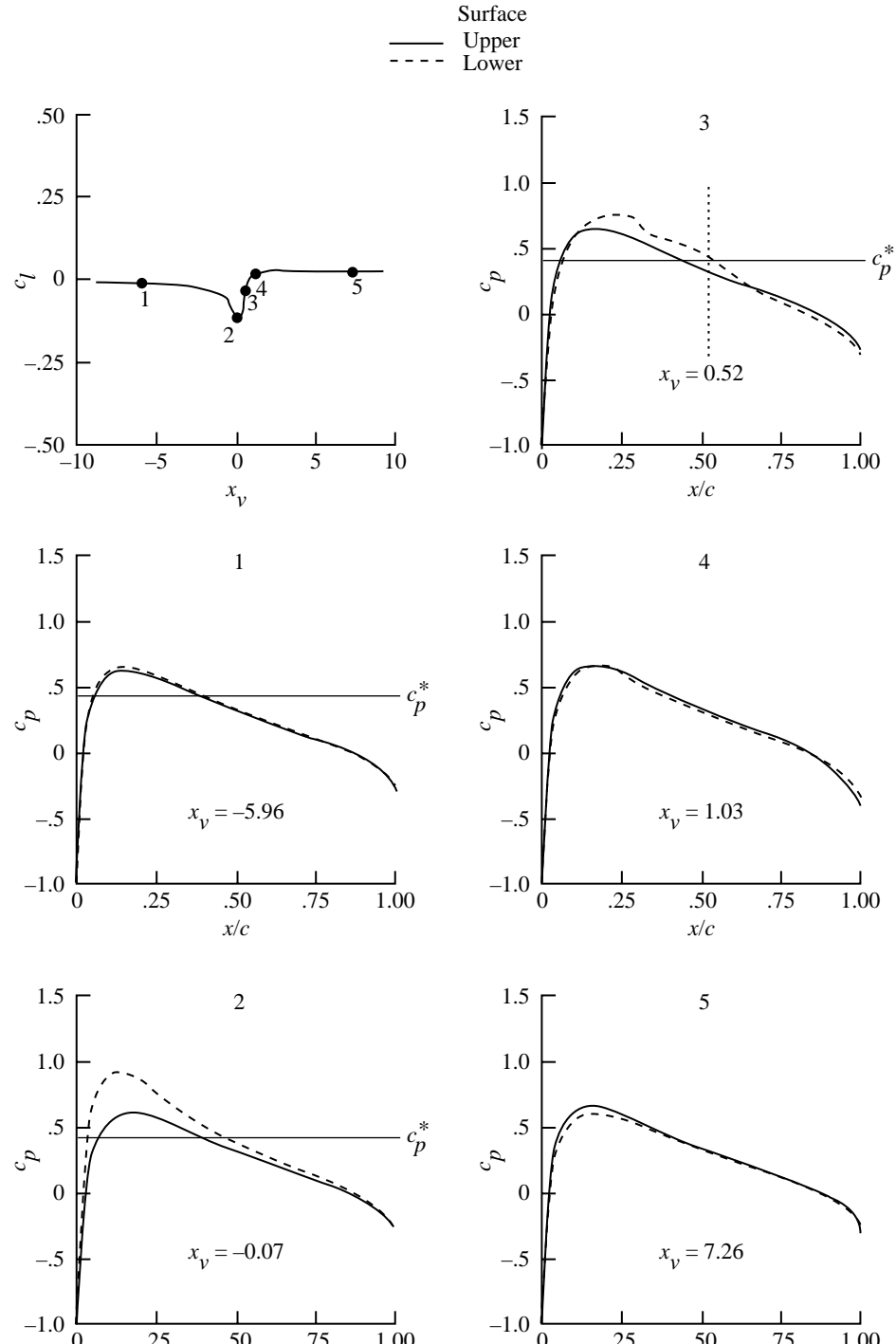
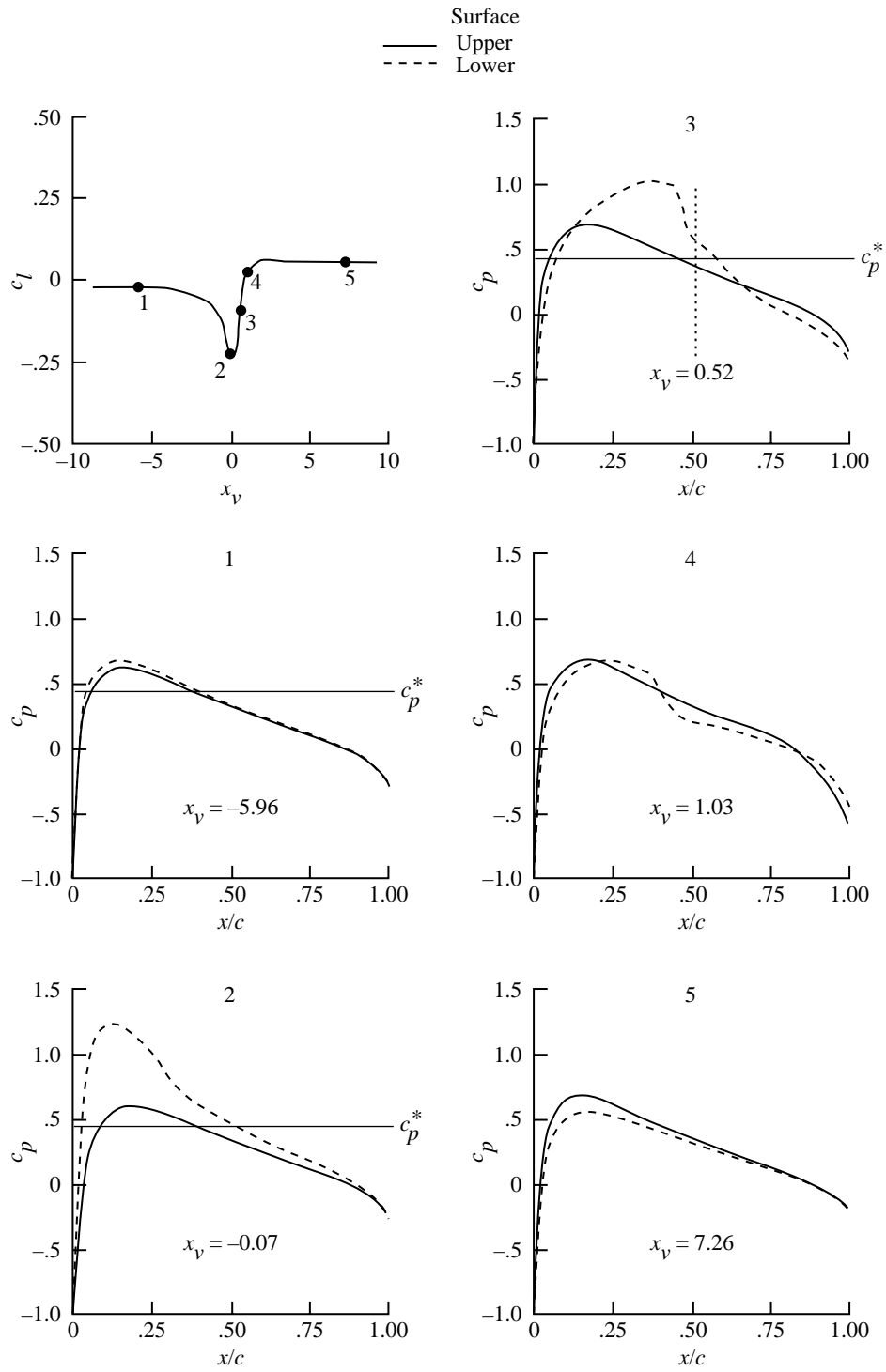
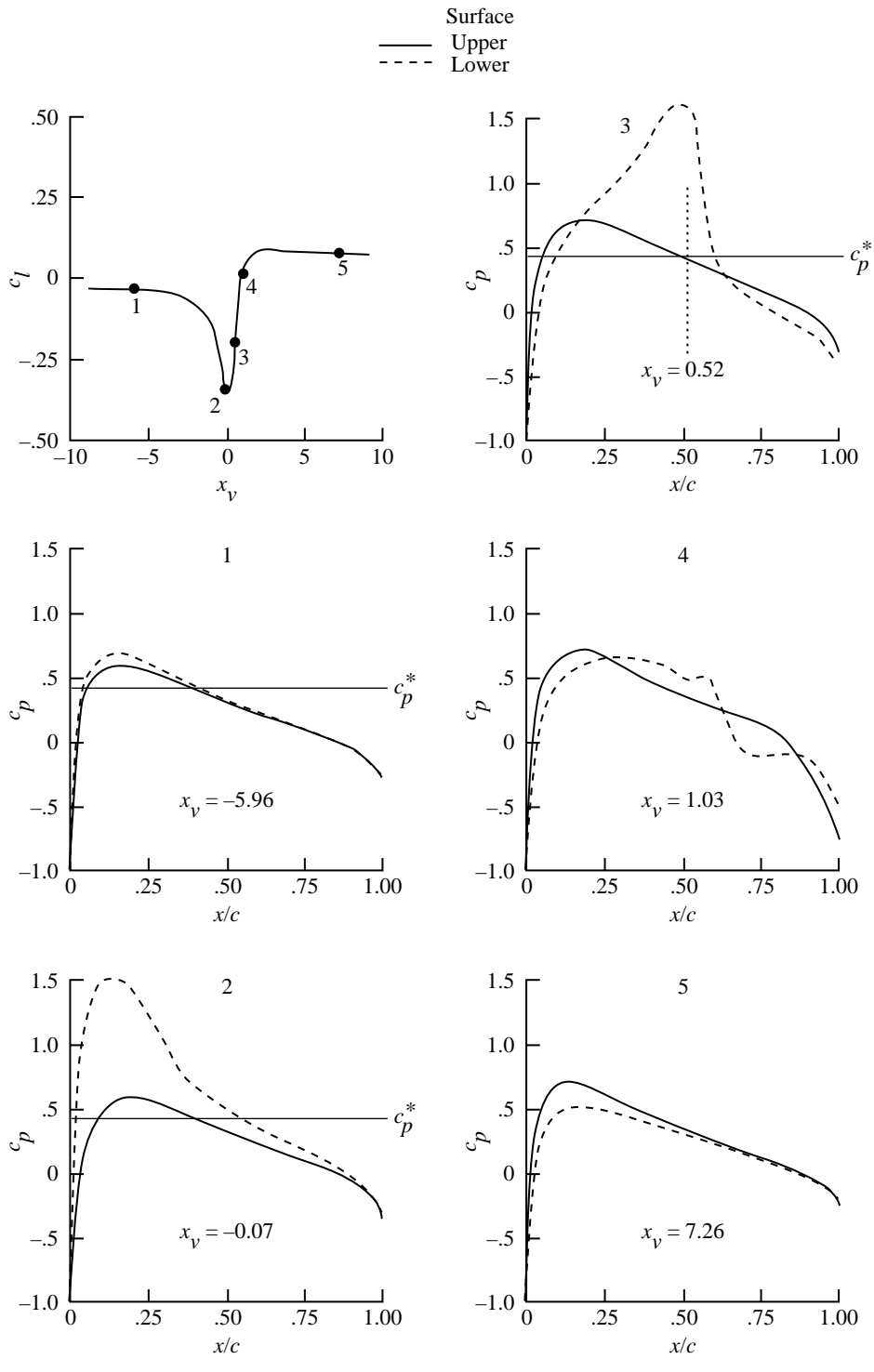


Figure 39. Airfoil pressure distribution at selected vortex locations for several vortex strengths.



(b)  $c_{l,v} = 0.4$ .

Figure 39. Continued.



(c)  $c_{l,v} = 0.6$ .

Figure 39. Concluded.

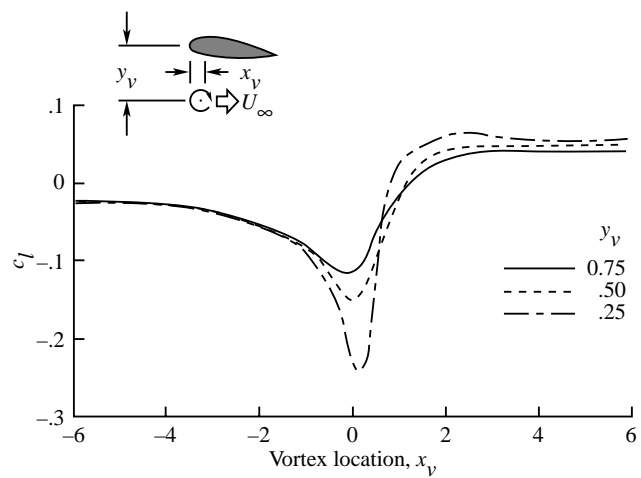
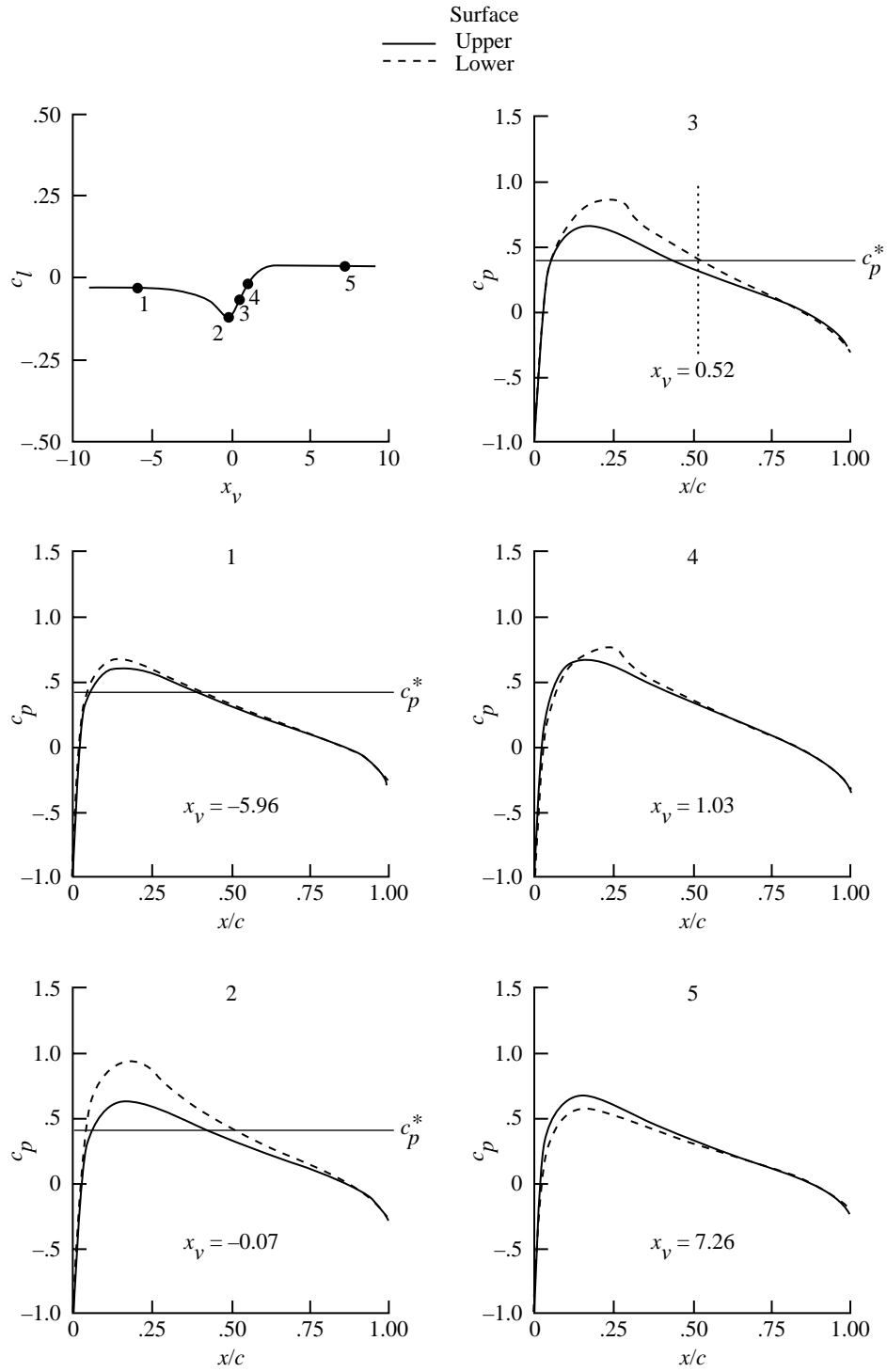
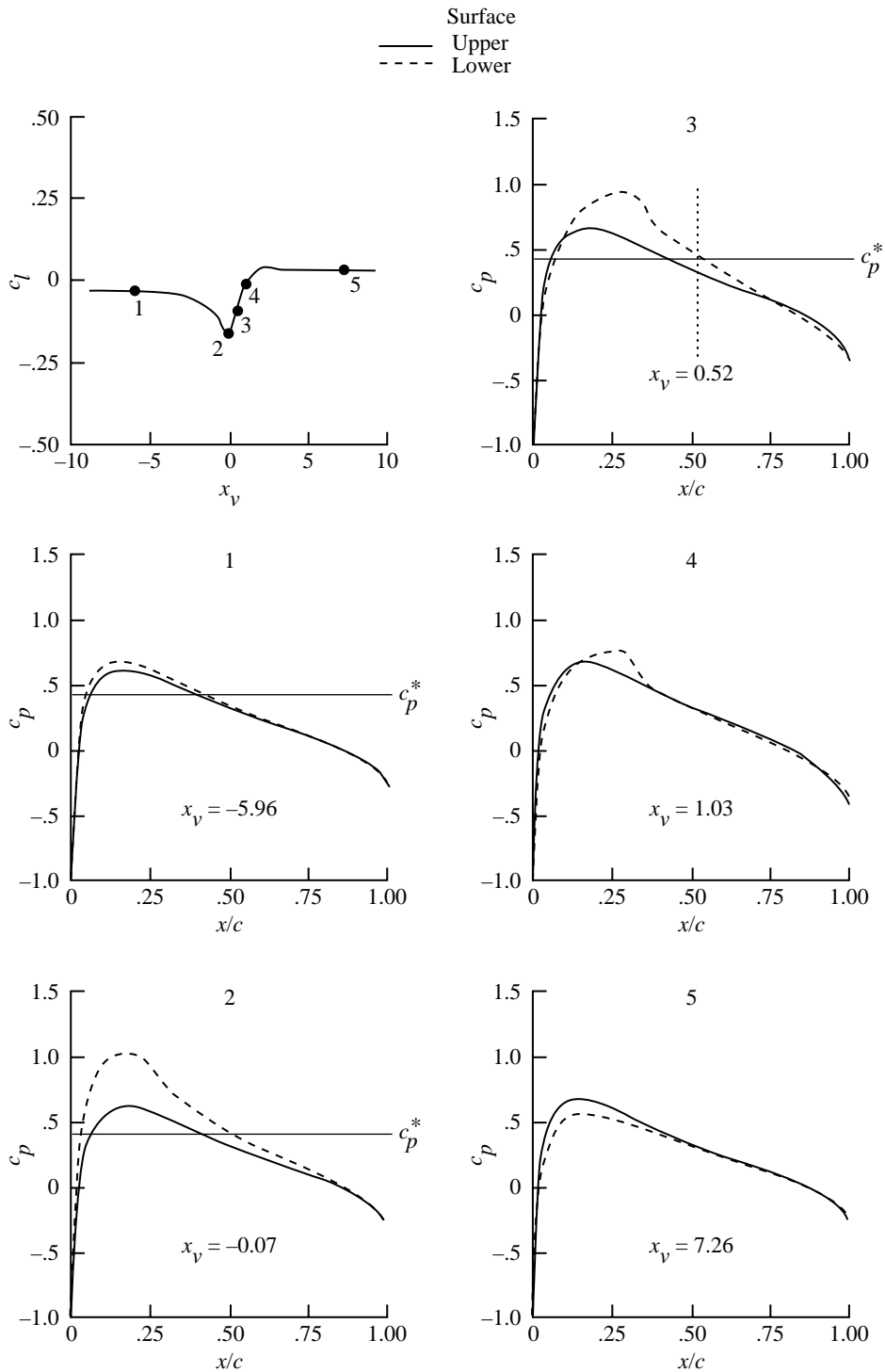


Figure 40. Effect of vertical miss distance on variation of airfoil lift coefficient.  $a = 0.05$ ;  $\alpha = 0^\circ$ ;  $M_\infty = 0.714$ ;  $c_{l,v} = 0.400$ ; NACA 0012 airfoil; fixed path.



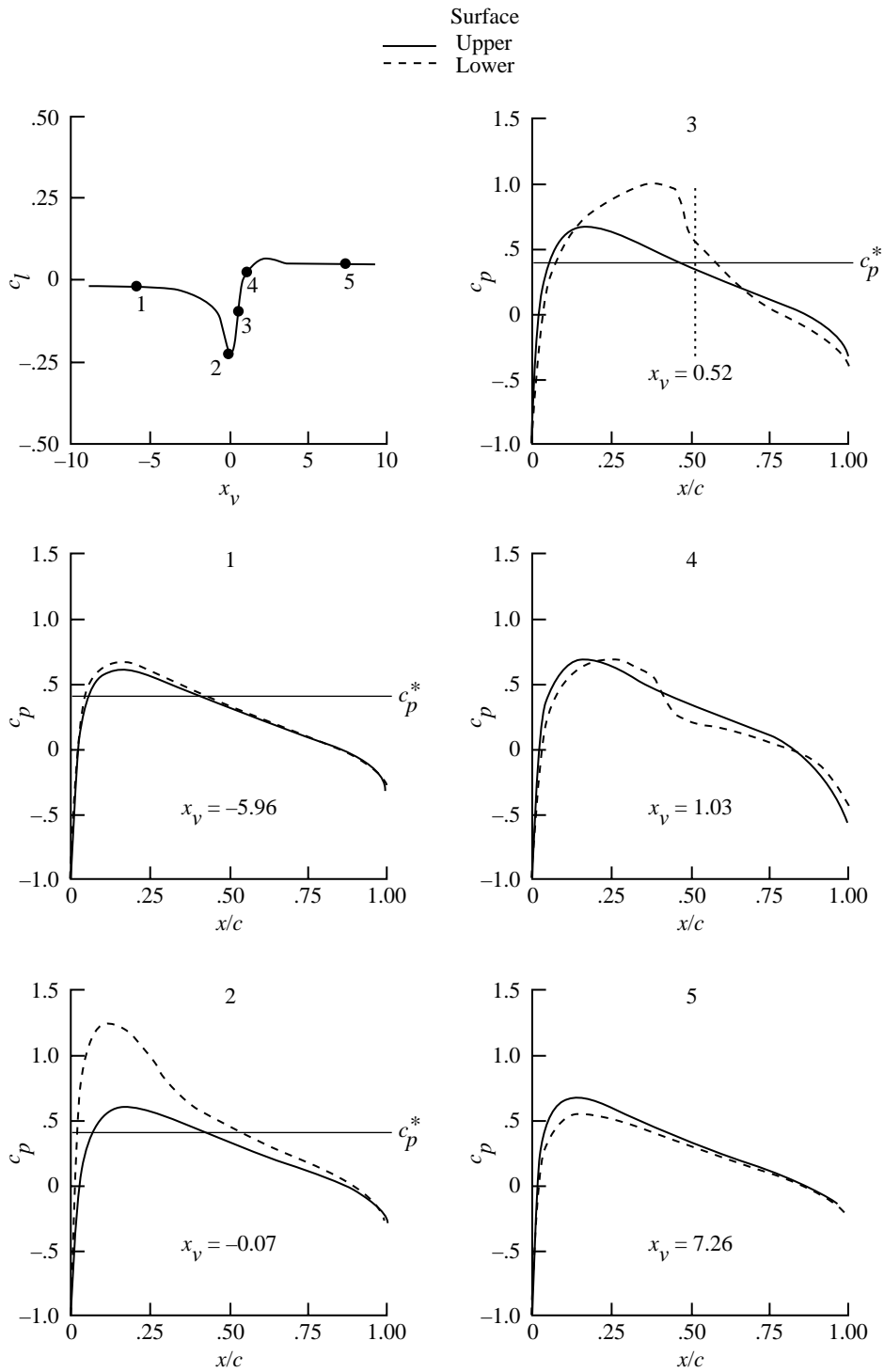
(a)  $y_v = -0.75$ .

Figure 41. Airfoil pressure distribution at selected vortex locations for several values of  $y_v$ .



(b)  $y_v = -0.50$ .

Figure 41. Continued.



(c)  $y_v = -0.25$ .

Figure 41. Concluded.

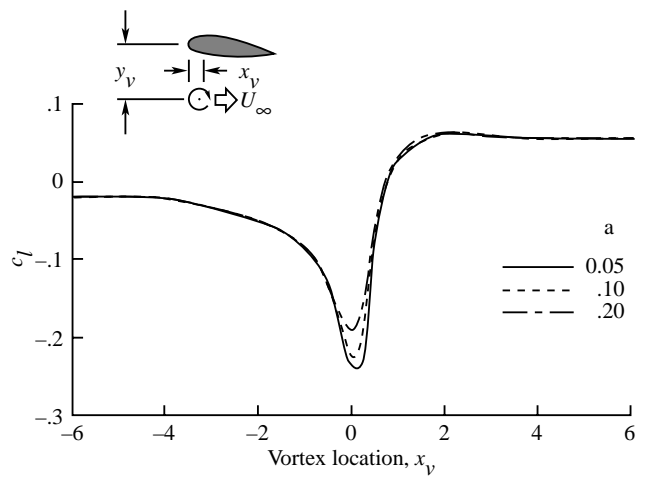
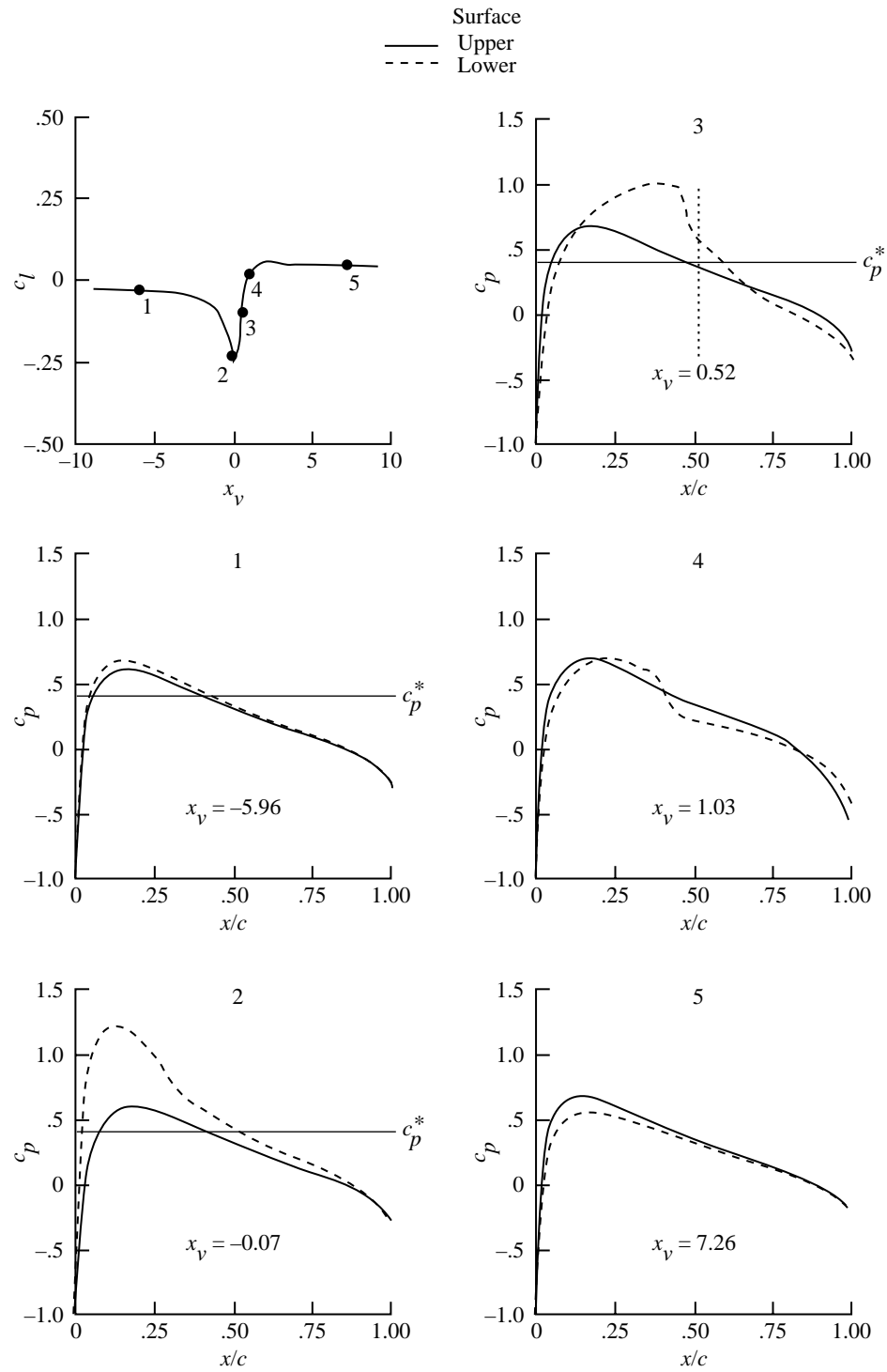
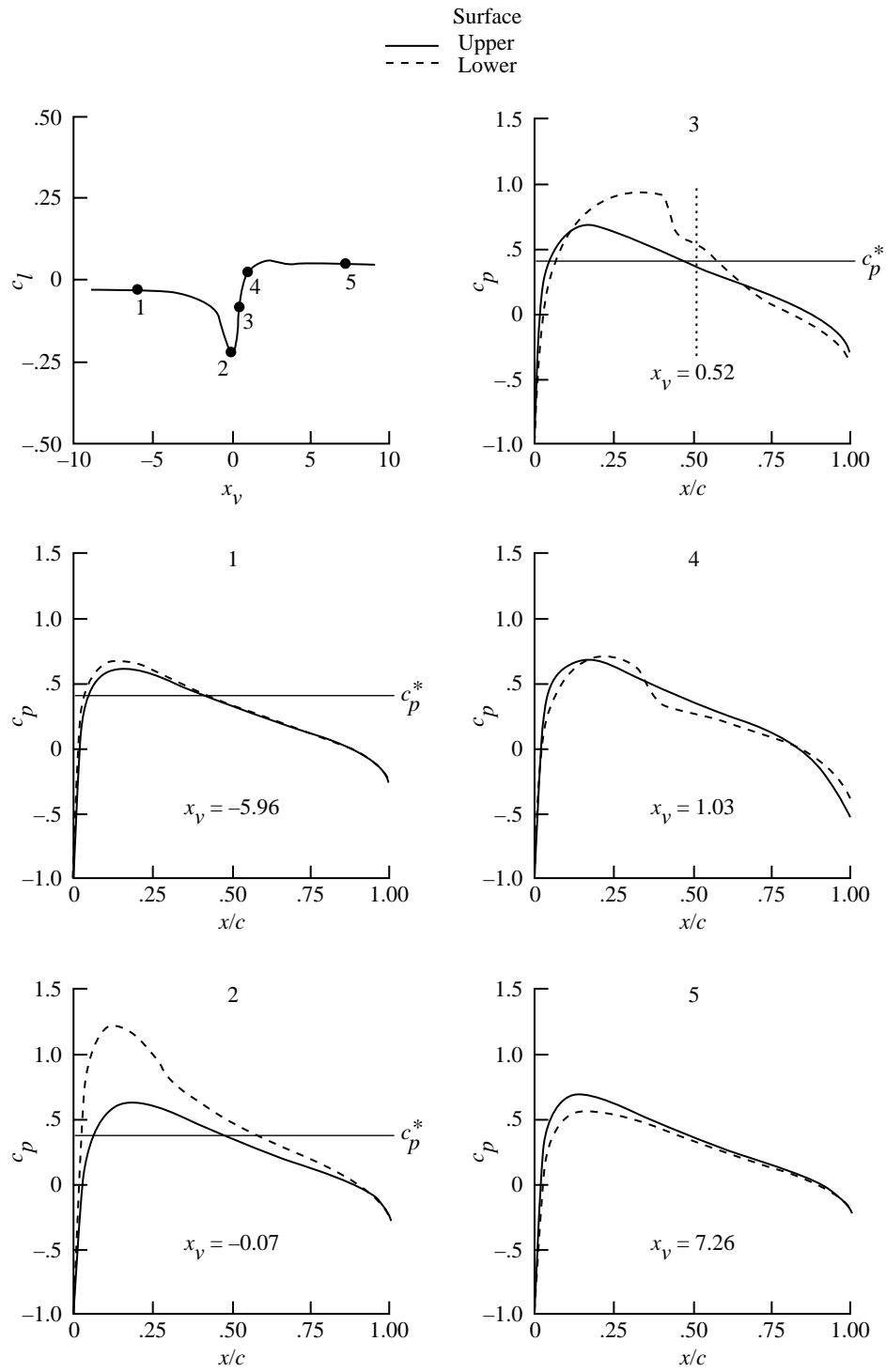


Figure 42. Effect of core size on variation of airfoil lift.  $\alpha = 0^\circ$ ;  $M_\infty = 0.714$ ;  $y_v = -0.251$ ;  $c_{l,v} = 0.400$ ; NACA 0012 airfoil; fixed path.



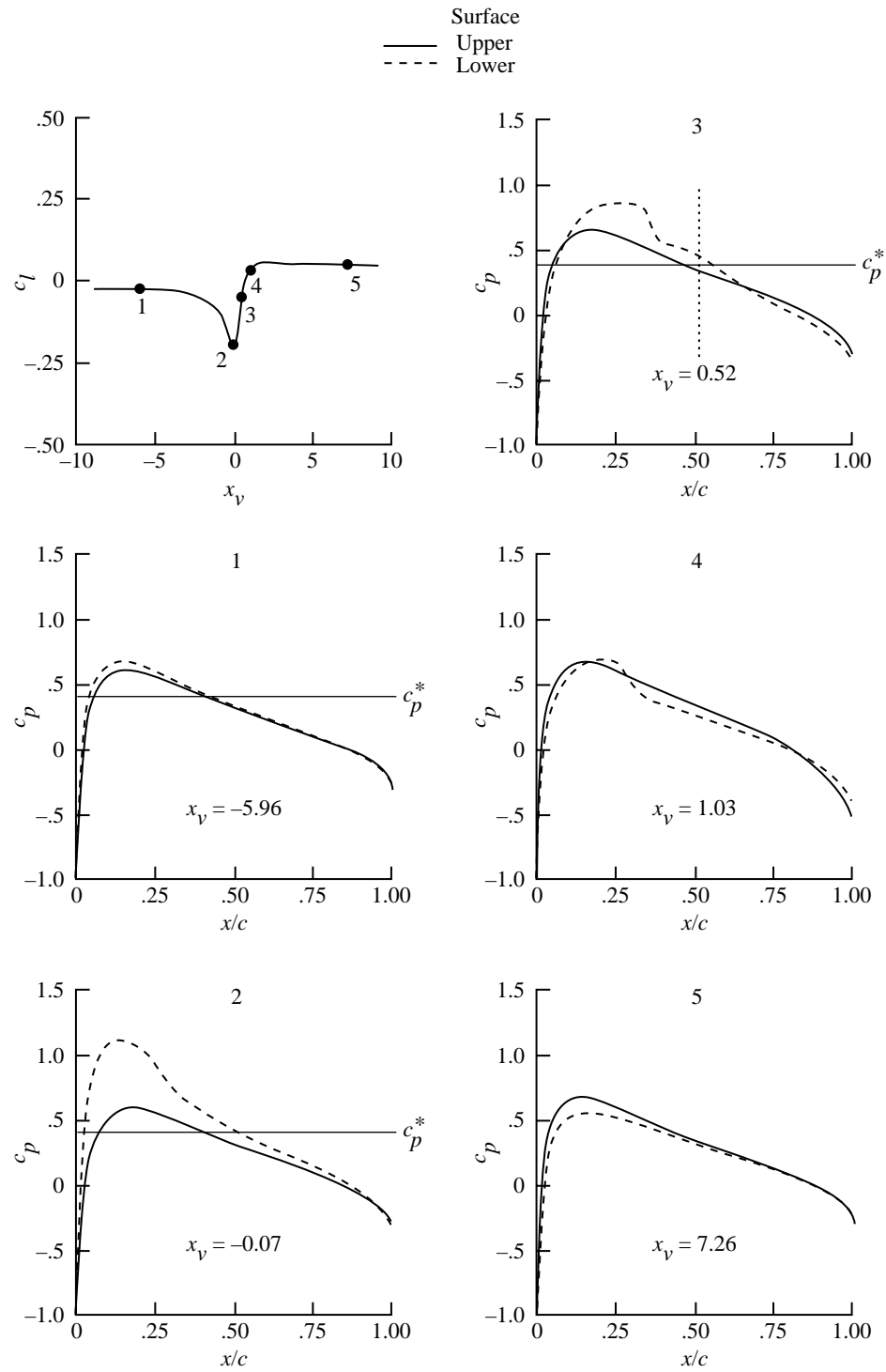
(a)  $a = 0.05$ .

Figure 43. Airfoil pressure distribution at selected vortex locations for several vortex core radii.



(b)  $a = 0.10$ .

Figure 43. Continued.



(c)  $a = 0.15$ .

Figure 43. Concluded.

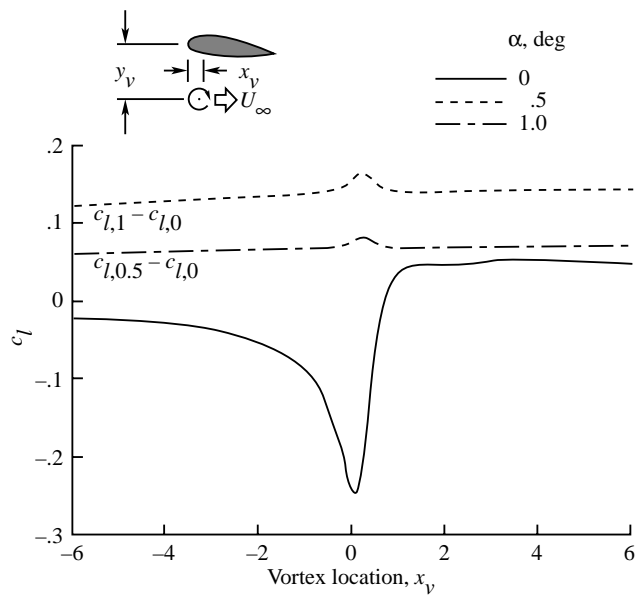
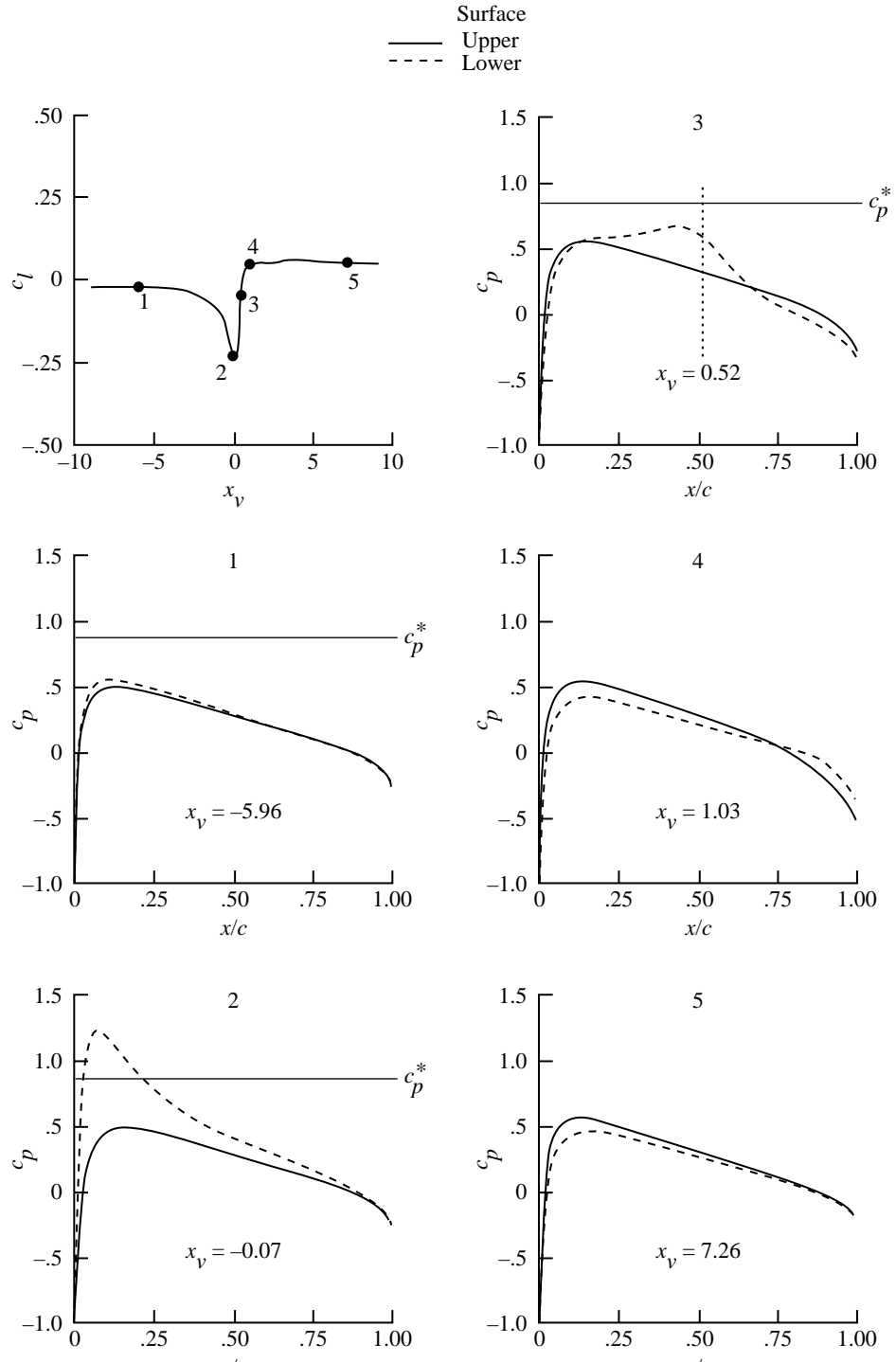
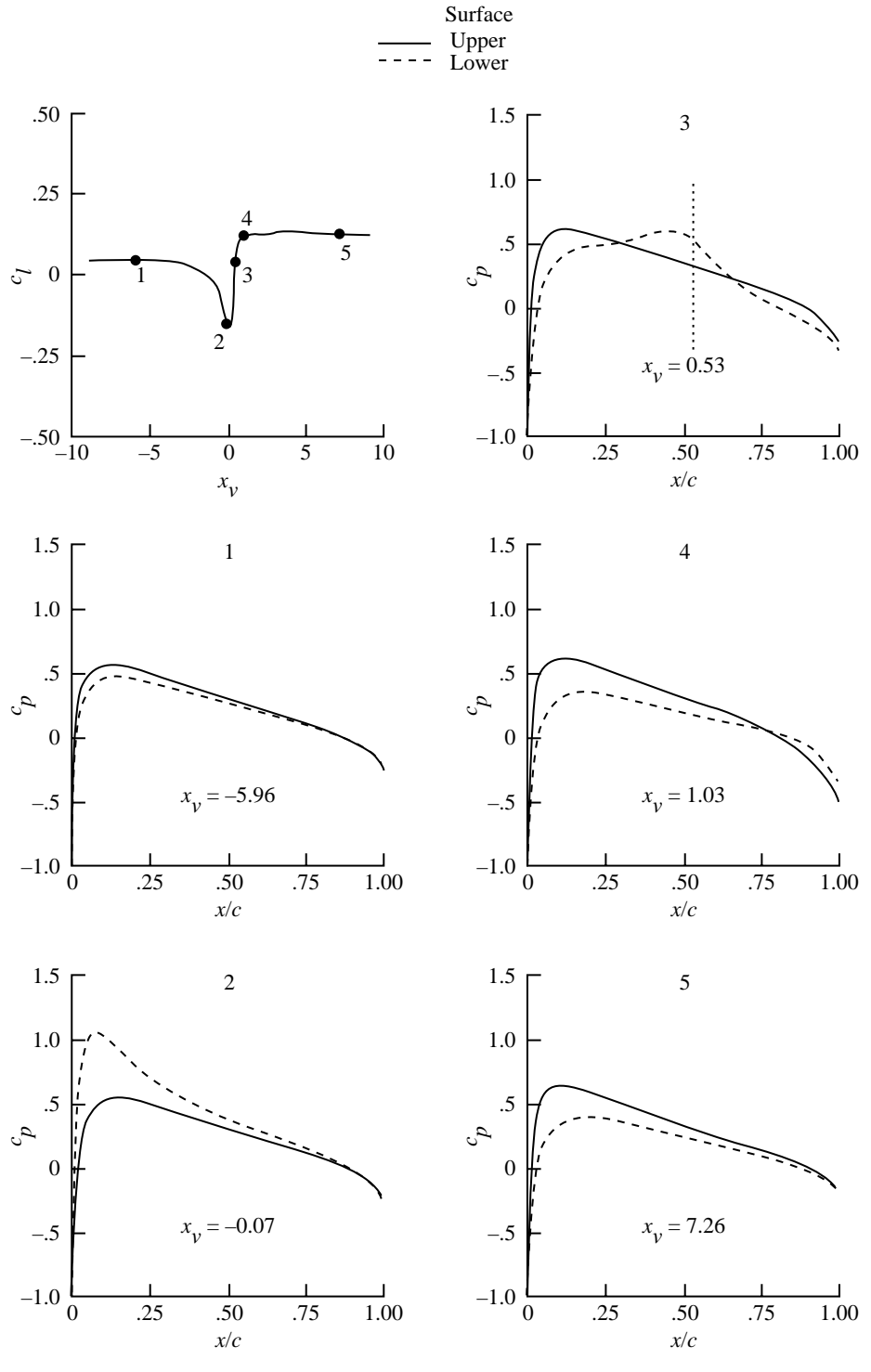


Figure 44. Effect of angle of attack on airfoil lift variation for subcritical flow.  $a = 0.05$ ;  $M_\infty = 0.60$ ;  $y_v = -0.251$ ;  $c_{l,v} = 0.400$ ; NACA 0012 airfoil; fixed path.



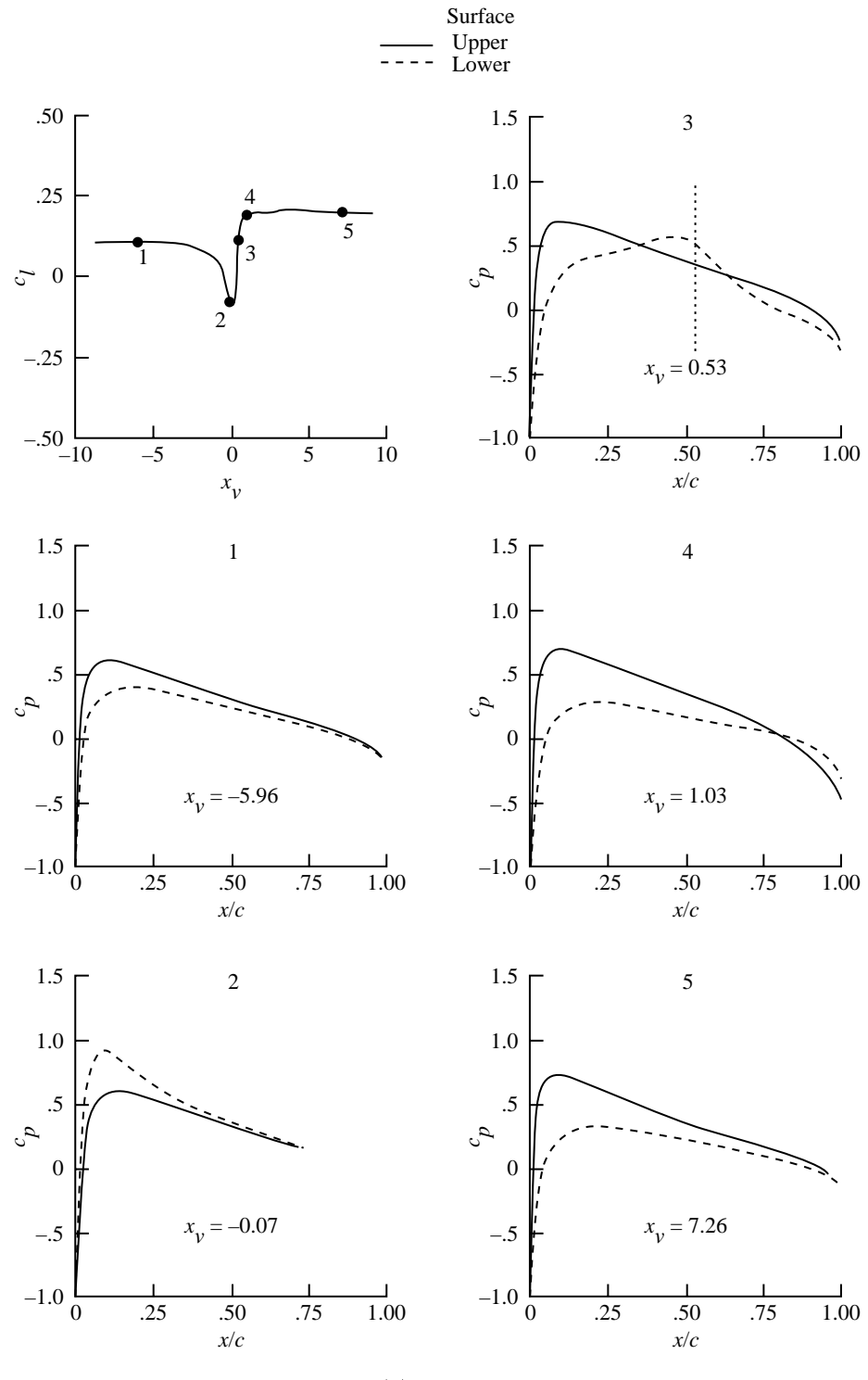
(a)  $\alpha = 0^\circ$ .

Figure 45. Airfoil pressure distribution at selected vortex locations.



(b)  $\alpha = 0.5^\circ$ .

Figure 45. Continued.



(c)  $\alpha = 1^\circ$ .

Figure 45. Concluded.

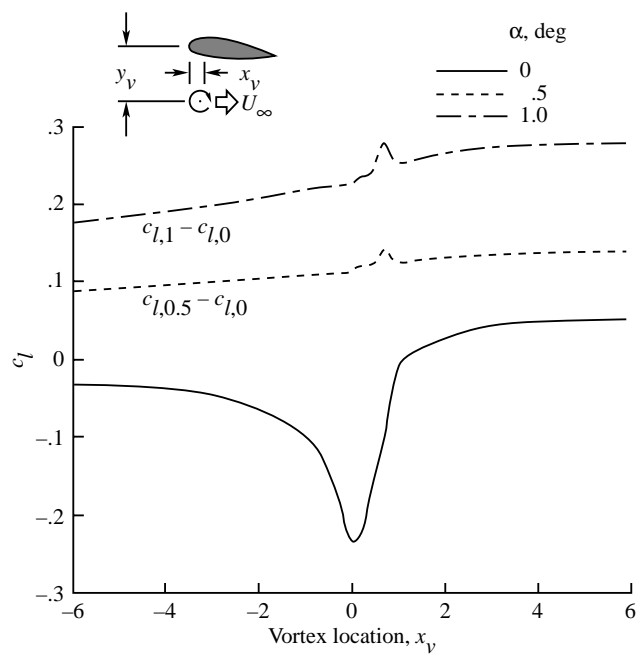
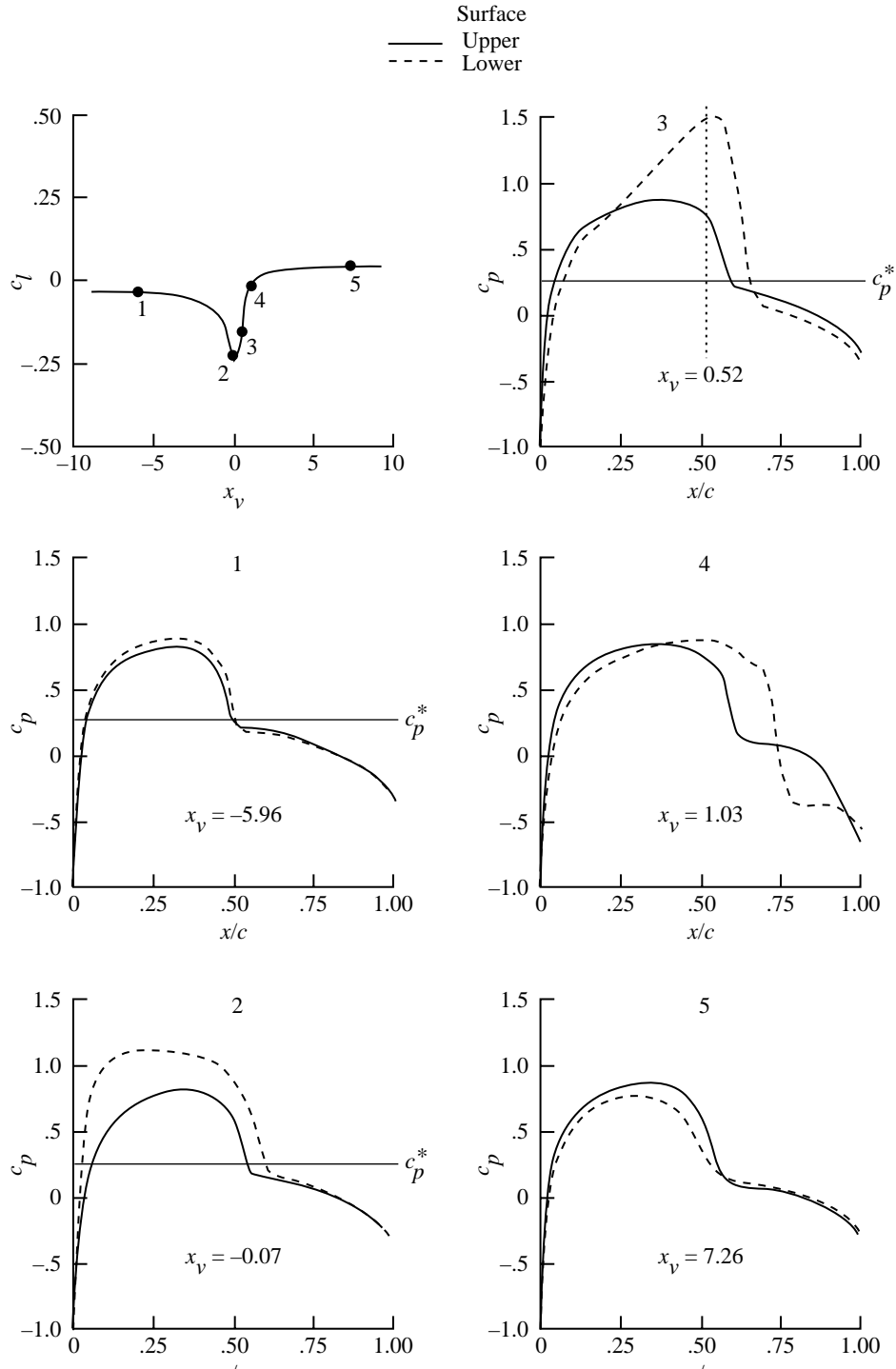
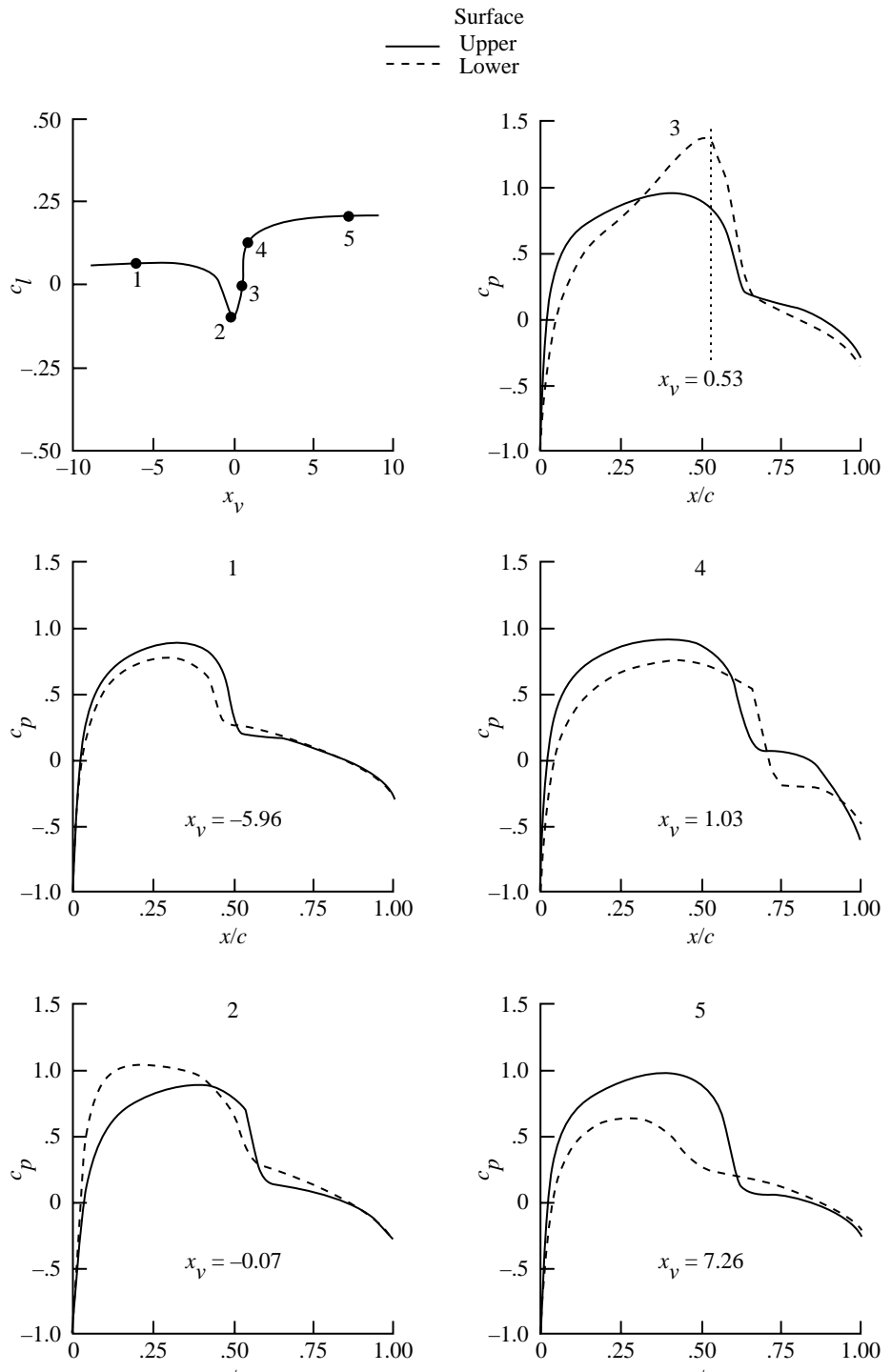


Figure 46. Effect of angle of attack on airfoil lift variation for supercritical flow.  $a = 0.05$ ;  $M_\infty = 0.80$ ;  $y_v = -0.251$ ;  $c_{l,v} = 0.400$ ; NACA 0012 airfoil; fixed path.



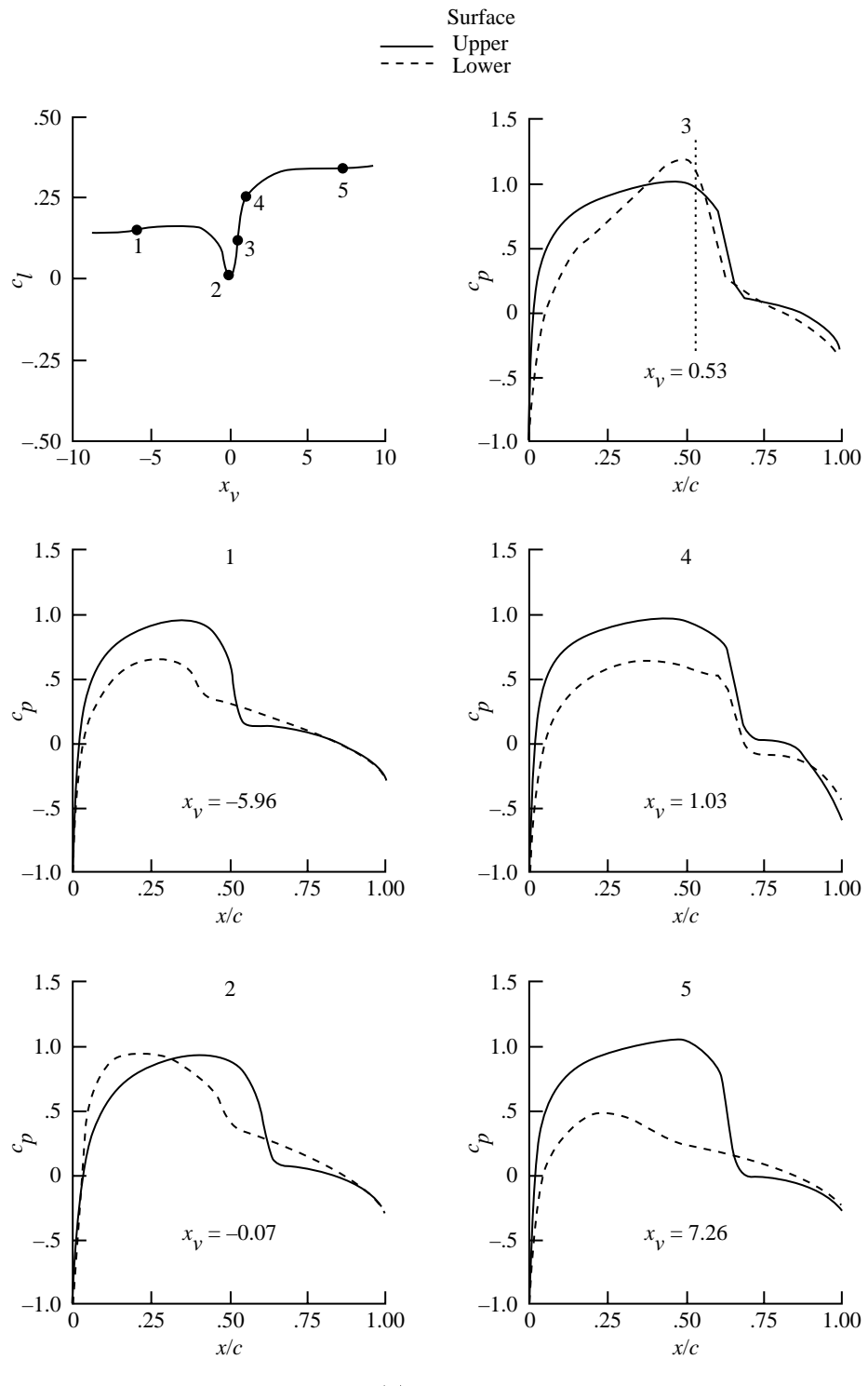
(a)  $\alpha = 0^\circ$ .

Figure 47. Airfoil pressure distribution at selected vortex locations.



(b)  $\alpha = 0.5^\circ$ .

Figure 47. Continued.



(c)  $\alpha = 1^\circ$ .

Figure 47. Concluded.

## 5. Concluding Remarks

A study of the full-potential modeling of a blade-vortex interaction has been made. A primary goal of this study was to investigate the effectiveness of the various methods of modeling the vortex. The problem was studied within the context of a two-dimensional model problem, which represents one of the limiting types of blade-vortex interactions. The model problem restricts the interaction to that of an infinite wing with an infinite line vortex moving parallel to its leading edge. This problem provides a convenient testing ground for the various methods of modeling the vortex while retaining the essential physics of the full three-dimensional (3-D) interaction. The flow field is assumed to be inviscid, irrotational, unsteady and, in general, transonic.

A full-potential algorithm specifically tailored to solve the blade-vortex interaction (BVI) was developed to solve this problem. The algorithm is based on a model first presented by Steger and Caradonna (NASA TM-81211, AVRADCOM TR 80-A-14). The algorithm makes use of the unsteady mass conservation and Bernoulli equations to form a full-potential model of the flow field. The system of equations is reduced to one equation by using a Taylor-series expansion of the temporal derivative of the density term in the conservation equation. The spatial derivatives are recast in delta form, with the density written at the previous time step. The stability of the algorithm in transonic flow is assured through the use of upwind biasing of the density in the flux terms. The flux metrics are computed by the consistent metric method, which has been found to be superior to the so-called free-stream subtraction method that has difficulties with grid singularities. The equation is approximately factored into convenient geometric parts in order to reduce the matrix to a compact form. A tridiagonal matrix inversion is used to solve for the updated potential solution. The model has the capability to predict the steady and unsteady flow about an airfoil under subcritical and transonic flow conditions. Comparisons of the results predicted are made with those presented by other researchers and with experimental data. The comparisons indicate that the algorithm is able to predict basic unsteady transonic flow about an airfoil.

The basic algorithm has been modified to include the effect of a vortex passing near the airfoil. Four different methods of modeling of the vortex were used:

1. The angle-of-attack method
2. The lifting-surface method

### 3. The branch-cut method

### 4. The split-potential method

The angle-of-attack method uses the velocity field of a point vortex to compute a vortex-induced velocity at the airfoil quarter-chord. This velocity is then used to compute an effective angle of attack of the airfoil. This method is identical to techniques that are currently in use in comprehensive helicopter rotor analyses. The lifting-surface method is an extension of the angle-of-attack method in which the vortex-induced velocity is a function of chordwise distance on the airfoil surface. The branch-cut method is a flow-field vortex representation that makes use of a surface of potential discontinuity, the edge of which constitutes the vortex location. The effect of the vortex is implemented by imposing special differencing methods along the cut. In the split-potential method, the velocity field is split between a known field (induced by the vortex) and an unknown perturbation field due the airfoil.

A side-by-side comparison of the four models was conducted. These comparisons included:

1. Comparing generated velocity fields
2. A subcritical interaction
3. A critical interaction

The subcritical and critical interactions are also compared with experimentally generated results.

The following conclusions have been reached as a result of these comparisons:

1. All the methods give qualitatively similar results for integrated loads but differ considerably in the details.
2. An artificial core is necessary in order to remove the singularity in the vortex velocity equation.
3. Only the explicit models predict the presence of shock waves for the critical interaction.
4. The branch-cut method shows a strong sensitivity to the mesh configuration which leads to spurious waves in the solution, especially for transonic flow conditions.
5. The angle-of-attack method is sensitive to miss distance and predicts a spike in the loading curve which is not present in the other methods. This spike is caused by the abrupt change in angle of attack as the vortex passes the airfoil quarter-chord.
6. The lifting-surface method compares well with the split-potential method in computing integrated loads, especially for subcritical flow.

However, the details of the pressure time histories during the closest part of the interaction differ significantly. Nevertheless this method has proven to be useful in 3-D problems to specify far-field vortex effects.

7. The split-potential method is the most versatile and robust method.
8. The temporal gradient terms in the split-potential method must be retained in order to predict strong interactions. This retention may cause a slight increase in computing time for 3-D problems, but this increase can be offset by using the lifting-surface method for vortices far from the blade.

The split-potential model was used to make a survey of some of the more critical parameters which affect the BVI. The survey studies general flow parameters such as free-stream Mach number and airfoil angle of attack and vortex parameters such as strength, core size, and miss distance. The results were computed at subcritical and supercritical free-stream Mach numbers. For the vortex parameters, the free-stream Mach number was chosen to be just subcritical to study the effect of the vortex on the formation of critical flow on the airfoil. Based on the survey results, the following conclusions were reached:

1. Free-stream Mach number has little direct effect on the basic BVI except to modify the signal propagation speed which tends to broaden the loading signature. This effect was also noted experimentally in NASA TM-86005, USAAVSCOM TM-84-A-9. However, the vortex can induce shocks on an airfoil which is in near-critical flow.
2. The BVI loading response varies linearly with the vortex strength. The vortex induces shocks on the airfoil surface and the shock strength varies linearly with the vortex strength. For strong vortices, the shock may interact with the vortex directly to cause high peak pressures on the airfoil.
3. The BVI loading response varies linearly with the inverse of the vortex miss distance. Vortex-induced shock strength also varies linearly with the inverse of the miss distance.
4. The BVI loading response varies directly with the inverse of vortex core size  $a$ . Furthermore, the core size shifts the point of minimum lift in direct proportion to  $a$  and the shock strength varies directly with  $a$ .
5. The effect of airfoil angle of attack  $\alpha$  is to shift the magnitude of the loading curve by a constant value which varies linearly with  $\alpha$ .

A primary goal of this report has been to study the effect of the vortex model on the computation of the BVI problem. The selection of an appropriate technique of modeling the vortex would be based on this study; this has been accomplished. The split-potential model has proven to be the most versatile and robust method of the currently available techniques. The lifting-surface method has been shown to be a useful approximation to the split-potential method especially for far-field vortex specifications. The next logical step in this study is to extend these results to the 3-D rotor problem. In the process of accomplishing this, the method should be coupled with an existing comprehensive helicopter method, similar to that used by Strawn and Caradonna (AIAA-86-0079). The 3-D model should include a completed vortex wake model that uses a combined split-potential and lifting-surface method. Another interesting application of the split-potential technique would be to use it to model linear portions of the flow field (e.g., the rotational flow field).

The modeling of the BVI continues to be a key problem in helicopter aerodynamics because it is a major determinant of vibratory loading and noise. This report has analyzed the interaction in two dimensions and used this model problem to find the best means of determining BVI loading within the context of a finite-difference computation. The extension to three dimensions should build directly on this work. Beyond this point, the greatest problem will be to find an efficient and accurate way to predict the three-dimensional structure of the rotor wake.

NASA Langley Research Center  
Hampton, VA 23681-0001  
April 22, 1997

## Appendix A

### Computational Grid

The computational grid used in the present method is based on the streamlines and potential lines around a Joukowski airfoil in incompressible flow and at  $\alpha = 0^\circ$ . The intersection of this set of lines forms an orthogonal H-type mesh. This type of mesh is useful for three reasons:

1. It closely conforms to the shape of an airfoil, thereby accuracy is increased
2. It is orthogonal which simplifies coding
3. The gridlines align with the free stream away from the airfoil

The solution of the Joukowski airfoil is a classical problem in aerodynamics. The solution is based on the conformal mapping technique which arises from complex variable theory. The details of this well-known derivation are provided for students of the art.

The stream function  $\Psi(\xi, \eta)$  and the potential function  $\Phi(\xi, \eta)$  are related through the differential equations

$$\left. \begin{aligned} \frac{\partial \Phi}{\partial x} &= \frac{\partial \Psi}{\partial y} = u \\ \frac{\partial \Phi}{\partial y} &= -\frac{\partial \Psi}{\partial x} = v \end{aligned} \right\} \quad (\text{A1})$$

Both functions are solutions to Laplace's equation

$$\nabla^2 \Phi = \nabla^2 \Psi = 0 \quad (\text{A2})$$

Therefore, the stream function and the potential function may be combined into an analytic function of a complex variable  $z^*$ :

$$w(z^*) = \Phi + i\Psi \quad (\text{A3})$$

The function  $w(z^*)$  is often referred to as the complex potential. When given a known function  $w(z^*)$ , the potential field may be deduced by setting  $\Phi$  equal to the real part of  $w(z^*)$ .

The solution of Laplace's equation for problems with complicated boundaries is achieved with the aid of conformal mapping. The problem is mapped from the  $z^*$  plane to another plane in which the boundaries are simplified. The primary restriction on the transformation is that the mapping function be analytic. Joukowski presented a function which transforms the flow about a circle to that about an airfoil shape. (See ref. 29.) From this solution, obtaining

an equation for the streamlines and potential lines about this airfoil shape is possible.

Consider the flow field about a circle of radius  $b$ , then the complex potential is

$$w = U_\infty \left( z^* + \frac{b^2}{z^*} \right) \quad (\text{A4})$$

where

$$z^* = \xi + i\eta \quad (\text{A5})$$

From equation (A3),

$$\Phi + i\Psi = U_\infty \left( \xi + i\eta + \frac{b^2}{\xi + i\eta} \right) \quad (\text{A6})$$

Equating real and imaginary parts gives

$$\left. \begin{aligned} \Phi &= U_\infty \xi \left( 1 + \frac{b^2}{\xi^2 + \eta^2} \right) \\ \Psi &= U_\infty \eta \left( 1 - \frac{b^2}{\xi^2 + \eta^2} \right) \end{aligned} \right\} \quad (\text{A7})$$

The velocities  $\Phi_\xi$  and  $\Phi_\eta$  are

$$\left. \begin{aligned} \Phi_\xi &= U_\infty \frac{(\xi^2 + \eta^2)^2 + b^2(\eta^2 - \xi^2)}{(\xi^2 + \eta^2)^2} \\ \Phi_\eta &= 2 \frac{b^2 U_\infty \xi \eta}{(\xi^2 + \eta^2)^2} \end{aligned} \right\} \quad (\text{A8})$$

The derivatives  $\Psi_\eta$  and  $\Psi_\xi$  are

$$\left. \begin{aligned} \Psi_\eta &= U_\infty \frac{(\xi^2 + \eta^2)^2 - b^2(\eta^2 - \xi^2)}{(\xi^2 + \eta^2)^2} \\ \Psi_\xi &= 2 \frac{b^2 U_\infty \xi \eta}{(\xi^2 + \eta^2)^2} \end{aligned} \right\} \quad (\text{A9})$$

The slope of the streamlines is

$$\frac{d\eta}{d\xi} = \frac{-\Phi_\eta}{\Phi_\xi} = \frac{-2b^2\eta\xi}{(\xi^2 + \eta^2)^2 - b^2(\xi^2 - \eta^2)} \quad (\text{A10})$$

Equation (A10) may be integrated to produce

$$\eta_{i+1} = \zeta^* \Delta \xi_i + \eta_i \quad (\text{A11})$$

where  $\zeta^*$  is equal to  $\frac{d\eta}{d\xi}$ . Equation (A11) is for a line of constant stream function.

The grid is generated with the following steps:

1. Produce a satisfactory stretched Cartesian grid by any method
2. Use the  $(\xi, \eta)$  coordinates along the front of the mesh as a start to integrate equation (A10) until you reach the aft face of the mesh (this solves for the streamlines around the circle)
3. Transform the circle solution by using the Joukowski transformation to produce the airfoil solution
4. Select an appropriate distribution of point along the airfoil streamline
5. Interpolate to find the potential at each of these points
6. Find the location on each of the off-airfoil streamlines which have matching potential values
7. Form the new mesh with the resulting set of points

## Appendix B

### Derivations of Boundary Conditions

There are two special equations which are used in implementing the boundary conditions in the full-potential algorithm. Both these equations make use of special applications of the Bernoulli equation.

The first equation is used along the aft face of the computational grid to ensure that  $\rho = 1$ . A special equation is required because of the presence of branch cuts which specify a jump in potential and hence preclude the use of a Dirichlet condition. The equation is used to determine the velocity which is used in the flux computation. For  $\rho = 1$ , the Bernoulli equation yields

$$2\Phi_\tau + \mathbf{U}\Phi_\xi + \mathbf{V}\Phi_\eta = M_\infty^2 \quad (\text{B1})$$

The aft face of the computational grid is far from the airfoil (80 chords). It is therefore valid to assume

$$\left. \begin{aligned} \mathbf{V} &= 0 \\ \mathbf{A}_1 &= \xi_x^2 \\ \Phi_\xi &= \phi_\xi + M_\infty x \end{aligned} \right\} \quad (\text{B2})$$

With these assumptions obtain

$$2\phi_\tau + M_\infty \xi_x \phi_\xi = M_\infty^2 \quad (\text{B3})$$

The equation for  $\phi_\xi$  is

$$\phi_\xi = \frac{1}{\xi_x} [M_\infty - \frac{\phi_\tau}{M_\infty}] \quad (\text{B4})$$

Equation (B4) is used in the flux computation along the aft face of the computational mesh in place of the usual backward difference of  $\Phi$ .

The second equation is used to compute the convection of  $\Gamma$  downstream of the airfoil trailing edge. Since the wake cut is a shear layer, density and  $\mathbf{V}$  are constant across it. The jump in potential is

$$\Gamma = \|\Phi\| = \Phi_u - \Phi_l \quad (\text{B5})$$

Using the Bernoulli equation gives

$$\begin{aligned} 2(\Phi_l)_\tau + \mathbf{A}_1 [\partial_\xi(\Phi_l)]^2 &= 2\partial_\tau(\Phi_l + \Gamma) \\ &\quad + \mathbf{A}_1 [\partial_\xi(\Phi_l + \Gamma)]^2 \end{aligned} \quad (\text{B6})$$

Eliminating terms gives

$$2\Gamma_\tau + 2\mathbf{A}_1 \Phi_\xi \Gamma_\xi + \mathbf{A}_1 \Gamma_\xi^2 = 0 \quad (\text{B7})$$

The higher order term is dropped for convenience to give

$$\Gamma_\tau + \langle \mathbf{U} \rangle \Gamma_\xi = 0 \quad (\text{B8})$$

The term  $\langle \mathbf{U} \rangle$  is simply the average of the velocities above and below the cut. Equation (B8) is used to determine the convected value of  $\Gamma$  along the wake cut.

## Appendix C

### Time Linearization Operator

The conventional form of an operator which is derived from the Bernoulli equation and acts on the difference  $\Phi^{N+1} - \Phi^N$  is given by equation (2.22), which is

$$\left( \frac{\partial \rho}{\partial \Phi} \right)^N \equiv -\rho^{2-\gamma} \left( \frac{\partial}{\partial \tau} + \frac{\mathbf{U} \partial}{\partial \xi} + \frac{\mathbf{V} \partial}{\partial \eta} \right)^N$$

The operator arises from the linearization of the density which is necessary to maintain strong conservative form. The linearization takes the form

$$\rho = \rho_o + \frac{\partial \rho}{\partial \Phi} (\Phi - \Phi_o) \quad (C1)$$

The subscript  $o$  represents a neighboring known state or solution. If  $(\Phi - \Phi_o)$  is small, for example  $(\Phi^{N+1} - \Phi^N)$  or  $(\Phi_i - \Phi_{i-1})$ , where  $t = n\Delta t$  and  $x = i\Delta x$ , the error due to expanding  $\rho$  is second-order accurate and is no greater than that usually

made in time differencing. Equation (C1) is obtained by using the Bernoulli equation

$$\begin{aligned} \rho &= \rho_o + \left[ 1 + \frac{\gamma-1}{2} (M_\infty^2 - 2\Phi_\tau - \mathbf{U}\Phi_\xi - \mathbf{V}\Phi_\eta) \right]^{\frac{1}{\gamma-1}-1} \\ &\quad + \left( \frac{1}{\gamma-1} \right) \frac{\gamma-1}{2} \left[ -2(\Phi_\tau^{N+1} - \Phi_\tau^N) \right. \\ &\quad \left. - 2\mathbf{A}_1 \Phi_\xi^N (\Phi_\xi^{N+1} - \Phi_\xi^N) - 2\mathbf{A}_3 \Phi_\eta^N (\Phi_\eta^{N+1} - \Phi_\eta^N) \right] \end{aligned} \quad (C2)$$

Combining terms gives

$$\rho = \rho_o - \rho^{2-\gamma} \left( \frac{\partial}{\partial \tau} + \frac{\mathbf{U} \partial}{\partial \xi} + \frac{\mathbf{V} \partial}{\partial \eta} \right)^N (\Phi^{N+1} - \Phi^N) \quad (C3)$$

so that the operator becomes

$$\left( \frac{\partial \rho}{\partial \Phi} \right)^N \equiv -\rho^{2-\gamma} \left( \frac{\partial}{\partial \tau} + \frac{\mathbf{U} \partial}{\partial \xi} + \frac{\mathbf{V} \partial}{\partial \eta} \right)^N$$

## References

1. Johnson, Wayne: *A Lifting Surface Solution for Vortex Induced Airloads and Its Application to Rotary Wing Airloads Calculations*. NASA CR-192328, 1970.
2. Steger, J. L.; and Caradonna, F. X.: *A Conservative Implicit Finite Difference Algorithm for the Unsteady Transonic Full Potential Equation*. NASA TM-81211, AVRADCOM TR 80-A-14, 1980.
3. Glauert, H.: *A General Theory of the Autogyro*. R. & M. No. 1111, British ARC, 1926.
4. Piziali, Raymond A.; and DuWaldt, Frank A.: A Method for Computing Rotary Wing Airload Distributions in Forward Flight. TCREC Tech. Rep. 62-44, U.S. Army, Nov. 1962. (Available from DTIC as AD 295 089.)
5. Isay, W. H.: Zur Traglinientheorie des Hubschrauberrotors. (Lifting-Line Theory of a Helicopter Rotor). *Z. Angew. Math. Mech.*, vol. 49, no. 9, 1969, pp. 533-544. (Available as NASA TT F-13245.)
6. Kocurek, J. D.: A Lifting Surface Performance Analysis With Circulation Coupled Wake for Advanced Configuration Hovering Rotors. Ph.D. Thesis, Texas A & M Univ., 1978.
7. Johnson, Wayne: *A Comprehensive Analytical Model of Rotorcraft Aerodynamics and Dynamics. Part 1: Analysis Development*. NASA TM-81182, AVRADCOM TR 80-A-5, 1980.
8. Caradonna, F. X.; Tung, C.; and Desopper, A.: *Finite Difference Modeling of Rotor Flows Including Wake Effects*. ONERA TP no. 1982-114, 1982.
9. Straw, R. C.; and Caradonna, F. X.: Numerical Modeling of Rotor Flows With a Conservative Form of the Full-Potential Equations. AIAA-86-0079, Jan. 1986.
10. Bridgeman, J. O.; Steger, J. L.; and Caradonna, F. X.: A Conservative Finite Difference Algorithm for the Unsteady Transonic Potential Equation in Generalized Coordinates. AIAA-82-1388, Aug. 1982.
11. George, Albert R.; and Chang, S. B.: Noise Due to Transonic Blade-Vortex Interactions. *Proceedings of the 39th Annual Forum, American Helicopter Soc.*, May 1983.
12. George, A. R.; and Chang, S. B.: Flow Field and Acoustics of Two-Dimensional Transonic Blade-Vortex Interactions. AIAA-84-2309, Oct. 1984.
13. McCroskey, W. J.; and Goorjian, P. M.: Interactions of Airfoils With Gusts and Concentrated Vortices in Unsteady Transonic Flow. AIAA-83-1691, July 1983.
14. Steinhoff, J.; Ramachandran, K.; and Suryanarayanan, K.: The Treatment of Convected Vortices in Compressible Potential Flow. *Aerodynamics of Vortical Type Flows in Three Dimensions*, AGARD CP-342, July 1983, pp. 22-1-22-12. (Available from DTIC as AD A135 157.)
15. Srinivasan, G. R.; McCroskey, W. J.; and Kutler, P.: Numerical Simulation of the Interaction of a Vortex With Stationary Airfoil in Transonic Flow. AIAA-84-0254, Jan. 1984.
16. Srinivasan, G. R.; McCroskey, W. J.; and Baeder, J. D.: Aerodynamics of Two-Dimensional Blade-Vortex Interaction. AIAA-85-1560, July 1985.
17. Sankar, L. N.; and Malone, J. B.: Unsteady Transonic Full Potential Solutions for Airfoils Encountering Vortices and Gusts. AIAA-85-1710, July 1985.
18. Viviand, H.: Conservative Forms of Gasdynamics Equations. *La Recherche Aerospatiale*, Jan.-Feb. 1974, pp. 65-66.
19. Holst, T. L.; and Ballhaus, W. F.: *Conservative Implicit Schemes for the Full Potential Equation Applied to Transonic Flows*. NASA TM-78469, 1978.
20. Flores, J.; Holst, T. L.; Kwak, D.; and Batiste, D. M.: A New Consistent Spatial Differencing Scheme for the Transonic Full-Potential Equation. AIAA-83-0373, Jan. 1983.
21. Scully, M. P.: *Computation of Helicopter Rotor Wake Geometry and Its Influence on Rotor Harmonic Airloads*. ASRL TR 178-1 (Contracts N00019-73-C-0378 and N00019-74-C-0321), MIT, Mar. 1975.
22. Caradonna, F. X.: The Transonic Flow on a Helicopter Rotor. Ph.D. Thesis, Stanford Univ., 1978.
23. Stremel, P. M.: Computational Methods for Non-Planar Vortex Wake Flow Fields. M.S. Thesis, MIT, Feb. 1982.
24. Jones, H.: The Interaction of an Airfoil With a Vortex in Transonic Flow. AVSCOM paper presented at *Workshop on Blade-Vortex Interactions* (Ames Research Center, Moffett Field, Calif.), Oct. 1984.
25. Holst, T. L.: An Implicit Algorithm for the Conservative Transonic Full Potential Equation Using an Arbitrary Mesh. AIAA-78-1113, July 1978.
26. Goorjian, P. M.; and Guruswamy, G. P.: *Unsteady Transonic Aerodynamic and Aeroelastic Calculations About Airfoils and Wings*. NASA TM-85986, 1984.
27. Srinivasan, G. R.; and McCroskey, W. J.: Numerical Simulations of Unsteady Airfoil-Vortex Interactions. *Vertica*, vol. 11, no. 1-2, 1987, pp. 3-23, 25-28.
28. Caradonna, F. X.; Laub, G. H.; and Tung, C.: *An Experimental Investigation of the Parallel Blade-Vortex Interaction*. NASA TM-86005, USAVSCOM TM-84-A-9, 1984.
29. Durand, William Frederick, ed.: *Aerodynamic Theory. Volume II—General Aerodynamic Theory, Perfect Fluids*. Dover Publ., Inc., 1963, pp. 91, 355. (Primary Source—Joukowski, N.: Über die Konturen der Tragflächen der Drachenflieger, *Z.F.M.*, vol. 1, 1910, p. 281, and *Z.F.M.*, vol. 3, 1912, p. 81.)